ABSTRACT

Title of Dissertation:	Two Experiments with Cold Atoms: I. Application of Bessel Beams for Atom Optics, and II. Spectroscopic Measurements of Rydberg Blockade Effect
	Ilya Arakelyan, Doctor of Philosophy, 2010
Dissertation directed by:	Prof. Wendell Hill, III Department of Physics

In this dissertation we report the results of two experimental projects with laser-cooled rubidium atoms: I. Application of Bessel beams for atom optics, and II. Spectroscopic measurements of Rydberg blockade effect.

The first part of the thesis is devoted to the development of new elements of atom optics based on blue-detuned high-order Bessel beams. Properties of a 4th-order Bessel beam as an atomic guide were investigated for various parameters of the hollow beam, such as the detuning from an atomic resonance, size and the order of the Bessel beam. We extended its application to create more complicated interferometer-type structures by demonstrating a *tunnel lock*, a novel device that can split an atomic cloud, transport it, delay, and switch its propagation direction between two guides. We reported a first-time demonstration of an atomic beam switch based on the combination of two crossed Bessel beams. We achieved the 30% efficiency of the switch limited by the geometrical overlap between the cloud and the intersection volume of the two tunnels, and investigate the heating processes induced by the switch. We also showed other applications of crossed Bessel beams,

such as a 3-D optical trap for atoms confined in the intersection volume of two hollow beams and a splitter of the atomic density.

The second part of this dissertation is devoted to the spectroscopic measurements of the Rydberg blockade effect, a conditional suppression of Rydberg excitations depending on the state of a control atom. We assembled a narrow-linewidth, tunable, frequency stabilized laser system at 480 nm to excite laser-cooled rubidium atoms to Rydberg states with a high principal quantum number $n \sim 50$ through a two-photon transition. We applied the laser system to observe the Autler-Townes splitting of the intermediate $5p_{3/2}$ state and used the broadening of the resonance features to investigate the enhancement of Rydberg-Rydberg interactions in the presence of an external electric field.

Two Experiments with Cold Atoms: I. Application of Bessel Beams for Atom Optics, and II. Spectroscopic Measurements of Rydberg Blockade Effect

by

Ilya Arakelyan

Dissertation submitted to the Faculty of the Graduate School of the
University of Maryland, College Park in partial fulfillment
of the requirements for the degree of
Doctor of Philosophy
2010

Advisory Committee:

Prof. Wendell Hill, III, Chairman/Advisor
Prof. Steven Rolston
Prof. Michael Coplan
Prof. Ki-Yong Kim
Prof. Luis Orozco

ACKNOWLEDGMENTS

I am truly grateful to my advisors, Prof. Wendell Hill, III and Prof. Steven Rolston, for the opportunity to conduct my Ph.D. research in their laboratories. I would like to thank them for their patience, guidance and support during years of my graduate studies at the University of Maryland. This work could not be possible without invaluable contribution of my colleagues, Narupon Chattrapiban, Jennifer Johnson, Emily Edwards, Matthew Beeler, Zhao-Yuan Ma and Tao Hong.

A special thanks goes to my friend and colleague Arseni Goussev for his help, advice and optimism.

I would also like to thank the members of my dissertation committee for their useful comments and suggestions.

TABLE OF CONTENTS

LIST OF FIGURES

Abbreviations and Acronyms

NMR	Nuclear Magnetic Resonance
AMO	Atomic Molecular and Optical
BEC	Bose-Einstein Condensate
TEM	Transverse Electromagnetic Mode
Nd:YAG	Neodymium-doped Yttrium Aluminium Garnet
DHB	Dark Hollow Beam
MOT	Magneto-optical Trap
LGB	Laguerre-Gaussian Beam
SLM	Spatial Light Modulator
LVIS	Low-velocity Intensity Source
CCD	Charge-coupled Device
VGA	Video Graphis Array
Ti:Sapphire	Titanium-sapphire
SAS	Saturated Absorption Setup
CNOT	Controlled NOT
SI	International System of Units
FORT	Far-off Resonance Optical Trap
UHV	Ultra-high Vacuum
MCP	Microchannel Plate
AOM	Acousto-optical Modulator
EOM	Electro-optical Modulator
FWHM	Full Width at Half Maximum
OBE	Optical Bloch Equations

Chapter 1

Introduction

1.1 Atom Optics

Atom optics is a study of the manipulation of atoms. In analogy to ordinary optics, electron or neutron optics, the goal is to develop a set of tools to create beams of atoms, reflect, focus, diffract and make the atoms interfere. Atom optics has several advantages over the traditional photon or particle optics based on electrons and neutrons. Unlike electrons, atoms are neutral and therefore less susceptible to stray electromagnetic fields. Being heavier than neutrons, atoms could make better gravitational sensors. Large mass means short de Broglie wavelength on the order of a nanometer and below at low particle energies, opening the possibility of using atomic beams for a high resolution lithography or as precise surface probes. For example, X-radiation has a wavelength in the range of 0.01 to 10 nm, de Broglie wavelength of trapped ultra-cold neutrons is below 50 nm, and cold atoms used in our experiments are characterized by de Broglie wavelength of about 30 nm. Various atoms can be either bosons or fermions, have a large total angular momentum or a magnetic moment compared to electrons or neutrons, and their complex internal structure can interact with external near-resonant electromagnetic fields. Experiments with atomic beams have almost a century-long history [1], but the recent development of laser cooling techniques opened the possibility of increasing beam luminosity at large atomic phase space densities significantly and forming well-collimated, dense atomic beams with well-defined velocity. Atomic

beam sources created using laser cooling are relatively straightforward and inexpensive to implement, especially compared to the nuclear reactor or the spallation neutron source required to create a neutron beam.

The first part of this dissertation is devoted to the development of new elements of atom optics based on blue-detuned high-order Bessel beams. We extended an application of a single Bessel atomic guide to create more complicated interferometer-type structures by demonstrating a *tunnel lock*, a novel device that can split an atomic cloud, transport it, delay, and switch its propagation direction.

1.2 Rydberg Blockade Effect

Quantum information science, a merging of quantum mechanics and classical information theory, opens new exciting possibilities in data computation, communication and storage. Over the last decades, the exponential shrinking of electronic components that process the information may be approaching its limit. The further minituarization of transistors on a near-atomic scales will leave no room for packing more components on a single chip. Quantum mechanics allows us to step beyond this limit, and in combination with information science, can provide a physical system to process information on the microscopic level. Such quantum systems can outperform some of their classical computational counterparts tremendously. Original ideas to exploit the computational power of quantum mechanics [2] and the development of quantum algorithms [3, 4, 5] motivated significant efforts toward the practical realization of a variety of physical systems applicable for quantum information.

Efforts to realize quantum computer hardware, a physical system that provides qubits and gates, are occurring in very different fields, such as NMR [6], linear optics [7], quantum dots [8], cold trapped ions [9] and neutral atoms [10]. One of the promising implementations of quantum computer is the system of neutral atoms, weakly interacting with the environment. The internal level structure can

be used as states of qubits while coupling between qubits can be provided by the dipole-dipole interactions between Rydbergs atoms.

The second part of this dissertation is devoted to the spectroscopic measurements of the Rydberg blockade effect, a conditional suppression of Rydberg excitations depending on the state of a control atom.

1.3 Overview of Dissertation

The Bessel beam project discussed in the first part of the dissertation concerns the engineering of novel tools for atom optics. In particular, we applied a high-order Bessel mode laser beam generated by a spatial light modulator to guide a slow atomic beam of rubidium, and used a combination of two Bessel beams to switch the direction of the atomic beam propagation from one guide to another, thus demonstrating a necessary element for an atom interferometer. The main results of the Bessel beam project consist of the following:

- construction of an experimental apparatus for laser cooling and guiding atoms
- application of a blue-detuned hollow laser beam as an atomic guide
- demonstration of an atomic beam switch by combining two crossed Bessel beams

Chapter 2 of the thesis is devoted to the review of various techniques of guiding and splitting of atomic densities. The experiments reported in this manuscript were performed in 2003-2005, we describe advances in the field up to those years, our contribution to the subject, and also mention most recent progress made by other research groups.

Repulsive optical potentials based on the blue-detuned laser light are discussed in Chapter 3. We discuss various ways to produce the potentials, their applications

for manipulation of atomic densities, and our approach to generate Bessel beams with a spatial light modulator.

The subject of the dissertation, guiding and splitting of a slow atomic beam of rubidium is reported in Chapter 4. We first discuss the application of a single blue-detuned Bessel beam to guide an atomic beam along the direction of gravity. The properties of this type of guide were investigated for various parameters of the hollow beam, such as the detuning from an atomic resonance, size and the order of the Bessel beam. We then report a first-time demonstration of an atomic beam switch based on the combination of two crossed Bessel beams. We measure the efficiency of the switch and investigate the heating processes induced by the switch. We also report other applications of crossed Bessel beams, such as a 3-D optical trap for atoms confined in the intersection volume of two hollow beams and a splitter of the atomic density.

The Rydberg blockade project is covered by Chapters 5, 6 and 7. Chapter 5 introduces the application of neutral Rydberg atoms for quantum computing. There, we describe various approaches to enhance the atom-atom interactions required for fast quantum gates along with the recent experimental progress.

Chapter 6 is devoted to description of the experimental apparatus we built to excite Rydberg transitions and investigate Rydberg-Rydberg interactions.

Finally, in Chapter 7 we report the first experimental results obtained with the our experimental apparatus. The main results of the Rydberg blockade project consist of the following:

- construction of a narrow-band laser system for Rydberg excitations
- spectroscopic measurements of Rydberg states to observe signatures of the Rydberg-Rydberg interactions

As the laser cooling technique became a standard tool of AMO Physics nowadays, we assume that most readers are quite familiar with the subject. Thus, the

details of the more common knowledge, such as main aspects of atom-light interactions, selected properties of rubidium, building and control of the cold atom apparatus are all collected in the Appendices.

Chapter 2

Review of Guiding and Splitting Experiments

Chapter 2 is devoted to a review of various experimental approaches to create a set of atom optics tools that would allow manipulation of slow velocity atomic beams. This review does not cover control over hot[1] beams of atoms, although that branch of atom optics is quite fruitful [11]. Most of the experiments described below were aimed at designing guides for cold atoms and atom optics analogs for optical mirrors, lenses and beam splitters. One incentive was the creation of an atomic interferometer (using atoms of mass m_a and velocity v) that can be more sensitive to inertial or gravitational effects [12] than the traditional optical counterpart (using photons of energy $\hbar\omega$ or wavelength λ_{ph}) of the same geometry, by a ratio of the order of $m_a c^2/\hbar\omega = \lambda_{ph} c/\lambda_{db} v$, where λ_{db} is the de Broglie wavelength of atoms. Large-area interferometers require not only well-controlled atomic beam-splitting but also reliable transfer of atomic densities over large distances. Another exciting area of application of atomic guides is quantum information science: ensembles of atoms as collections of quantum bits can be transported in space using atomic guides as buses for quantum computers and wires for atom squids. Another promising application of atom optics includes lithography, where

[1]We call atomic beams or sources *hot* if their equilibrium or characteristic temperature is close to or above the room temperature. We refer to *cold* atoms as to those slowed down using laser cooling techniques. Those atoms usually have temperatures below 1 mK but their velocity distribution is still Maxwellian (thermal) opposed to degenerate gases (such as BEC) that are not considered in this dissertation.

the deposition resolution, $\lambda/2$ is not limited by optical wavelengths. We should point out, that with the development of the field, many experiments investigated more fundamental issues, such as properties of matter-waves among many other results of quantum physics.

Motion of neutral atoms can be controlled through the interaction of their internal structure with an external electromagnetic field. Absorption and consecutive emission of photons may change the atom velocity both in direction and a magnitude. Light forces are considered in some detail in Appendix A. Spontaneous emission gives rise to a radiation pressure force that may both accelerate or decelerate atoms, but, due to its random nature, results in the phase decoherence of an atomic wavefunction, which can be fatal for quantum information application. Stimulated emission produces the conservative dipole force that allows the direction of atomic velocity to be changed coherently. The radiation pressure force is essential for laser cooling, but we will only rely on the dipole force to manipulate atoms while trying to reduce the effects of radiation pressure as much as possible. Another approach to control the atoms relies on the interaction of the internal magnetic moment of an atom with an external magnetic field. In this review we separate the all-optical control via light-matter interactions from that via magnetic interactions, as the two approaches have different experimental realizations and their own intrinsic advantages and drawbacks. It is, however, sometimes experimentally advantageous to combine the two methods together by appropriate tailoring of the magnetic and optical potentials [13].

We first briefly describe various experiments to control the motion of cold atoms by magnetic interactions with a special attention to a splitter based on a current-carrying wire. A direct comparison can be done between this device and an all-optical atomic beam switch, the subject of the dissertation. The motion control through the light-matter interactions is the major interest of the review. Manipulation based on both the attractive red-detuned and repulsive blue-detuned optical potentials is discussed in detail.

2.1 Magnetic Interactions

Ions can be successfully manipulated with external electromagnetic fields. To control neutral atoms, one can rely on the much weaker interaction between the atom magnetic moment $\boldsymbol{\mu}$ and an external static magnetic field $\boldsymbol{B}$ that gives rise to the interaction potential $V_{mag} = -\boldsymbol{\mu} \cdot \boldsymbol{B}$. For example, this potential is below 1 K for rubidium at moderate magnetic fields of less than 2 T, and therefore such an approach can be applied to slow atoms only, and has to be realized in combination with laser cooling techniques. An early review of various ion/neutral atom trap configurations is given in Ref. [14]. For $V_{mag} < 0$, the atoms can be trapped in a local 2-dimensional field maximum while moving unconstrained along the third dimension. A simple example of such a neutral atom trap configuration is a current-carrying wire that was further developed into more complicated and much smaller fabricated magnetic microtraps, or atom chips. This approach is very tempting for atom interferometry purposes as the individual interferometer elements not only can be precisely and reproducibly made, but also combined together on a single chip to extend to multicomponent experiments.

2.1.1 Guiding Along Wire with Current

For a straight wire, the atom moves along the wire freely with its thermal velocity. The motion in the plane transverse to the wire is constrained by magnetic interactions and would follow a Kepler orbit if the orbiting frequency were smaller than the Larmor precession frequency (rotation of magnetic moment around the direction of the magnetic field). The resulting trajectory spirals around the wire. Trapping neutral atoms by the $1/r$ magnetic field of a current-carrying wire was proposed and implemented for atom guiding by Schmiedmayer [15]. His group has later used this approach to guide cold atoms [16]. A 1.6 mm lithium cloud was laser cooled down to temperature of 200 μK and released from the magneto-optical trap in the vicinity of a 50-μm thick and 10-cm long tungsten wire carrying a current of

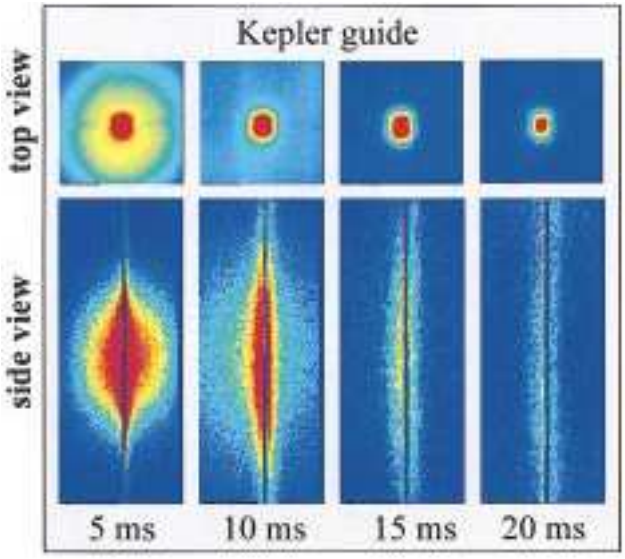

Figure 2.1: Density distributions of lithium atoms trapped by the magnetic field of a current-carrying wire for various trapping times from reference [16]. Top row of images show the distribution across the wire integrated along it; bottom images represent the distribution along a 2-cm portion of the wire integrated across the wire.

1 A. Atoms with the appropriate direction of the magnetic moment were trapped by the magnetic field of the wire and then guided along the wire. Measured density distributions along the wire and in the plane transverse to the wire are presented on Fig. 2.1. The Kepler guide loading efficiency was about 10% (2×10^6 atoms).

Better control over atomic motion can be achieved by tailoring several magnetic potentials together. Combination of a Kepler guide with a bias magnetic field produces so-called "side guide" [16] where atoms precess along the field minimum and move alongside the wire. More complicated structures, consisting of two wires and a bias field, were realized to provide omnidirectional guiding along a spiral path [17]. Further miniaturization of the guiding structures created by lithographic techniques led to microtraps/guides where atoms can be held in steep magnetic potentials very close to material surfaces. For example, cold rubidium

atoms were guided 50 μm above a curved 10-cm long track made of two 100 μm cross-section copper wires deposited on a glass substrate using electroplating techniques [18]. Furthermore, recent advances in nano-technology suggest the possibility of trapping neutral atoms sub-micron distances away from a dielectric substrate containing carbon nanotubes [19].

2.1.2 Magnetic Beam Splitter

One example of magnetic microtraps is a magnetic beam splitter [20]. Its purpose is similar to the subject of this dissertation, the atomic beam switch, and therefore it is interesting to discuss the properties of this device. A side guide arrangement was extended to a Y-shaped wire in the presence of a bias magnetic field. As a result, the atoms could either follow a specific arm of the wire or be split between the two arms. Fig. 2.2 presents a photograph of fluorescing atoms for different modes of operation of the device (panel (b)). The blue images show the atoms following either one of the arms and a 50/50 splitting between the two arms. The splitting ratio is determined by the current ratio between two arms and is presented on the right panel of Fig. 2.2. The separation angle between two arms was 15° and more than than 1×10^6 lithium atoms were loaded and split by this device. It is worth mentioning, that this device can be used to split atomic density; the splitting of the wavefunction would require a single mode operation of the device for a given de Broglie wavelength.

Atom interferometry requires bright atomic sources and Bose-Einstein condensates (BEC) are ideal for this purpose. Guiding BEC clouds on a microtrap has been demonstrated along with the splitting by a double-well potential [21, 22], and the splitting, reflecting, and recombining of condensate atoms by a standing-wave light field [23]. The area of the prototypes was quite small, which reduces the sensitivity of an interferometer. For example, a phase shift, ϕ_s, between two arms of the Sagnac atom interferometer is proportional to its area, A, according

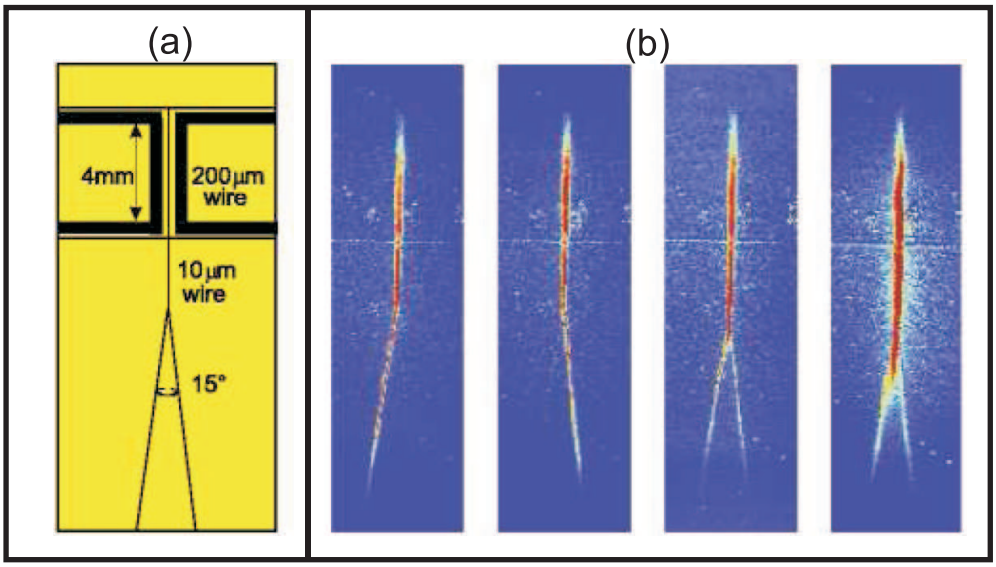

Figure 2.2: Beam splitter on a chip: (a) chip schematic (right) and (b) fluorescence images of guided atoms (right). Atoms can be guided along either of arm of the Y-shaped wire or split into both sides as they move along the wire with their thermal velocity [20].

to $\Delta\phi_s = 2m\Omega A/\hbar$, where m is the atomic mass, and Ω is the rotation frequency. In additional, guiding along a microchip has a serious problem: for a small cross-section wire, any material imperfection causes deviation of the currents from a straight line that results in fluctuation of the magnetic field large enough to produce a break-up of the BEC cloud. Close proximity of the cloud to the material of the chip is another issue: van der Waals interactions can cause decoherence (*e.g.*, spin flips) of the atomic ensemble. Microtraps imply permanent design and thus lack some flexibility as the fabricated chip must be positioned appropriately with respect to the source of the cold atoms in advance to optimize the loading efficiency; after that, any modification of the experimental setup that is under ultra-high vacuum might be challenging. Finally, only atoms with the specific magnetic moment can be manipulated by the external magnetic field.

2.2 All-optical Control

A different approach to controlling the atomic motion relies on the interactions between an external electric field (laser light) and the induced dipole moment of the atom. This approach reduces the coupling between the investigated system and the environment as atoms can be manipulated far away (compared to short ranges of the van der Waals potentials) from the materials of the chamber walls; the arrangement of the laser beams can be modified outside the vacuum system, optical potentials of arbitrary shapes can be modified in real time, for example, using a spatial light modulator. Optical dipole traps are especially interesting for trapping atoms with arbitrary magnetic sublevels, or trapping several atomic species simultaneously. Optical control has a strong limitation: laser beams propagate along straight lines in free space. Various techniques to manipulate atoms by light are described in the next section.

A microscopic particle suspended in a medium of refractive index n_0 and polarized in the presence of the external electric field $\boldsymbol{E}$ is subject to a force due to the interaction between the field and the induced electric dipole moment[2]. Classically, the force expressed as a gradient of the interaction potential is given by

$$\boldsymbol{F}_g = -\frac{1}{2} n_0 \alpha \nabla \boldsymbol{E}^2, \tag{2.1}$$

where α is the particle's polarizability and n_0 is the refractive index of the medium in which the particle is suspended. With laser light sources, the gradient force (Eq. 2.1) traps microscopic dielectric particles in a tightly focused Gaussian laser beam [24]. For a large electric field gradient the particles are attracted to the beam focus, and the gradient force can dominate gravitational forces, Brownian motion, and forward-scattering light force, and trap the particle in 3-D [25]. This type of trap, referred to as optical tweezers, was later extended to hollow laser beams [26]. Optical tweezer is a non-contact method to manipulate macroscopic objects and is

[2]Electric field is low, such that the higher order processes can be neglected

especially powerful for biological applications [27]. Some hollow laser beams, such as Bessel beams, possess orbital angular momentum that can be transferred to the particles and cause them to rotate (optical spanners) [28]. Blue-detuned optical potentials are especially promising as optical tweezers: the null intensity of the on-axis region reduces the light-scattering force. That minimizes the optical damage to the trapped particles, which is particularly important for trapping biological samples.

A microscopic particle, such as an atom, in the presence of a near-resonant laser light field is subjected to the dipole force as a result of the interaction between the field and the induced dipole moment of the atom (for details refer to Appendix A). The force can be either attractive or repulsive depending on the sign of the light detuning from an atomic resonance. The magnitude of the dipole force depends on the spatial gradient of the light intensity. This leads to the possibility of either trapping atoms in the regions of the maximum light intensity (attractive potential) or confining them in the dark region of the minimum intensity surrounded by light (repulsive potential); but in both cases the spatial variation of the light intensity has to be large. For example, atoms placed in a Gaussian (TEM_{00}) laser beam will be pulled to the beam axis in the transverse plane of the beam and attracted to the beam focus in the longitudinal direction as described in Ref. [29]; for a higher-order Bessel (dark-core hollow beam) atoms can be confined in the dark core and move freely along the beam as reported in Chapter 4 of this thesis.

In most cases one tries to suppress the absorption from the trap light by detuning its frequency, ω, far from an atomic resonant frequency, ω_a (on the scale of the inverse lifetime, γ, of an upper level of a two-level system), because the photon scattering rate scales as $1/\delta^2$ (Eq. A.26), where detuning $\delta = \omega - \omega_a$. For the moderate light intensities, $I(\boldsymbol{r})$, the expression for the potential associated with the dipole force exerted on a two-level atom (Eq. A.45) can be simplified to

$$U(\boldsymbol{r}) = \frac{1}{2}\hbar\delta\frac{I(\boldsymbol{r})/I_s}{4(\delta/\gamma)^2}, \tag{2.2}$$

where the saturation intensity $I_s \equiv h\pi c\gamma/3\lambda^3$ [30], and λ is the wavelength of light. The dipole potential scales as $1/\delta$, and for a large detuning and a given light intensity one can achieve the desired value of the potential, while suppressing heating due to the absorption over the time of an experiment.

The dipole force as the gradient of the potential relies on the spatial variation of the light intensity $I(\boldsymbol{r})$ that allows for various trap configurations. For example, atoms can be moved along a straight line in free space using a red-detuned Gaussian laser beam. In this configuration the atoms are trapped in three dimensions at the beam focus: a Gaussian intensity distribution characterized by the beam's waist size provides a tight confinement in the transverse plane while a less tightly confining optical potential (limited by the beam's Rayleigh range) holds the atoms in the longitudinal direction. The position of the beam focus and thus the trapped cloud can be moved by means of a relay optics. As discussed in Section 2.2, for large enough detunings the scattering rate can be kept low, while the required optical dipole potential can be achieved for higher laser light intensities according to Eq. 2.2. For instance, a BEC cloud of 10^6 rubidium atoms can be trapped at a focus of a 15 W fiber laser at 1567 nm with the waist of 40 μm (the Rayleigh range of 3.2 mm) and routinely moved over a distance of tens of centimeters [29].

2.2.1 Hollow Core Optical Fiber Guides

Guiding atoms along laser beams in free space is limited to straight lines. One can avoid this constraint by employing a hollow-core optical fiber. For efficient guiding, the atoms must be kept away from the dielectric material that contains the light in the fiber. That implies that the optical potential has to be higher than the sum of the kinetic energy of the atoms in the plane transverse to the fiber[3]

[3]Assuming that longitudinal and transverse velocities are comparable

and the short-ranged van der Waals attractive potential between the dielectric and the atoms. Light can be mode-matched with a hollow core fiber to either propagate along the core, in vacuum, surrounded by a cylinder of the dielectric or can be internally reflected by the dielectric and travel inside the walls of the hollow cylinder of a dielectric material. The first configuration in combination with the red-detuned light creates an optical potential attracting atoms to the dark core of the fiber, while the second pushes the atoms away from the dielectric walls for the blue-detuned laser light. The red-detuned guiding of atoms inside a hollow core optical fiber is similar to that by a Gaussian beam: intensity gradient in the transverse plane attracts atoms to the maximum of the light field creating a 2-dimensional trap. As atoms are mostly trapped along the axis of the fiber and far from the walls, the van der Waals interaction is low. The red-detuned guiding was experimentally demonstrated by Renn, *et al.* [31], who used a 3 cm long capillary hollow core fiber to transport hot atoms from one vacuum chamber to another. Supported light modes for this type of the optical fiber decay exponentially with the fiber length thus severely limiting the guiding distance, while a high light intensity required for the on-axis trapping leads to a significant heating of the atoms. A strong electric field attenuation can be avoided by the use of a photonic crystal fiber. The band gap structure of the fiber reduces the propagation loss thus potentially improving the red-detuned guiding distances. Preliminary experiments with microscopic dielectric particles [32] show some promise to apply the photonic crystal fibers for atom guiding.

For the case of the blue-detuned hollow fiber guide, light propagates inside the dielectric and its intensity exponentially vanishes into the dark core over a distance of about $\lambda/2\pi$. Such evanescent light fields characterized by a large spatial gradient can be used to expel the atoms from the high-intensity region near the fiber wall and guide them along the fiber [33]. In the cited experiment, the laser power of 500 mW tuned blue of rubidium D_2 line provided a maximum optical potential depth of 22 mK large enough to constrain the transverse atomic motion and exceed the

attractive van der Waals potential. The guiding experiment was later extended to a laser-cooled atomic sample [34]. In contrast with the red-detuned fiber guides, the evanescent field potential is generated by lossless modes of light making the application of long blue-detuned fiber guides more practical. Moreover, as with any blue-detuned optical potential, atoms spend most of their time in the low-intensity region, and therefore decoherence or heating of atoms due to spontaneous emission can be kept small for the evanescent field guides. In addition to the evanescent field potential, it should be possible to propagate doughnut-type modes in photonic hollow core fibers. We made a few unsuccessful attempts to exploit that idea, which is promising and should be investigated more in the future.

The use of hollow core optical fibers offer several advantages over other methods of guiding atoms. A guiding path is not limited by a straight line as the fiber can be bent[4]. A hollow fiber guide can be used to connect two separate vacuum chambers. Moreover, as the fiber dielectric is transparent at optical frequencies, the atoms inside the fiber can be probed outside of the vacuum system by a high numerical aperture optical system. Unfortunately, the input/output coupling of both atoms and the light with the fiber is quite challenging as it has to be done inside the vacuum chamber thus limiting the flexibility of the experimental setup.

2.2.2 Free-space Red-detuned Atomic Guides

Early guiding of an atomic beam along a red-detuned Gaussian beam was reported by Bjorkholm, *et al.* [35]. A thermal beam of sodium atoms was focused and steered by a co-propagating red-detuned laser beam, and de-focused by a blue-detuned beam. The experimental arrangement was limited by small detunings

[4]The transverse guiding force must provide adequate centripetal force. The tightest bend radius is given by $R_{min} = mr_0v_z^2/U(0)$, where m is the mass of the atom, r_0 is the radius of the light mode propagating in the fiber, v_z is the atomic velocity along the fiber, and $U(0)$ the value of the optical potential on the axis of the fiber [31]

(less than $10^3\gamma$ in Eq. 2.2) at a relatively low laser power (50 mW) resulted in significant heating. With the technological advances in laser manufacturing, the problem of heating was addressed by using far-detuned high power laser beams to guide atoms loaded from an atomic fountain [36] and a MOT [37]. In the second experiment, rubidium atoms were released from optical molasses and fell in the gravitational field of the Earth in a red-detuned Nd:YAG laser beam at 1064 nm with a corresponding detuning of $1.6 \cdot 10^7\gamma$. A 40 % loading efficiency was reported. The laser power of 15 W focused into a beam waist of 100 μm provided a dipole potential of 100 μK in the transverse plane with the maximum scattering rate[5] of 1 s^{-1}.

2.2.2.1 Red-detuned Beam Splitters

A combination of two red-detuned Gaussian beams can be applied to guide the atoms along one of the beams and then split the cloud into two separate propagation directions by a second beam [38]. In this demonstration a rubidium cloud of 10^7 atoms cooled down to 14 μK was released from optical molasses and fell in a vertical guide (Fig. 2.3) composed of a fundamental mode of Nd:YAG laser. The 14 W collimated beam of 400 μm in diameter created an optical potential of 30 μK in the transverse plane and provided a loading efficiency of 10% from the molasses. In 29 ms after the cloud release, the second, *oblique guide* (10 W, 600 μm diameter collimated Nd:YAG laser beam) was turned on, when the cloud reached the intersection region of the two beams, 4 mm below the molasses. As an atom oscillated across the intersection region in a two-well potential, it could end up in either of the guides. For the two beams crossed at about 7°, this device provided a splitting efficiency of 29%.

The two-crossed guides experiment was later extended to demonstrate more

[5]Number of photons absorbed and spontaneously emitted per unit time per atom. Note, that $E_{rec} = 3.6\ \mu K$ for rubidium D_2 line

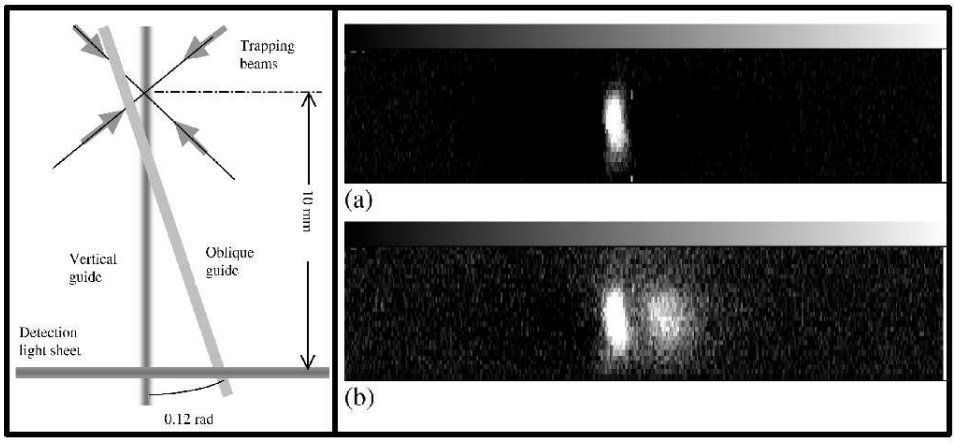

Figure 2.3: The schematics of the red-detuned beam splitter (left), and the pictures of the cloud, imaged for the vertical guide (a) and for two guides (b). Reproduced from Ref. [38].

complicated structures such as an array of crossed red-detuned laser beams for atom guiding [39]. A cylindrical lens transforms a round Gaussian beam into an elliptical one with a large aspect ratio, and can be used as an atom guide in the focal plane of the lens. A set of cylindrical microlenses provides a parallel array of the guides while the second set rotated with respect of the first creates a 2-dimensional mesh of light that can be used to split, guide and recombine the atomic densities. A fluorescence image of atoms loaded onto such an interferometer-type structure is presented in Fig. 2.4. By proper control of the intensity at the intersection points one can employ this structure as either Mach-Zehnder or Michelson interferometers. The angle between the arms of the interferometer could be adjusted by mutual rotation of the lens arrays, but the interferometer area of 1 mm^2 was quite small.

2.2.3 Free-space Blue-detuned Atomic Traps

In case of the blue-detuned laser light, the corresponding optical potential is repulsive, and atoms can be confined within the dark region surrounded by light. Practically, this can be achieved by coupling atoms with laser beams of zero central

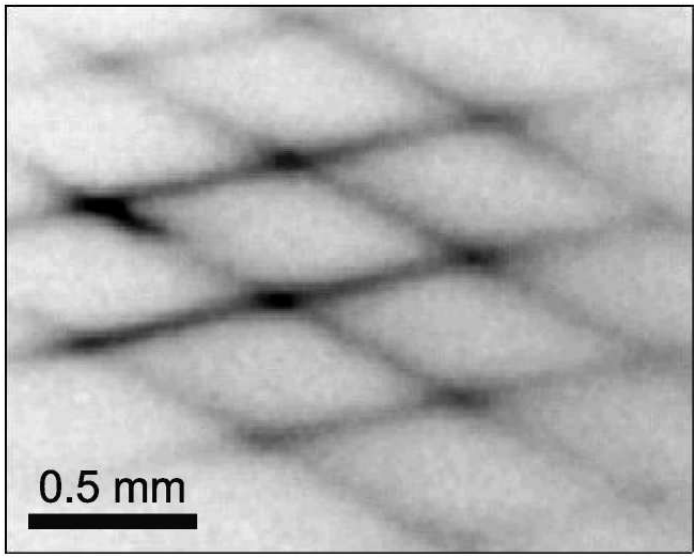

Figure 2.4: Fluorescence image of rubidium atoms loaded from a MOT into a multiple-path Mach-Zehnder type guiding structure created by the combined dipole potentials of two sets of microfabricated arrays of cylindrical lenses. Reproduced from Ref. [39].

intensity, so-called dark hollow beams (DHBs). Among those are high-order Bessel-Gaussian, Laguerre-Gaussian, high-order Mathieu and doughnut hollow beams. The properties of the various DHBs and techniques of their generation were discussed in some detail by Yin, *et al.* [40]. Some aspects of the diffraction theory applied to the hollow beam generation are discussed in Appendix B. As atoms in the blue-detuned optical potentials are trapped in the dark regions, they experience a low photon-scattering and photon-assisted-collision rates, and suffer minimal light-shift effects of atomic levels. Being all-optical, DHBs can trap and transport atoms far from material walls thus suppressing attractive van der Waals interactions.

The first applications of the DHBs as atom traps were experimentally demonstrated with the development of laser cooling techniques. In a doughnut-beam trapping scheme [41], a 3-dimensional dipole trap consisted of a blue-detuned

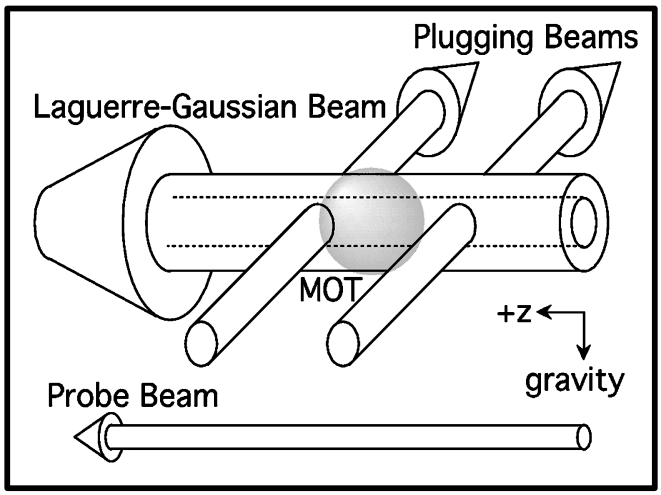

Figure 2.5: Schematic illustration of the novel optical trap: an atom cloud is confined transversely inside a Laguerre-Gaussian beam and longitudinally by two blue-detuned plugging beams. Reproduced from Ref. [41].

Laguerre-Gaussian beam and two blue-detuned plug beams transverse to the hollow beam (Fig. 2.5). Such configuration provided a maximum optical potential of 40 μK, high enough to trap 10^8 rubidium atoms laser-cooled to 10 μK. In yet another variation, the gravito-optical surface trap, cesium atoms were confined inside a DHB and held by a blue-detuned evanescent light in the gravity field [42]. Cold metastable xenon atoms were captured in a dark region of space inside a single blue-detuned hollow laser beam formed by an axicon [43], a lens which has a conical surface. The trap region was an elongated diamond of revolution with a diameter of roughly 1.5 mm and 150 mm of length corresponding to a volume of about 80 mm^2, where up to one million atoms were confined. Since then, various configurations for the blue-detuned atom traps and refrigerators were proposed and demonstrated [40] to investigate the possibility of effective evaporative cooling towards BEC. However the achieved phase-space densities of $\sim 3\times10^{-4}$ are too low for BEC production, and the blue-detuned traps do not compete with the standard evaporation cooling techniques in magnetic [29] or red-detuned dipole [44] traps.

2.2.4 Free-space Blue-detuned Atomic Guides

Cylindrically symmetric blue-detuned DHB are ideal candidates to transport atoms along their dark core. Various types of hollow beams can be applied as atomic wave guides, atomic funnels, atomic motors, beam collimators and splitters. In one of the earliest demonstrations, a hologram generated LG-beam was employed to guide an atomic beam of neon for about 30 cm and focus it to a radius of 6.5 μm [45]. At the same time, rubidium atoms from a MOT fell in the gravitational field inside a LP_{01} beam generated from an output of a hollow-core optical fiber [46]. Guiding cesium atoms over a 20 cm distance was reported for an axicon-generated hollow beam with a 10% efficiency limited by the collisions with the background vapor [47]. A TEM_{00} laser beam was converted into a DHB with three axicons ($A_{1,2,3}$) and a spherical lens (L) as shown on the top inset of Fig. 2.6 along with a photograph of the transverse beam profile, and the corresponding intensity distribution. A guiding efficiency of 50% was achieved for a LP_{01} beam generated from an output of a hollow-core optical fiber for the atoms falling in gravity over a 10 cm distance [48].

An axicon-generated DHB, being a mixture of high order Bessel modes, preserves its shape over a limited distance and does not posses phase singularity on its axis, the property required for non-vanishing null on-axis intensity of the tightly focused beam. On the contrary, a pure high order Bessel beam is diffraction-free, has on-axis phase singularity, and thus is very useful as a waveguide and funnel. A Bessel beam can be generated with a 2-dimensional spatial light modulator (SLM) [49], and was shown to be successfully employed as an atom tunnel [50]. Moreover, using the SLM allows creation of arbitrary 2-dimensional optical potentials[6], that can be used as billiards or scatterers for atomic wavepackets to study the connection between classical and quantum chaos [50, 51].

[6]Continuity of the potential is limited by the resolution of the SLM, which is a digital instrument.

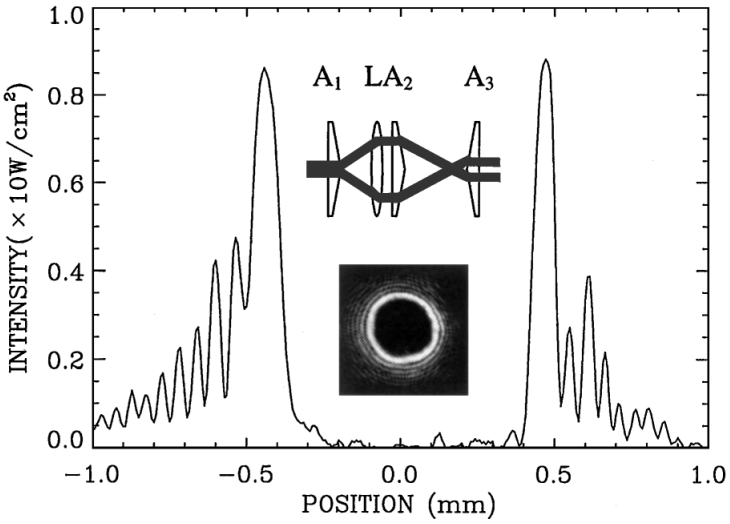

Figure 2.6: 1-mm hollow-core beam intensity distribution at the position of the MOT (graph and bottom inset) and optical components for hollow-core beam generation (top inset). Reproduced from Ref. [47].

With the advent of the experimental realization of Bose-Einstein condensates, the application of the blue-detuned optical potentials for manipulation of BEC, especially creation of a single-mode waveguides, was investigated both theoretically and experimentally. In particular, a blue-detuned Laguerre-Gaussian (LG) beam was used to realize a BEC waveguide to investigate dynamic evolution of matter waves in the loading and waveguiding processes [52]. In this demonstration, a 100% loading efficiency from a magnetically trapped BEC to a 10 μm LG beam was achieved. It has been shown that due to non-adiabatic transfer, a few transverse modes of the waveguide were occupied, leading to longitudinal heating.

For interferometry applications, one has to be able not only to guide atoms, but also to split the wavefunction of the atom, and deflect an atomic beam. One of the first experiments towards interferometry-type structures using blue-detuned optical potentials demonstrated guiding and splitting of a low-velocity intense source of atoms (LVIS) [53] using an axicon generated DHB [54]. The hollow beam was overlapped with the rubidium vapor MOT at angle of 8° with the LVIS beam and

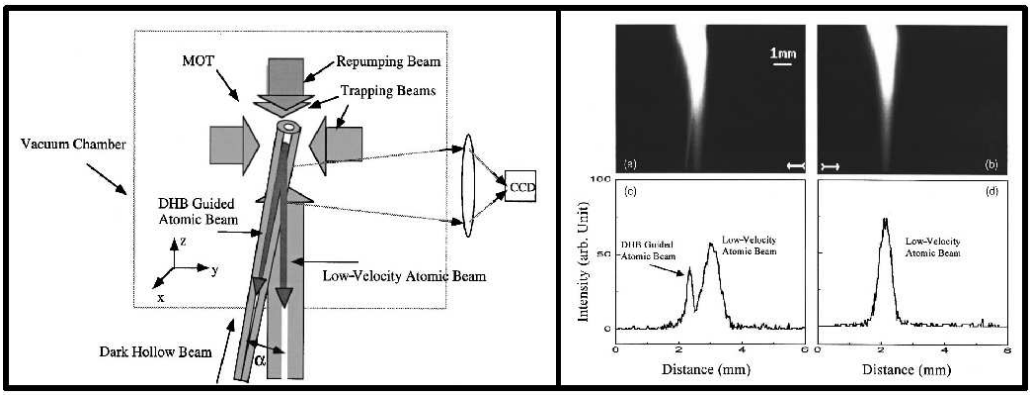

Figure 2.7: Schematic of the low-velocity beam splitter (left), and (a) CCD image of rubidium beam split and guided by the DHB. (c) Spatial profile of the rubidium beam taken at the location indicated by the arrow. For comparison, (b) and (d) show the corresponding image and the spatial profile without the DHB. Reproduced from Ref. [54]

.

directed along the gravity field. Atoms originally inside the hollow beam propagated along it while those outside the guide followed the direction of LVIS beam due to the radiation pressure imbalance in the MOT beams. For this experiment, a spatial separation of the two atomic beams was demonstrated (Fig. 2.7), with the atomic flux in the hollow beam to be 50% of that of a single LVIS beam[7].

[7]Note, that the diameter of the guided atomic beam is smaller than that of the LVIS, and therefore the total number of atoms in the DHB was smaller that half of the atom number in a single LVIS.

Chapter 3

Generation of 4th Order Bessel Beam for Atom Guiding

Chapter 3 describes approaches to generate blue-detuned optical potentials suitable to transport cold atoms over long distances. Here we discuss advantages and limitations of the various hollow beam generation techniques, and described the experimental setup we used to create a 4th-order Bessel beam.

3.1 Requirements on Blue-detuned Guides

A blue-detuned optical potential is repulsive: atoms are confined in a dark region surrounded by light. The simple way to create such an intensity pattern is to block the central part of a Gaussian beam with an opaque disk or by using a mirror with a small hole to reflect a Gaussian beam. This approach has two main disadvantages that make this approach impractical. Because of the power loss, the conversion efficiency is low, and the radial intensity distribution along the beam is not preserved, as its propagation is governed by Fresnel or Fraunhofer diffraction of the disk (hole), while the distribution of the remaining part is still Gaussian. When choosing an appropriate hollow beam to guide atoms one wants to avoid those limitations and have both the high conversion efficiency and conservation of the beam transverse profile along the propagation direction. The most common way to generate a dark hollow beam (DHB) relies on a mode conversion of a TEM_{00} laser cavity mode into a desired superposition of another complete set of

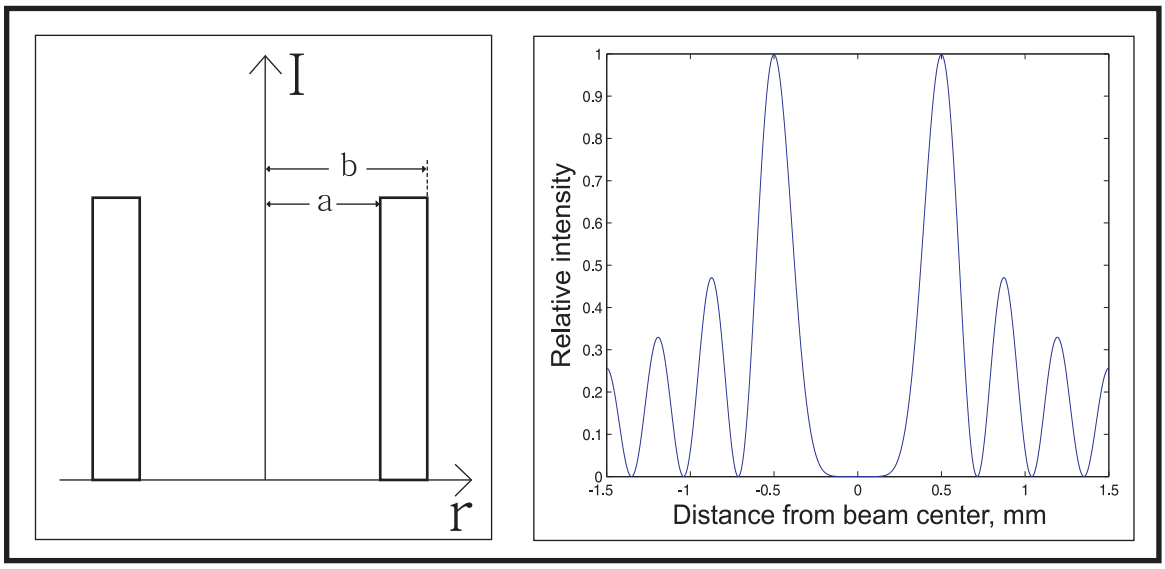

Figure 3.1: Ideal dark hollow beam of inner diameter $2a$ with double-rectangular $(b-a)$ wide transverse intensity profile $I(r)$ (left), and a normalized transverse profile of a 1 mm diameter, 4th-order Bessel beam at 780 nm (right).

optical modes. However, a hollow beam can be generated directly from a properly designed laser cavity if the TEM_{01}^{*}[1] is predominantly excited [55]. In addition, the magnitude of the repulsive force is larger for a steeper optical potential and thicker guide walls reduce probability of tunneling through the walls. The ideal candidate for an atomic guide would be a double-rectangular-profile hollow beam with the rectangular transverse intensity distribution, $I(r)$ invariant along the beam axis (Fig. 3.1). Such a beam has not been generated yet. The practically generated hollow beams are designed to have transverse profiles similar to the rectangular beam, and are characterized by the intensity profile $I(r)$, and the inner and outer diameters a and b. As an example, a normalized transverse profile of a 1 mm diameter, 4th-order Bessel beam at 780 nm is plotted in Fig. 3.1, right. The beam radius is defined as the position of the first maximum of the Bessel function.

[1]The TEM_{01}^{*} is a superposition of TEM_{01} and TEM_{10} modes with a relative phase shift of $\pi/2$

For some applications, such as lithography, it might be desirable to be able to focus a hollow beam while preserving zero electric field on the beam axis. In general, this can only be done for a hollow beam with a phase singularity along its axis, such as a high-order Bessel beam. A high-order Bessel beam is a diffraction-free, hollow laser beam, and its field amplitude is given by

$$E_n(r, \phi, z) = \frac{A}{w(z)} J_n(k_r r) e^{ik_z z} e^{in\phi}, \tag{3.1}$$

where A is a normalization constant, $w(z) = w_0\sqrt{1 + (\lambda z/\pi w_0^2)^2}$ is the beam waist at z (w_0 being the beam waist at $z = 0$), k_r and k_z are the transverse and longitudinal components of the wavevector, and J_n is the nth-order Bessel function. This beam carries infinite amount of energy. Practically, the transverse profile should be modified by a Gaussian function, thus forming a real Bessel-Gaussian beam (BGB)[2][56]. The electric field amplitude for a linearly polarized nth-order BGB is given by

$$E_n(r, \phi, z) = \frac{A}{w(z)} J_n(k_r r) e^{ik_z z} e^{in\phi} e^{-\frac{r^2}{w^2(z)}}. \tag{3.2}$$

Atoms are usually confined within the first ring of light in guiding experiments, and for a nearly collimated Bessel beam of a 1 mm diameter its propagation is nearly diffraction-free as $w(z) \gg r_0$, where r_0 is radius of the first ring. Under these experimental conditions, the first ring of the Bessel-Gaussian beam matches that of the Bessel beam.

3.2 Generation of Bessel Beams

There are three main approaches to generate a Bessel-Gaussian beam: the geometric optical method, the optical holographic method, and the computer-generated

[2]This is an approximation. The electric field given by Eq. 3.2 does not satisfy the wave equation.

holographic method. They rely on a mode conversion of a Gaussian or a Laguerre-Gaussian (LGB) laser beam into the Bessel beam. All three methods can be understood in terms of the scalar diffraction theory outlined in Appendix B. Here we briefly describe the basics of each generation technique with the emphasis on the versatile computer-generated holographic method implemented with a spatial light modulator. This particular approach has been used to create the Bessel beams discussed in the dissertation.

The geometric optical method can be applied to generate a Bessel beam by illuminating an axicon, a lens with a conical surface, with a LGB [57]. In this case, the field distribution behind the axicon placed at the waist of the LGB is given by the Fresnel diffraction integral, and the resulting intensity distribution in the transverse plane behind the axicon is proportional to

$$I(r,z) \propto z^{2n+1} exp(-\frac{2z^2}{z_{max}^2}) J_n^2(k_r r), \tag{3.3}$$

where z_{max} is a "propagation distance" defined by

$$z_{max} = w_0 k/k_r, \qquad k_r = k(n-1)\gamma_a, \tag{3.4}$$

where n and γ_a are the refractive index and a small internal angle of the axicon, respectively. According the Equation 3.3, the generated beam approximates a Bessel beam of order n close to the optical axis and within the "propagation distance" z_{max}.

The optical holographic method is based on the mathematical connection between Bessel beams of the adjacent order. In the integral representation, the zeroth-order Bessel function can be written as

$$J_0 = \frac{1}{2\pi} \int_0^{2\pi} e^{ix\,sin\theta} d\theta, \tag{3.5}$$

while the nth-order Bessel function is given by

$$J_n = \frac{1}{2\pi}\int_0^{2\pi} e^{i(x\,sin\theta - n\theta)}d\theta. \tag{3.6}$$

In particular, the first-order Bessel beam can be expressed as

$$J_1 = \frac{1}{2\pi}\int_0^{2\pi} e^{-i\theta}e^{ix\,sin\theta}d\theta. \tag{3.7}$$

Experimentally, the $e^{-i\theta}$ factor in the integrand of the Eq. 3.7 can be obtained by adding a circular wedged phase plate (*e.g.,* a transparent plate of a variable thickness) to the configuration of J_0 beam [58]. In this case, the phase plate could be a disk whose optical thickness increases linearly with the polar angle.

A plane-wave (large collimated Gaussian laser beam) illuminating a phase mask given by a transmission function

$$T(r,\phi,0) = \begin{cases} e^{in\phi}e^{-ik_r r} & r \le r_0, \\ 0 & r > r_0, \end{cases} \tag{3.8}$$

is converted into a beam-like wave field with a Bessel transverse intensity profile $|J_n(k_r r)|^2$ within the propagation-invariant distance given by

$$z_{max} = \frac{1}{k_r}\frac{\pi D}{\lambda}. \tag{3.9}$$

Here D is the diameter of the hologram, λ is the wavelength of light, (r,ϕ) are the polar coordinates in the plane $z = 0$ of the hologram, and k_r is a radial spatial frequency of the Bessel beam of order n, as defined in Eq. 3.4.

The transmission function (3.8) can be realized by a dielectric disk whose optical thickness varies as $(-k_r r + n\phi)$ in polar coordinates. The order n of the Bessel beam is determined by the integral number of full revolutions around the mask center to produce the phase shift of 2π. The radial spatial frequency k_r sets the position of local maxima of the Bessel function, and thus the diameter of the first ring. A separate dielectric disk needs to be manufactured for each set of mask parameters (n, k_r).

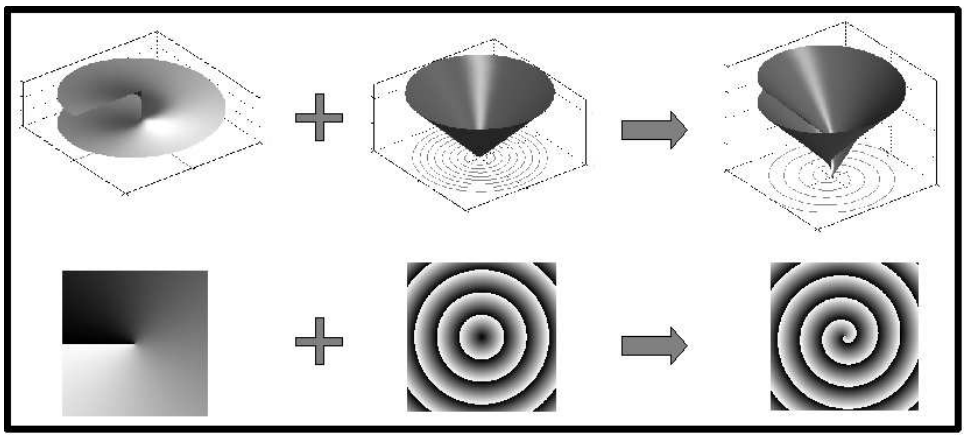

Figure 3.2: Phase masks - contour plots of the transmission function (3.8) (bottom row) and the corresponding surfaces of the constant phase (top row) of a first order Bessel beam. The total phase (right bottom) is a sum of the angular term $n\phi$ (left bottom) and the radial term $-k_r r$ (middle bottom).

A more versatile method to generate the phase mask involves application of a spatial light modulator (SLM), which allows dynamical adjustment of both n and k_r by a computer-generated hologram. An example of a 2-dimensional representation of the dielectric disk would be a contour graph shown in Fig. 3.2 (bottom row) for a first order Bessel beam. The gray scale of the graph varies from white to black, which corresponds to a phase change of the wave field from 0 to 2π. Now, instead of using a dielectric disk of a variable thickness, we employ a thin phase mask which shifts the phase of the light field at each point of the (r, ϕ) plane of the mask according to $(-k_r r + n\phi)$ for a given k_r and n. The left mask in Fig. 3.2 corresponds to the angular increment of the phase $n\phi$, the middle - to the radial $-k_r r$, and the right is the sum of the two. The resulting surfaces of constant phase of the diffracted light fields are shown in the top row. Practically, the phase mask is discrete and has a finite resolution; therefore, one can only adjust the phase of the light at each pixel of the mask, and the part of the incoming light field within that pixel area would be phase-shifted by the same value. The value of the shift is also discrete and can be changed from 0 to 2π in discrete steps determined by

a dynamic range of the mask. Thus, the higher the resolution and the dynamic range of the generated mask the better it represents the continuous transmission function (3.8). The phase mask can be realized as a liquid crystal matrix (the active element of the SLM), a 2-dimensional array of polar molecules transparent to the incoming light. The orientation of the molecules of each pixel, and thus the local index of refraction responsible for the phase shift, can be controlled by an external electric field through an applied voltage. The voltage is computer-generated for each element of the liquid crystal matrix (pixel of the SLM) in accordance with the required transmission function (3.8).

In our experiments we used a Spatial Light Modulator produced by the Hamamatsu Corp. A grey-scale contour plot similar to that in Fig. 3.2 was computer generated for a given order of the Bessel beam n and a specific diameter of the first ring set by k_r. The plot's 8-bit image as an array of voltages was sent through a video-graphic array (VGA) port of the computer to the SLM, thus controlling the phase shift at each element of the liquid crystal matrix with a 256-level depth. The physical size of the pixel was set by the active square cross-section area of the modulator of 2.5cm $\times$ 2.5cm and the resolution of 768 $\times$ 768 pixels. Technically, the control voltage for each pixel is created in the following way. The voltage from the computer sets the power of the SLM's internal laser. The internal laser beam propagates onto an array of photoelectrodes, which place voltages across a liquid crystal matrix. As the voltage is applied across the crystal, the polar molecules re-orient themselves. When a molecule in the liquid crystal re-orients, the index of refraction changes in that region of the crystal, thus retarding the phase of the corresponding portion of the external light field [59]. More details on the internal structure and the functionality of a particular model of the SLM used in our experiments can be found in reference [60].

The optical setup to create the Bessel beams used in our experiments is presented in Fig. 3.3. A Coherent 899 Ti:Sapphire laser pumped by a Coherent Innova 400 Ar^+ laser generated a Gaussian laser beam at 780 nm with the output power

of 500 mW. A small portion of the light was reflected from the main beam and coupled with a saturated absorption setup (SAS) to calibrate the laser frequency. The main beam was horizontally polarized by a half-wave plate, expanded by a telescope consisting of two spherical lenses L1 and L2 to cover the active area of the SLM. As our SLM was reflective, we used long optical paths of several meters between mirrors M1, M2 and the SLM to reduce the angle between beams incident to and diffracted from the SLM. The computer-generated phase mask corresponding to the transmission function (3.8) assumes normal incidence. The small deviation from the normal incidence gives rise to a slight ellipticity of the Bessel rings that can be compensated by changing the aspect ratio of the computer-generated hologram. Also, note that the incident light has to be linearly polarized along the orientation axis of the liquid crystal molecules at zero external voltage. This was achieved by a half-wave retardation plate that set the linear polarization of the Ti:Sapph beam to provide the maximum conversion efficiency from the Gaussian to Bessel transverse optical modes. As an example, a photograph of a transverse intensity profile of the $4th$-order Bessel beam is shown in Fig. 3.4.

We have done an extensive investigation of the transverse profiles of Bessel beams of various orders n and transverse spatial frequencies k_r generated for different resolutions and dynamic ranges of the SLM to find the best combination suitable for guiding cold atoms inside the first ring of the hollow beam. In particular, we tracked three main parameters important for the guiding: the transverse intensity profile, the maximum propagation-invariant distance and the optical mode conversion efficiency. The transverse profile determines the repulsive optical potential for the atoms and its quality is important for atom confinement. It is essential to minimize the amount of leakage light inside the dark core of the beam to reduce the photon scattering rate, to ensure the homogeneity of the light intensity distribution in the first ring as a function of the polar angle, and to create a large radial intensity gradient that provides a higher repulsive force. The larger intensity gradient corresponds to a smaller width of the first Bessel ring at the same optical

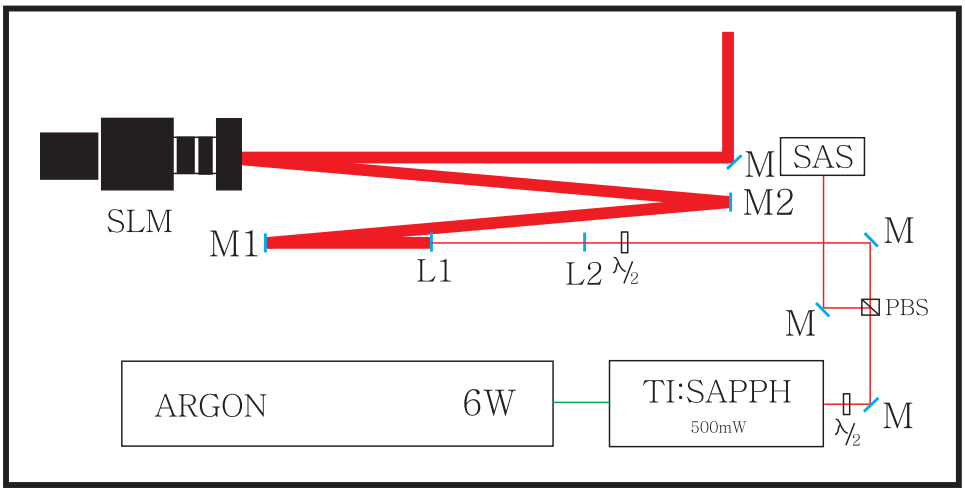

Figure 3.3: Optical layout of the Bessel beam generation setup. The Gaussian output of a Ti:Sapphire laser is expanded by spherical lenses L1 and L2, polarized by a half-waveplate ($\lambda/2$) and diffracted from the surface of the SLM to form a Bessel beam. A part of the Gaussian beam is split by a polarizing beam splitter (PBS) and sent to a saturated absorption spectroscopy setup (SAS) to monitor its detuning. The Ti:Sapphire laser is pumped by a 6 W argon laser. M, M1 and M2 are dielectric mirrors.

power, and can be increased with the order of the Bessel beam. For example, an $n = 20$ beam provides a much more attractive confining potential than one of $n = 4$, but has a much larger radius of the first ring for a fixed spatial frequency k_r. The ring's radius can be reduced with k_r, but at some point the beam quality becomes limited by the resolution of the SLM, and we could only use Bessel beams of low order guides for small atomic clouds. The propagation-invariant distance sets the quality of the Bessel beam as an atom guide of a constant cross-section. This distance is set by the size of the experimental vacuum chamber or the desired distance over which the atoms have to be transported. For our experimental setup we required an invariant-propagation distance of 25 cm, while invariant-propagation distances of over a meter were demonstrated for the applied Bessel beams. Finally, we also tried to optimize the SLM efficiency to convert the power of the Gaussian

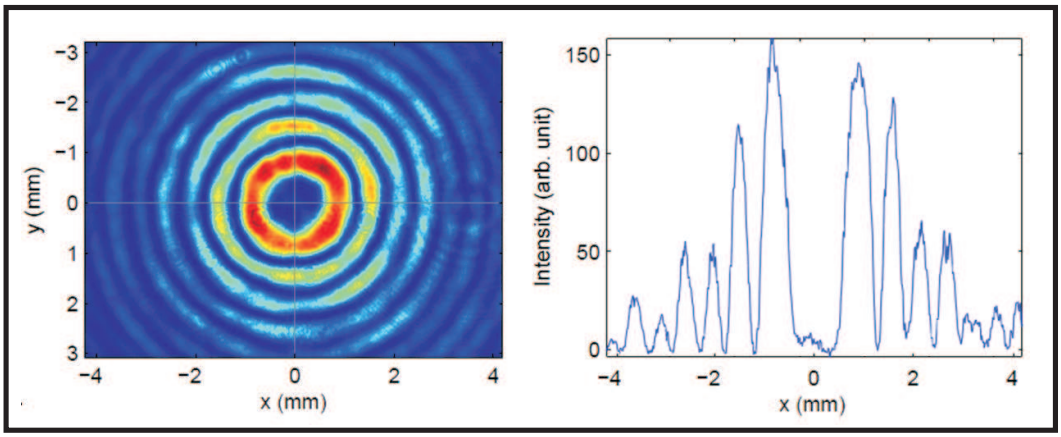

Figure 3.4: A photograph of transverse intensity profile of $4th$-order Bessel beam (left) and a one-dimensional slice of the beam's intensity distribution along radial direction (right).

optical mode into the Bessel's first ring, as the higher total power in the first ring of the hollow beam increases the height of the repulsive optical potential seen by the atoms. The most interesting results on the properties of the hollow Bessel beams generated by an SLM were reported in reference [50]; more technical details and numerical simulations can be found in Ref. [60].

After investigation of the transverse profiles of various Bessel beams and their ability to confine atoms within the first ring of the beam, we have found that the most suitable candidate for a parallel atomic guide would be a $4th$-order Bessel beam with the transverse spatial frequency $k_r = 10635m^{-1}$. The corresponding transverse intensity profile is presented in Fig. 3.4; it is characterized by the radius of the first ring (position of the first maximum of the Bessel function) of 0.5 mm and the total width of the first ring of 0.7 mm. The invariant-propagation distance of the tunnel was over 1 m. We found that the SLM conversion efficiency under those conditions was about 20 %, when 500 mW of the Gaussian laser beam were converted by the SLM into 100 mW of power in the first ring of the Bessel beam. Various devices based on the generated Bessel beam were demonstrated and are described in Chapter 4.

Chapter 4

Tunnel Lock

As discussed in Chapter 2, optical dipole potentials are useful for such applications as atom interferometry, lithography, quantum information and biological physics. Repulsive blue-detuned optical potentials are especially promising for trapping particles in the null intensity on-axis regions, where light scattering is greatly reduced. A high-order Bessel mode, non-diffracting solution of the wave equation with the transverse profile given by a Bessel function, is ideal as an atomic guide of a constant cross-section to transport cold atoms over large distances. The generation of the Bessel beams suitable for atom optics was discussed in Chapter 3. In Chapter 4 we will show how one can apply a Bessel beam as a building block to create several elements from the atom optics toolbox: a single Bessel beam can be used as a guide to transport atom; a *tunnel lock*, proper combination of two beams allows us to switch the direction of an atomic beam, to split an atomic density between two beams, and delay the propagation of the atomic beam.

4.1 Single Tunnel

We first consider an application of a single blue-detuned Bessel beam for guiding laser-cooled rubidium atoms. As described in Chapter 3, we chose a $4th$-order Bessel beam with the transverse spatial frequency $k_r = 10635m^{-1}$. The beam had 100 mW of power in the first ring of 1 mm in diameter that set the ring intensity, and therefore the dipole optical potential, at a fixed detuning. As discussed in

Chapter 2 (Sec. 2.2), the height of the dipole optical potential is inversely proportional to detuning from an atomic resonance at high values of the detuning and moderate laser intensities. Lower detunings provide higher optical potentials for the atoms, but increase the photon scattering rate, which results in heating and acceleration of the cold atomic sample. For example, the detuning by + 4 GHz[1] from the $5s_{1/2} \rightarrow 5p_{3/2}$ transition in rubidium provides the maximum value of the optical potential of 300 μK for the Bessel beam of our choice, high enough to confine atoms laser-cooled and confined by a magneto-optical trap (MOT). The corresponding heating rate due to the absorption is less than 1 μK per millisecond. The height of the optical potential and the photon scattering rate are calculated in Appendix A.

We used a standard magneto-optical trap as a source of cold atoms. The principle of the MOT operation is discussed in Appendix A, while the particular design of our experimental apparatus for laser cooling is presented in full detail in Appendix C. Here we only mention the MOT parameters relevant to the guiding experiments. Our demonstrations of all Bessel beam applications were performed with a 1 mm diameter Rb cloud collected from a vapor of 10^{-8} torr into a MOT held at 250 μK. A Bessel beam tunnel of 1 mm in diameter was blue-detuned 4 GHz from $5s_{1/2}|\, F = 2\,\rangle \rightarrow 5p_{3/2}|\, F' = 3\,\rangle$ rubidium cycling transition. Due to the absorption of light, the atoms can decay to the lower hyperfine ground state level $5s_{1/2}|\, F = 1\,\rangle$, which is - 6.8 GHz from the cycling transition. For those atoms, the tunnel is red-detuned, and the corresponding optical potential attract atoms to the high-intensity walls of the tunnel, where they can be heated and pumped back to the cycling transition.

The propagation direction of the Bessel beam was close to vertical, 6° from vertical. The guide was aligned with the trapped MOT cloud by maximizing the number of atoms inside the dark core of the hollow beam. To load the tunnel,

[1]The '+'-sign indicates that the laser frequency is blue-detuned from the atomic resonance.

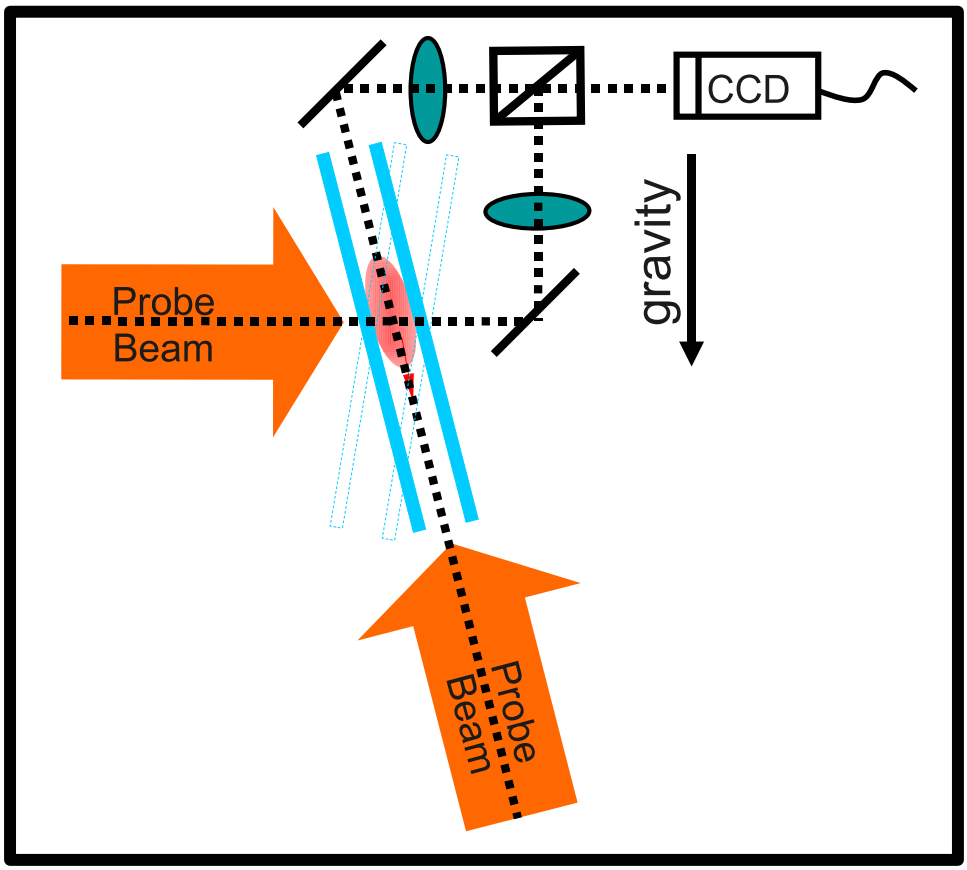

Figure 4.1: Two probe beams were used to capture the cloud dynamics along and transverse to the tunnel.

MOT laser beams were blocked by a mechanical shutter and the Bessel beam was turned on. This event set time $t = 0$ for the evolution of the atomic density in the presence of the Bessel beam. The atomic density distribution was monitored by an absorption imaging technique with two probe laser beams, one along and the other one across the tunnel. The schematic of the imaging system is presented in Fig. 4.1. To improve the signal-to-noise ratio we took a background image with no atoms in the field of view and subtracted it from the image with the cloud. The experimental sequence, MOT loading, propagation in the tunnel for a fixed time t, and cloud imaging were repeated many times. The resulting column density distributions averaged for 40 individual photoshots at each evolution time

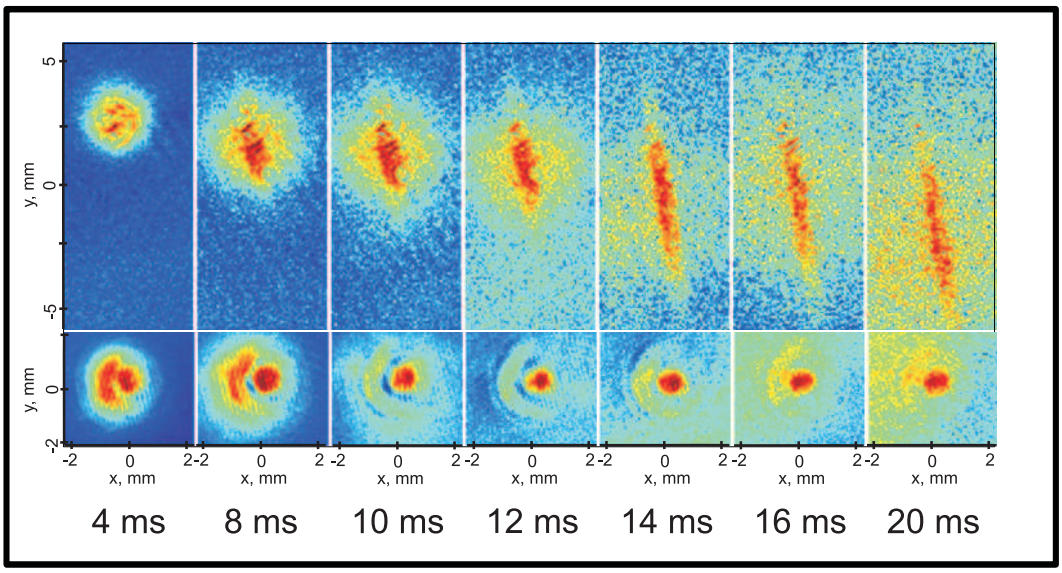

Figure 4.2: Dynamics of a cold rubidium cloud in the presence of a single tunnel. The top row of images shows propagation along the tunnel; bottom row confirms the confinement in the transverse direction.

are presented in Fig. 4.2.

The images in the top row were taken across the tunnel: the initial round cloud at t = 0 starts falling in the gravitational field, expands according to its thermal energy, while experiencing the dipole force from the optical potential of the Bessel beam. The atoms inside the tunnel move freely along the tunnel while confined by the tunnel walls in the transverse direction, when their corresponding kinetic energy at the wall was less then the height of the optical potential. The rest of the atoms, up to 40 % of the initial number of atoms in the MOT, too energetic to be trapped by the tunnel walls, leave the first ring of the Bessel beam and are not taken into account when investigating the properties of the atomic guide. At t = 14 ms there is a noticeable separation between atoms trapped inside and those outside the tunnel, and the atomic cloud takes the shape of the tunnel. This separation is more pronounced when the transverse density profile is monitored along the tunnel (the probe beam for absorption imaging and the Bessel beam were aligned) as seen

on the bottom row of images in Fig. 4.2. At t = 8 ms the separation between the trapped atoms and those outside of the tunnel is quite clear. Also note, the cloud's optical density, when imaged along the tunnel, is much higher than when imaged across the tunnel, which provides a high signal-to-noise ratio even at longer times. We calculated the relative number of atoms trapped in the tunnel at a given time as a column density integrated along the direction of the probe beam. The absolute number of atoms was deduced by calibrating the relative number of atoms in the freely expanding MOT cloud as described in Appendix A.

We have tracked the atomic cloud confined in the transverse plane of the Bessel beam and free-falling along the beam for up to 70 ms. The time of the experiment and the propagation distance were limited by the collisions with the room-temperature background gas due to a relatively high rubidium vapor pressure in the experimental chamber. We estimated the total single tunnel loss rate due to the background gas collisions together with the leak of hot atoms through the tunnel from a series of images similar to those in Fig. 4.5 (bottom row). The number of atoms in the tunnel as a function of time is plotted in Fig. 4.3 (top), along with an exponential fit of the data taken between 6 and 70 ms, and normalized residuals from the fit (bottom). In a simplified model, the total decay rate is determined by the background collisions and the leakage through the tunnel walls, as discussed in Ref. [60]. Here we treat the decay as a single exponential, $y = Ae^{x/\tau} + y_0$, to use the resulted decay time in calculations of the switch efficiency. From the fit, we found the $1/e$-decay time $\tau = (15.9 \pm 1.41)$ ms and the reduced chi-square $\chi^2_{red} = 4.71$.

As atoms propagate along the tunnel, they scatter photons and are accelerated. Depending on the detuning, atoms with high kinetic energy are not trapped by the tunnel, resulting in a cut-off of the high-energy tail of the Maxwellian velocity distribution of the remaining cloud in the transverse plane. At small detunings the dipole potential is high, but so is the scattering rate. Due to light absorption, the atoms are heated and accelerated along the tunnel, their kinetic energy exceeding

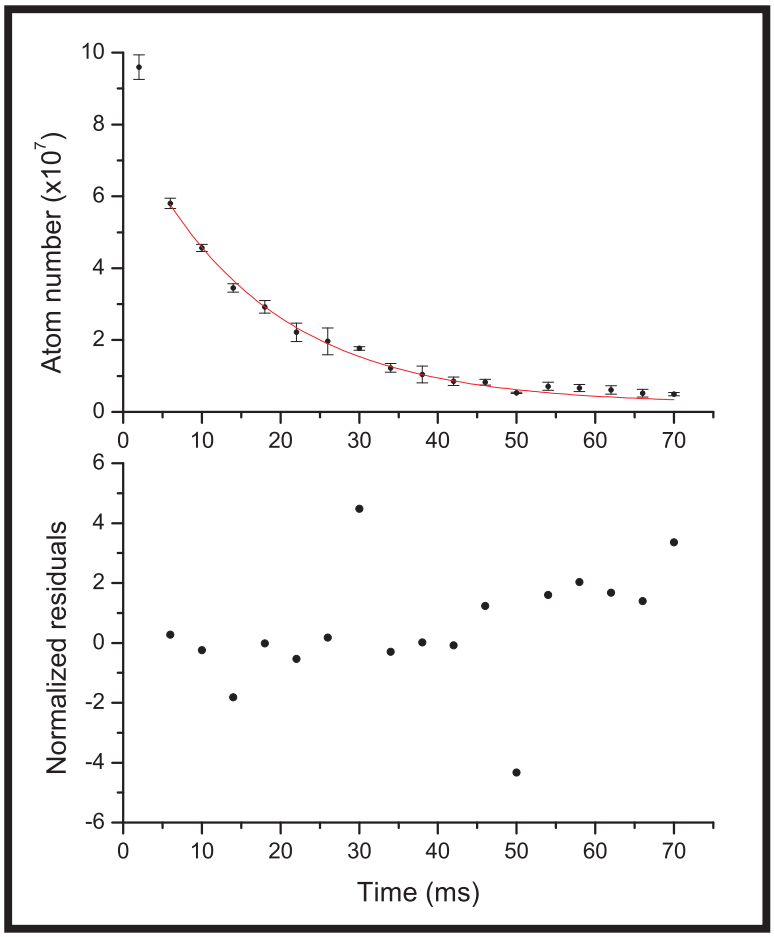

Figure 4.3: The number of atoms confined in a single tunnel is shown as a function of time along with an exponential fit at the detuning of + 4 GHz (top), and normalized residuals resulted from the fit (bottom). The error bars represent the standard deviation in the mean of forty runs. The exponential fit yields the $1/e$-decay time $\tau = (15.9 \pm 1.41)$ ms and the reduced chi-square $\chi^2_{red} = 4.71$.

the height of the tunnel potential. At larger detunings, the scattering rate, δ, and therefore heating of the atoms, drops faster ($\sim 1/\delta^2$) than the height of the dipole potential ($\sim 1/\delta$), and atoms can be confined in the tunnel for longer times. To find the optimum detuning, we compared the number of atoms left in the tunnel at t = 16 ms for various detunings. The choice of time was determined by the duration of the switch experiment. We found, that the number of confined

atoms reached its maximum value at the detuning of about + 4 GHz. At higher detunings, atoms gain less thermal energy from the absorption, but the reduced height of the trapping potential results in the leakage loss. In this case, the atom number in the tunnel will drop faster than at short times as the most energetic atoms will leave the tunnel in several milliseconds. The number of atoms left in the tunnel will decay due to collisions with the background gas similar to the tail of Fig. 4.3. As the number of trapped atoms dropped with the detuning, we observed the number to be about 10% of its maximum value at a detuning of + 5 GHz. However, further detuning gave rise to an increase of the atom number to about 30% of the maximum value at a detuning of + 6 GHz, and the number gradually fell for higher δ. This local maximum as a function of the detuning is thought to be due to the internal level structure of rubidium-87[2]. As discussed before, atoms can decay into $5s_{1/2}|\, F = 1\,\rangle$ ground state. The closer the detuning of the Bessel beam to the hyperfine splitting of the ground state, the more the tunnel pumps the population back to the $5s_{1/2}|\, F = 2\,\rangle$ state, acting similar to the repump beam of a standard MOT setup. Thus, we attribute the increase of the number of trapped atoms to the repumping effect of the Bessel beam at the detuning of + 6 GHz. The most effective repumping occurs on resonance, when the detuning is equal to + 6.8 GHz, the hyperfine splitting of the ground state. However, as the detuning is increased from 6 to 6.8 GHz, the tunnel starts acting as a red-detuned optical potential for the atoms in $|\, F = 1\,\rangle$ state, and those atoms will be attracted to the tunnel walls by the potential. For the case of a multi-level atom, Eq. 2.2, valid for the two-level atom, has to be generalized as the dipole potential depends on the particular sub-state of the atom [61]. In some situations, the complex internal structure can be used to our advantage, for instance, in the splitting experiment with ^{85}Rb as described at the end of this Chapter.

An extensive experimental investigation of dynamics of atoms trapped in the

[2]Rubidium level structure is discussed in Appendix C.

Bessel beam, theoretical analysis and numerical simulations are discussed in details in reference [60].

4.2 Atomic Beam Switch

After characterizing the properties of the Bessel beam as an atomic guide, we may apply it to demonstrate more complicated devices. For interferometry-type structures or Quantum Information applications, an atomic beam may need to be switched from one direction to another, an atomic density split into separate atomic beams, or the propagation of an atomic cloud delayed. All three scenarios can be realized by a *tunnel lock*, consisting of two properly gated hollow Bessel beams. Consider two crossed, near-vertical atomic guides as shown in Fig. 4.4. Let the atoms start propagating along tunnel A. If both tunnels are on (solid red, middle cross in Fig 4.4) the atoms can not penetrate the intersection region of the two Bessels beams[3]. If the intensity of the second tunnel B is lowered (entrance gate open; left cross in Fig 4.4) the atoms propagate into the intersection region to be positioned in both tunnels simultaneously. When the intensity of the second tunnel is raised (entrance gate closed; middle cross in Fig 4.4), the cloud will be trapped in three dimensions, and its propagation delayed. If the intensity of the second tunnel is reduced (left cross in Fig 4.4), the atoms will follow the original propagation direction after some delay thus realizing a delay line. If instead the intensity of the first tunnel is reduced (exit gate opened; right cross in Fig 4.4), the cloud will propagate along tunnel B, a different direction with respect to the original propagation, thus realizing an atomic beam switch.

The prototype tunnel lock was used to divide and switch the direction of a moving ensemble of cold atoms. We demonstrated the switch by launching a portion of a MOT cloud into a tunnel and then deviating the direction of the

[3]We assume that the optical potential due to the Bessel beam is much higher than the kinetic energy of the atoms.

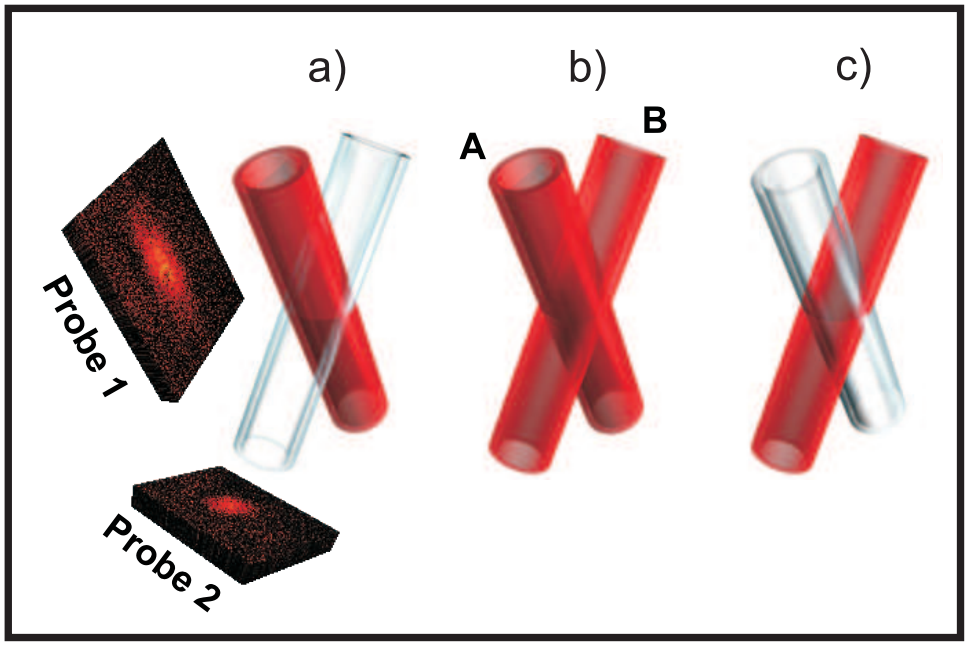

Figure 4.4: Schematic of the tunnel lock, formed by crossing two tunnels, and cloud images taken along and across the tunnels. Red (clear) cylinders indicate tunnels being on (off). From left to right: a) only tunnel A is on (atoms enter overlap volume), b) both tunnels are on (atoms trapped in the intersection volume), c) only tunnel B is on (atoms leave overlap volume). Appropriate switching of the tunnels generates a beam switch, a splitter and/or a delay line.

moving cloud with another tunnel. The tunnels were created by splitting the Bessel beam diffracted from the SLM into two beams with an optical beam splitting cube. Both tunnels were aligned with the MOT cloud and crossed at an angle of 12° . Both beams were nearly in the vertical direction as shown in Fig. 4.4. In order to distinguish cloud propagation in tunnel A from that in tunnel B, we monitored the atom distribution in each hollow beam in the vertical direction using only one probe beam directed along tunnel B. The corresponding shadow images are presented in Fig. 4.5 for the cloud trapped in tunnel A (top row) and tunnel B (bottom row) at various time. For example, as atoms move in tunnel B, the cloud elongates along the tunnel and projects an image that is circular with a constant

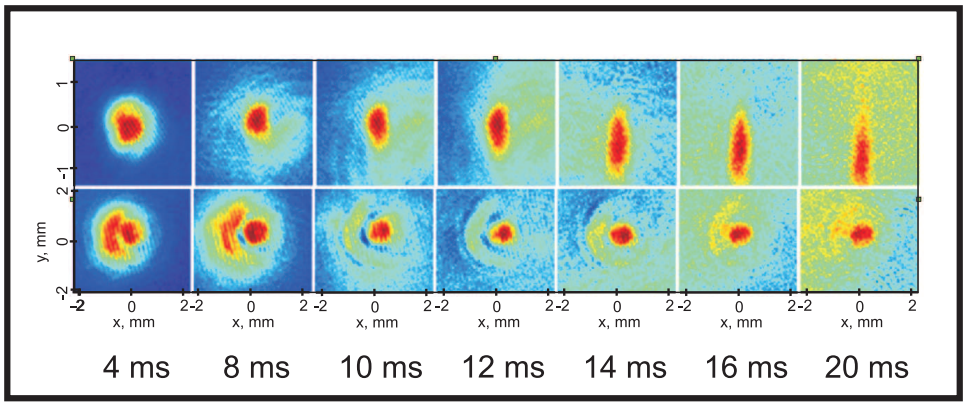

Figure 4.5: Cloud evolution in a single tunnel as imaged by a probe beam directed along tunnel B. Top row of images show the propagation in tunnel A, bottom row - in tunnel B. The bottom row of images is the same as in Fig. 4.2. The shape change from a stubby oval to a circle at longer times allows to distinguish the propagation in tunnel A from that in tunnel B.

diameter at all times (Fig. 4.5, top row). By contrast, the atoms in tunnel B propagate at a 12 ˚angle with respect to the probe beam direction, and as the cloud spreads, its projection changes from near circular to that of a stubby oval. The longer the evolution time the larger the cloud aspect ratio is as seen in the top row of images in Fig. 4.5. Therefore a switch of the atomic beam direction from tunnel A to tunnel B results in a change of the cloud's shape from an oval to a circle as in our imaging system.

Now we are set to describe the demonstration of the atomic beam switch when both tunnels were used in the same experiment. We changed the direction of the atomic beam with the following lock operations. At t = 0, the atomic cloud was launched in tunnel A with the entrance gate open (tunnel A on and tunnel B off). At t = 8 ms, the entrance gate was closed (tunnel B on) and the exit gate was opened (tunnel A off) simultaneously with two synchronized mechanical shutters. The speed of the shutters determined the gate switch time of 1.6 ms. As with single tunnel experiments, the cloud propagation was monitored by two probe beams, one

along the axis of tunnel B, and the other perpendicular to the geometrical plane defined by the axes of the two tunnels. The shadow images of the corresponding density distributions are presented in Fig. 4.6 for the probe directed across the plane of the two tunnels (top row) and the probe along the tunnel B (bottom row).

First, let us consider the top row of images. We see that 4 ms after the switch was activated (the 12 ms panel), the cloud is no longer aligned with tunnel A (tunnel A off and tunnel B already fully on at this point). It takes several milliseconds for the majority of atoms to encounter the walls of tunnel B and to start propagating along the tunnel. At this stage a significant part of the cloud is confined by tunnel B; the remaining images show the trapped cloud aligning itself with tunnel B and propagating along it. The re-direction of the cloud can be monitored as well from the other probe beam, aligned with the axis of tunnel B, and is presented in the lower row in Fig. 4.6. By 8 ms, the cloud starts taking an oval shape and would continue stretching similar to the top row of Fig. 4.5 if it were to propagate in tunnel A alone. Instead, after the switch from tunnel A to tunnel B is activated, we observe the distinct shape change from a stubby oval in the top row of Fig. 4.5 to a circle in the bottom row of Fig. 4.5 at $t > 8$ ms indicating the atomic beam switch from tunnel A to tunnel B.

To characterize the switch we measured its efficiency and the heating effects due to the abrupt change of the optical potential and the re-direction of the cloud. We define the switching efficiency as the ratio of the number of atoms in tunnel A before the switch (at t = 8 ms) to the number in tunnel B after the switch (t = 10 ms). The number of atoms before the switch can be determined directly from the absorption image at 8 ms (Fig. 4.5, bottom row). During the switch, a significant fraction of the atoms was outside of the intersection volume of the two tunnels and could not be re-trapped by tunnel B while still contributing to the shadow images right after the switch. Therefore the images corresponding to 10 and 12 ms were not used to determine the efficiency. Instead we measured the number of atoms

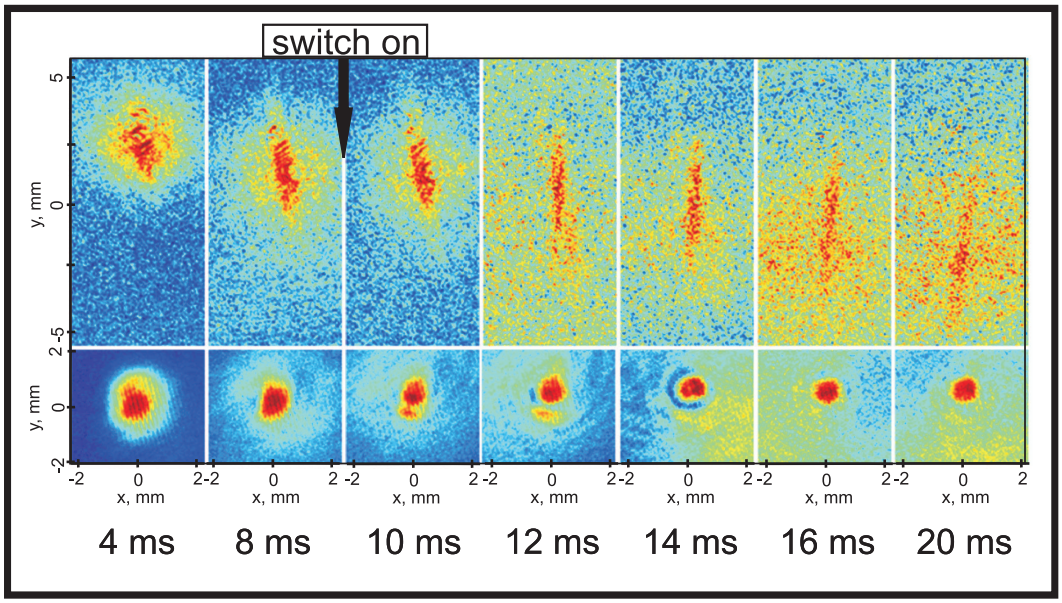

Figure 4.6: Shadow images of rubidium atoms passing through the tunnel lock. Top row shows the cloud initially moving downward and to the right in tunnel A and switching direction to propagate downward and to the left along tunnel B as observed by probe 1 (refer to Fig. 4.4). Bottom row of images shows the same switching as detected by probe 2. The cloud, starting in tunnel A, should stretch according to the top sequence of images in Fig. 4.5. After the switch was activated, the cloud takes and preserves a round shape similar to the bottom row of images in Fig. 4.5, an indication of propagation in tunnel B consistent with switching from one tunnel to another. The black arrow indicates the moment of switching.

at $t > 14$ ms, long enough after switching for the non-trapped atoms to leave the imaged volume. We used the single tunnel loss rate (Fig. 4.3) to extrapolate back to the number of atoms at t = 10 ms. We found the switching efficiency to be about $(33 \pm 5)\%$. The resulting efficiency was mainly limited by a relatively large size of the atomic cloud compared to the intersection volume of the two tunnels. The efficiency can be increased by using smaller and colder clouds, and switching of the whole cloud should be possible.

We investigated switch-induced heating and acceleration by measuring the tem-

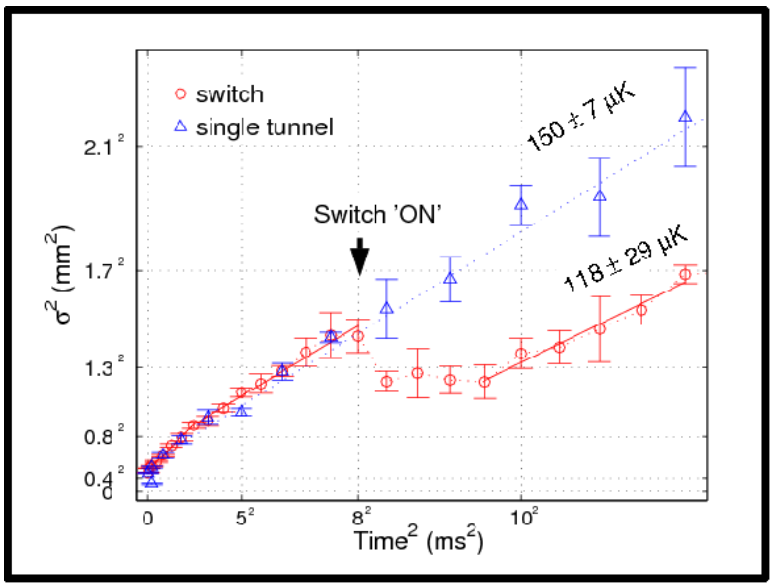

Figure 4.7: Cloud evolution in a single tunnel and through the switch where t is the time after the cloud is released from the trap and σ is the width of a Gaussian fit of the cloud density along either tunnel. The error bars represent the standard deviation of the mean of five runs.

perature and kinetic energy of the cloud before and after the switch in the longitudinal direction. There was no measurable enhancement to the center of mass acceleration over acceleration due to gravity after the switch was activated. Since the cloud's motion was not constrained along the tunnel, it preserved its original near-Gaussian density distribution expanded freely in 1-D according to $\sigma^2 = \sigma_0^2 + v^2t^2$, where σ^2 is the initial width of the cloud, and v^2 is the mean square velocity of the Maxwellian distribution. The sizes of the cloud propagating in a single tunnel and switching from one tunnel to another are presented in Fig. 4.7.

The slope of a curve in Fig. 4.7 is v^2 and proportional to the temperature. For the case of a single tunnel (blue triangles in Fig. 4.7), the slope decreases between 0 and 5 ms and after that becomes constant corresponding to the temperature of $(150\pm7)\ \mu K$. The confined cloud is colder than the source atoms. The temperature reduction may be attributed to the inability of the tunnel to confine the hottest

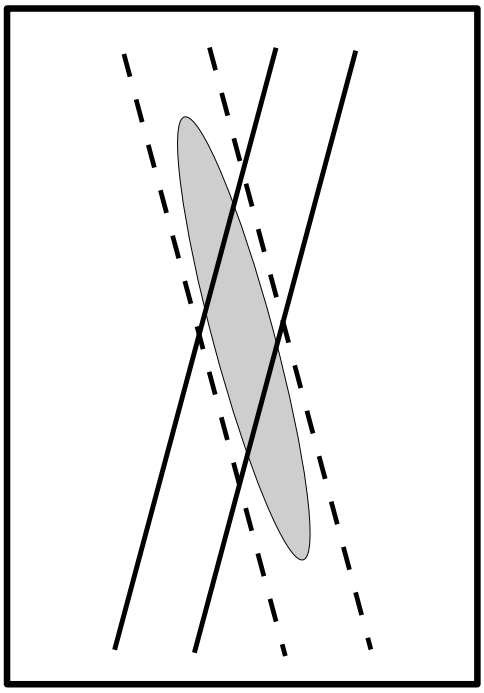

Figure 4.8: Schematics of the cloud re-direction upon the switch of tunnel B. The wings of the cloud, spread after thermal expansion along tunnel A, are outside the intersection volume of the two tunnel, and cannot be re-trapped.

atoms since the initial cloud temperature is comparable with the optical potential of the tunnel. In the switch experiments (red circles in Fig. 4.7), the evolution of the cloud is identical to that of a single tunnel up to 8 ms when the switch is activated. Shortly after the switch is activated, the length of the cloud is reduced by about 25% as the intersection of the two tunnels is smaller than the size of the cloud, and the ends of the expanded cloud are not re-trapped by the second tunnel. It is clear that between 8 and 10 ms the evolution of the imaged atomic density does not correspond the Maxwellian velocity distribution of the cloud; σ is nearly constant while the cloud re-adjusts. After 10 ms, when the near-Gaussian distribution is re-established, σ^2 becomes linear with t^2, giving a temperature of about 118 μK.

The measured reduction of the cloud temperature reflects the fact that hot

atoms occupied the ends of the cloud that were truncated by the switch as illustrated in Fig. 4.8. The atoms were originally confined in tunnel A, with their transverse kinetic energy smaller than the height of the corresponding optical potential. The cloud's transverse size across the tunnel was set by the 1 mm diameter of the tunnel, while the length along the tunnel, resulting from the free expansion of the cloud, was $\sim$ 4 mm. When the second tunnel, B, was turned on, only a fraction of the cloud was inside the intersection volume of the two tunnels, giving by $V = \frac{16}{3} r^3 / sin\phi$ for the perfect overlap, where r is the radius of a tunnel, and ϕ is the angle between the two tunnels. The atoms outside the intersection volume were lost for the second tunnel. Atoms at the edge of the cloud were the hottest as they moved furthest from the center of the cloud. In addition, some of the atoms had kinetic energy along tunnel A higher than the confining optical potential. When tunnel B was turned on at an angle with respect to tunnel A, those atoms were not re-directed by the barrier of tunnel B, but penetrated the walls of tunnel B, thus contributing to cooling the rest of the cloud. In the real experiment, the tunnel cross was not perfectly overlapped with the central portion of the cloud, and some of the colder atoms closer to the center were also ejected upon switch activation. We studied the temperature change numerically by truncating all but the central spatial part of the cloud, such that only 30% of atoms were left in the tunnel after the truncation. We assumed a Gaussian density and Maxwellian velocity distributions of the cloud and the cloud temperature of 150 μK before the switch. Keeping the central portion led to a 60-μK cloud after re-thermalization without taking into account the change of the cloud propagation direction by a small angle of 12°. To verify the validity of this approach, we eliminated the central portion of the cloud containing 70% of the atoms. The resulted re-thermalization gave rise to a 1500-μK cloud. This simple consideration is consistent with our observation that we truncated both hot and cold atoms in our experiment, but mostly hot. More importantly, our results suggest no measurable heating of the cloud upon switch activation due to absorption from the tunnels. Although our simulations

were overly simplified, not accounting for the full 3D behavior, they did identify an important contribution to cooling after the switch. Furthermore, they revealed the importance of the overlap geometry, something that will have to be addressed by any beam-splitter design based on hollow tunnels.

4.3 Splitter and Delay Line

We can extend the application of the prototype lock device to an atomic splitter and delay line by crossing the two tunnels at the MOT cloud maximizing the initial number of atoms in the tunnel overlap volume. In this configuration, both Bessel beams were on simultaneously after the MOT was switched off. The evolution of the atoms along the plane of the two tunnels is presented in Fig. 4.9. Consider three right frames, which show the evolution of three distinct clouds with different momenta. Atoms with transverse and longitudinal velocities below 15 cm/s (250 μK) form the delayed cloud trapped in the intersection volume of the two tunnels. The traveling clouds have higher longitudinal velocities and propagate along each tunnel thus forming two atomic beams split from the main cloud. Before the tunnel was loaded, the MOT atoms were in the upper hyperfine level of the ground state ($5s_{1/2}|\, F = 2\,\rangle$). The tunnel loss via the lower hyperfine level($5s_{1/2}|\, F = 1\,\rangle$), and thus the image contrast (the number of trapped atoms), is sensitive to detuning. For ^{87}Rb, the best image contrast (4.9, two left frames) was obtained at a detuning of + 6 GHz relative to the $F = 2 \rightarrow F' = 3$ transition (refer in Appendix C). This detuning places the laser light frequency 0.2 - 0.4 GHz red of the $F = 1 \rightarrow F' = 0, 1, 2$ transitions. Therefore the Bessel beam turns out to be blue-detuned with respect to some near-resonant atomic transitions and red-detuned with respect to the others: atoms in the $5s_{1/2}|\, F = 2\,\rangle$ are repelled by the tunnel walls but those in the $5s_{1/2}|\, F = 1\,\rangle$ are drawn in by the tunnel walls and get accelerated by a high photon scattering rate. In addition, a significant fraction of these atoms will be lost because, when they are pumped back to the upper

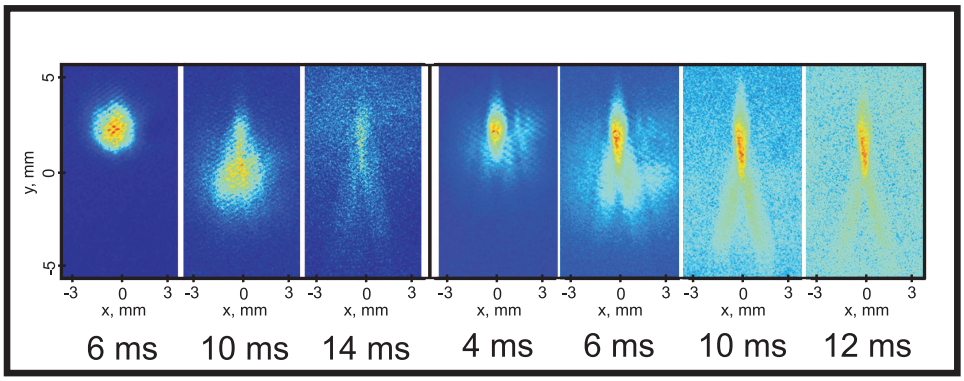

Figure 4.9: Splitter/delay line realized with the tunnel lock. Tunnels A and B are on simultaneously and crossed at the MOT location. The three(four) left (right) panels correspond to ^{87}Rb (^{85}Rb) with a tunnel detuning of +6 GHz (+3 GHz). Three momenta are generated corresponding to clouds moving downward to th left and to the right, or trapped in the overlap volume of the two tunnels.

hyperfine level, they can be expelled from the walls both back into and out of the tunnel. Smaller detunings increase the scattering rate as well as the decay rate into the $5s_{1/2}|\, F = 1\,\rangle$ state thus reducing the image contrast. We can eliminate the lower hyperfine leak by tuning the tunnel to the blue of the re-pump frequency as well. However, above + 6.6 GHz detuning, we could only generate a potential of $\sim 150\ \mu K$ or lower as the Bessel beam power was limited by the damage threshold of the SLM. Such an optical potential is too low to contain most of the atoms. Instead of increasing the detuning, we achieved better performance by using ^{85}Rb isotope at the detuning of + 3 GHz, which is blue of both sets of resonances (three right frames on Fig. 4.9). We have not performed any quantitative measurement to characterize the properties of the splitter and the delay line, as the main goal of this demonstration was to show the versatility of the tunnel lock for various applications.

4.4 Conclusion and Future Directions

This part of the dissertation was devoted to development of new tools for atom optics, a beam switch, a splitter, and a delay line that can find applications in atom interferometry, quantum information, lithography, and biological physics. We have successfully employed a blue-detuned $4th$-order Bessel beam as an atomic guide to transport laser-cooled rubidium atoms. We found the application of the Bessel beams to be quite versatile: the tunnel lock, two properly gated crossed Bessel tunnels, was demonstrated to transport and split an atomic cloud, delay its propagation, and switch the direction of an atomic beam from one tunnel to another. The ensemble's life time in the tunnel was limited by the collisions with the hot background gas, and the switching efficiency by the relative sizes of the cloud and the tunnel. The properties of the demonstrated tunnel lock are comparable with those achieved by other methods such as guiding and splitting along a magnetic wire, and all-optical red-detuned schemes.

Some of the applications of the demonstrated devices require decoherence-free evolution that remains to be properly shown. Because decoherence is strongly influenced by the high scattering rate at small detunings, coherence issues will have to be studied with larger detunings, where spontaneous emission is suppressed. The act of altering the direction of the cloud does not lead to significant heating, it would be interesting to follow this approach to study colder samples for interferometry purposes. A reduction in the sample temperature to less than 1μK and large detunings would allow to virtually eliminate absorption. However, the employed 1-mm diameter hollow beam is a multi-mode tunnel for atoms [60] that can results in excitations of higher order modes, similar to the property of a multi-mode optical fiber. While condensates are often envisioned for interferometry, it was shown that high fringe visibility can be achieved with thermal clouds [62]. The higher repetition rate is one distinct advantage of thermal clouds over condensates. The tunnel locks demonstrated in our experiments can be applied to red-detuned

(filled) tunnels. Since increasing the intensity essentially deepens the potential well for red-detuned tunnels, it is not clear how to stop a traveling cloud with a diffractionless laser beam (i.e., J_0) that does not come to a focus without introducing additional beams. This is possible with blue-detuned tunnels because blue detuning raises the barrier. Nevertheless, intensity modulation should allow the branching between two red tunnels to be modified as well. At the same time, interferometer structures are easier to imagine with red-detuned beams. Consequently, for greater flexibility in free-space manipulation of neutral ensembles, elements based on both red and blue detuning will be required.

We should also point out several promising applications of an SLM to generation of arbitrary shaped blue-detuned optical potentials on a plane in real time [50]. They might be used as billiards to study the chaotic dynamics of confined atoms and as tweezers to manipulate macroscopic biological objects. As an example, it was theoretically shown [51] that the escape rate of a wavepacket from a chaotic billiard deviated from the classical value when the quantum mechanical nature of the interaction was taken into account. The classical regime was investigated using cold atoms in optical billiards [63, 64], while a proposed measurement of quantum corrections would help to understand the quantum mechanical behavior of the classically chaotic system.

Chapter 5

Quantum Information Science

5.1 Introduction

Quantum information science, a merging of quantum mechanics and classical information theory, opens new exciting possibilities in data computation, communication and storage. Over the last decades, the exponential shrinking of electronic components that process the information may be approaching its limit. The further minituarization of transistors on a near-atomic scales will leave no room for packing more components on a single chip. Quantum mechanics allows us to step beyond this limit, and in combination with information science, can provide a physical system to process information on the microscopic level. Such quantum systems can outperform some of their classical computational counterparts tremendously. Original ideas to exploit the computational power of quantum mechanics [2] and the development of quantum algorithms [3, 4, 5] promoted significant efforts toward the practical realization of a variety of physical systems applicable for quantum information.

Quantum bits, or qubits, are the states of a quantum mechanical system. If a classical bit, the carrier of classical information, can be in either one of two states, its quantum analog can also be in a superposition of the two states. The number of simultaneously accessible states scales as 2^N for N qubits, dramatically increasing the potential computational power of the quantum information processor.

Two quantum algorithms are known to outperform their classical counterparts:

the factoring algorithm, introduced by Shor, provides an exponential growth of computation speed compared to the classical algorithms [5]. Grover's search algorithm can find an element in an unsorted database with a quadratic increase of speed [4].

Quantum algorithms are constructed from smaller elements, that include a single qubit rotation between its two states and logical operations with qubits provided by quantum gates. Quantum gates are linear unitary operators acting on a state of the system. A set of properly combined gates that can provide any linear unitary operation, is called universal, such as the one consisting of a single-qubit Hadamard gate (H), a single-qubit $\pi/8$ gate (T) and a two-qubit controlled-NOT gate ($CNOT$) [65]. If $|\,0\,\rangle$ and $|\,1\,\rangle$ denote the two states of a single qubit, $|\,00\,\rangle$,$|\,01\,\rangle$,$|\,10\,\rangle$,$|\,11\,\rangle$ are the basis of the two-qubit system, then the universal set of gates can be written as

$$H = \frac{1}{\sqrt{2}} \begin{pmatrix} 1 & 1 \\ 1 & -1 \end{pmatrix}, \quad T = \begin{pmatrix} 1 & 0 \\ 0 & e^{i\pi/4} \end{pmatrix},$$

and

$$CNOT = \begin{pmatrix} 1 & 0 & 0 & 0 \\ 0 & 1 & 0 & 0 \\ 0 & 0 & 0 & 1 \\ 0 & 0 & 1 & 0 \end{pmatrix}. \tag{5.1}$$

Efforts to realize quantum computer hardware, a physical system that provides qubits and gates, are occurring in very different fields, such as NMR [6], linear optics [7], quantum dots [8], cold trapped ions [9] and neutral atoms [10]. Each approach has its advantages and drawbacks, and has to meet a set of minimum requirements, so-called DiVincenzo criteria [66]: the quantum computer must be a scalable physical system that can be initialized to a known quantum state; qubit coherence time must be much longer than the gate operation time; it must be possible to implement a universal set of gates within the system, and read out the

results of the computation.

One of the promising implementations of quantum computer is the system of neutral atoms. Their internal level structure, hyperfine levels in particular, can be used as states of qubits while coupling between qubits can be provided by atom-atom interactions. Due to their neutrality, the interaction of atoms with the environment is weak, which results in long coherence times. In addition, well-developed techniques for trapping cold atoms provide good control. We will consider a development of a $CNOT$-phase gate based on the conditional excitation to Rydberg states.

5.2 Quantum Computing with Rydberg States

In contrast to ions it is difficult to have strong interactions between neutral atoms that are required for a realization of a fast quantum gate. The coupling between two atoms can be implemented through control of their internal structure, for example by means of collisions [67], photon exchange between atoms in a cavity [68] and the dipole-dipole interactions between Rydbergs atoms [69].

Alkali atoms may act as quantum bits. In case of rubidium-87, the hyperfine ground state levels can be used as states of the qubit,

$$|\,0\,\rangle \longleftrightarrow 5s_{1/2}|\,F=1, m=0\,\rangle$$

$$|\,1\,\rangle \longleftrightarrow 5s_{1/2}|\,F=2, m=0\,\rangle.$$

The hyperfine structure and Zeeman splitting of ^{87}Rb are thoroughly studied and well-understood [70]. The states can be addressed by microwave radiation or optical Raman transitions, and the interaction between two ground state atoms is negligible. The $|\,F=2\,\rangle$ ground state is employed in the laser-cooling cycling transition; atoms can be pumped to this state efficiently, and it can be naturally considered as a prepared initial state for an ensemble of qubits. A single qubit

rotation with a fidelity[1] of 0.99 was demonstrated recently [71].

The conditional operations required for realization of a two-qubit $CNOT$ gate can be achieved by altering the state of a target qubit with a control qubit. For example, if and only if the logic state of the control qubit is $|\,1\,\rangle$, the state of the target qubit flips. Such control gate can be realized using the Rydberg blockade effect [69]. Consider two atoms, A and B initially in their two hyperfine ground states $|\,0\,\rangle$ and $|\,1\,\rangle$ as illustrated in Fig. 5.1. The atoms can be coupled to a Rydberg level $|\,r\,\rangle$ with a high principle quantum number by means of a direct optical excitation or through an intermediate state such that states $|\,1\,\rangle$ and $|\,r\,\rangle$ form an effective two-level system. When atom A is in the Rydberg state it shifts the Rydberg energy of the second atom B by Δ_{rr} thus detuning the atomic resonance of atom B with respect to the excitation laser. The system is controlled by a sequence of π-pulses[2] according to the following protocol: (1) excite atom A to the Rydberg state $|\,r\,\rangle$ with a π pulse, (2) while atom A is the Rydberg state, apply a 2π pulse resonant with the $|\,0\,\rangle \leftrightarrow |\,r\,\rangle$ transition for atom B, and (3) de-excite atom A to state $|\,0\,\rangle$ with a π pulse. A qubit rotation between states $|\,0\,\rangle$ and $|\,1\,\rangle$ can be achieved by a microwave radiation as necessary.

Depending on the initial state of the 2-qubit system the gate operation will have the following result:

$$
\begin{aligned}
|\,00\,\rangle \xrightarrow{1} -i|\,r0\,\rangle \xrightarrow{2} -ie^{i\phi}|\,r0\,\rangle \xrightarrow{3} -e^{i\phi}|\,00\,\rangle,\\
|\,01\,\rangle \xrightarrow{1} -i|\,r1\,\rangle \xrightarrow{2} -i|\,r0\,\rangle \xrightarrow{3} -|\,00\,\rangle,\\
|\,10\,\rangle \xrightarrow{1} |\,10\,\rangle \xrightarrow{2} -|\,r0\,\rangle \xrightarrow{3} -|\,00\,\rangle,\\
|\,11\,\rangle \xrightarrow{1} |\,11\,\rangle \xrightarrow{2} |\,r0\,\rangle \xrightarrow{3} |\,00\,\rangle,
\end{aligned}
$$

that coincides with the $CNOT$-matrix in Eq. 5.1 when a single-qubit Hadamard gate is applied to atom B. The extra phase shift term $e^{i\phi}$ is due to the off-resonant

[1]for two pure states ψ and ϕ, fidelity is defined as $|\langle\psi,\phi\rangle|$

[2]the definition of the π-pulses is given in Appendix A

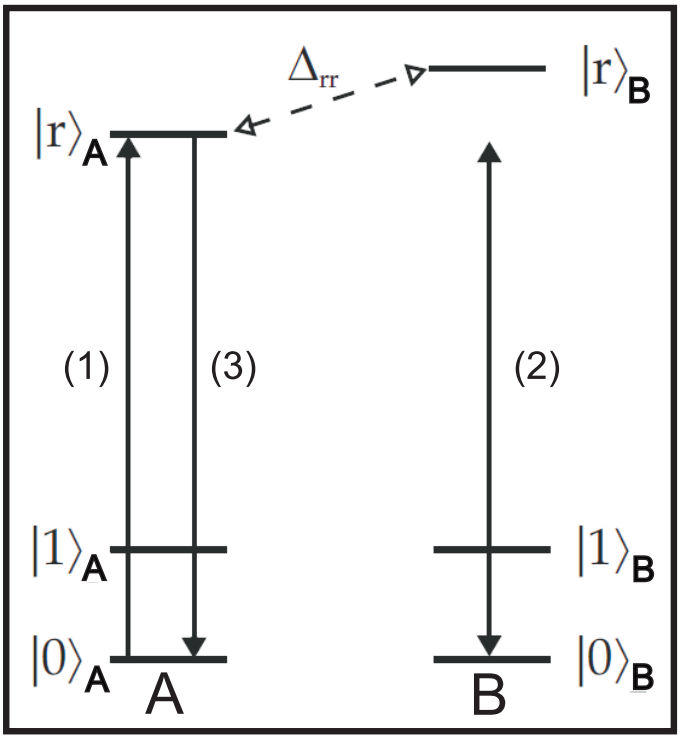

Figure 5.1: The controlled 2-qubit phase gate based on the Rydberg blockade effect. Logic state of atom A controls the state of the target atom B by altering its Rydberg state energy.

coupling between the ground and the Rydberg states of atom B when atom A is excited. The phase shift can be evaluated from the 2-level evolution operator [72] to find $\phi = \pi\Omega_R/2\Delta_{rr}$, where Ω_R is the Rabi frequency of the Rydberg excitation of atom B. For strong interactions, one can achieve $\Delta_{rr} >> \Omega_R$ and the unwanted phase shift can be suppressed. The gate operation time is $t_{op} = 2\pi/|\Omega_A| + 2\pi/|\Omega_B|$, where $\Omega_{A,B}$ are the Rabi frequencies for the corresponding atoms. According to the DiVincenzo criterion, the gate operation time must be shorter than the coherence time of the qubit, set by the radiative decay of the Rydberg state.

The idea of the two-qubit blockade gate can be extended to an ensemble of qubits, each consisting of N atoms [73]. The extension relies on the concept of the collective Rydberg blockade, in which excitation of a single atom to a Rydberg

state can block the subsequent excitation of a large number of atoms within the interaction volume. If the blockade shift is sufficiently large, the simultaneous excitation of two or more atoms is prevented and the enhanced Rabi frequency is given by $\Omega_N = \sqrt{N}\Omega$. Two-qubit gates can then be implemented between two ensemble qubits or between a single atom and an ensemble qubit analogous to the single atom protocol of Fig. 5.1.

The Rydberg blockade idea spurred a large amount of theoretical and experimental work and was further developed beyond the original proposals [69, 73]. For a detailed and up-to-date review on the subject please refer to Ref. [74].

5.2.1 Properties of Rydberg-Rydberg Interactions

Rydberg atoms with high principal quantum number n are potentially useful due to their long radiative lifetimes and strong atom-atom interactions resulting in large values of Δ_{rr}. In the absence of external fields, the eigen-states of a hydrogen-like alkali atom can be represented by quantum numbers n, l, s, and j denoting the principal, orbital angular momentum, spin angular momentum, and total angular momentum quantum numbers. The energy levels are accurately represented by the quantum defect theory [75]

$$E_{nlj} = -\frac{R_y}{(n^*)^2}, \qquad n^* = n - \delta_{lj}(n), \tag{5.2}$$

where $Ry = 109737.3\, cm^{-1}$ is the Rydberg constant, and the quantum defect $\delta_{lj}(n)$ is a slowly varying function of the principal quantum number [76].

5.2.2 Radiative Lifetime

The qubit coherence time is limited by the radiative decay and the black-body ionization rates of a Rydberg state that is close to the ionization limit. The finite temperature lifetime τ_{nl} is [75]

$$\frac{1}{\tau_{nl}} = \frac{1}{\tau^0_{nl}} + \frac{1}{\tau^{(bb)}_{nl}} \tag{5.3}$$

where τ_{nl}^0 is radiative lifetime at 0 K, and $\tau_{nl}^{(bb)}$ is the finite temperature blackbody contribution. The 0 K radiative lifetime can be parameterized by the expression [77]

$$\tau_{nl}^0 = \tau_l^0 (n^*)^{\alpha_l}, \tag{5.4}$$

where the value of numerical constants τ_l^0 and α_l are tabulated in reference [75]. For all alkali atoms, $\alpha_l \approx 3$, for low l states. The blackbody ionization rate can be approximated for large values of n as [75]

$$\tau_{nl}^{(bb)} = \frac{4\alpha^3 k_B T}{3\hbar n^2}, \tag{5.5}$$

where α is the fine structure constant and T is the characteristic temperature of the blackbody radiation. For $n \sim 50$, the Rydberg state lifetime is about $100\,\mu s$ at room temperature, about half from blackbody and half from the radiative contributions.

5.2.3 Rydberg-Rydberg Interaction Strength

The long-range interactions between two Rydberg atoms are extremely strong and are the core of the quantum computation scheme discussed here. We consider the Rydberg-Rydberg interactions in two limits: at zero electric field, where the long-range $1/R^6$ van der Waals interactions are of primary importance, and in a large external electric field, where the atoms have a dipole moment of magnitude $n^2 e a_0$, where e is the electron charge and a_0 is the Bohr radius of the alkali atom.

At interatomic distances $R >> n^2 e a_0$ between two Rydberg atoms A and B, the leading electrostatic interaction is the dipole-dipole interaction, that can written in atomic units as

$$V_{dd} = \frac{e^2}{R^3}\left[\boldsymbol{a}\cdot\boldsymbol{b} - 3(\boldsymbol{a}\cdot\hat{\boldsymbol{R}})(\boldsymbol{b}\cdot\hat{\boldsymbol{R}})\right], \tag{5.6}$$

where $\boldsymbol{a}$ and $\boldsymbol{b}$ are the positions of the two Rydberg electrons measured from their respective nuclei.

When the two atoms are excited by light to the same fine-structure level, the two-atom unperturbed state for $R = \infty$ can be written as $|\,\psi_2\,\rangle = |\,\psi_A\psi_B\,\rangle$. At zero field, the energy shift of the $50s$ states is due to the van der Waals interaction dominated by the near resonance between the states $|\,50s + 50s\,\rangle$ and $|\,50p + 49p\,\rangle$, with the energy defect $\delta = E(49p) - E(50p) - 2E(50s) = -3$ GHz. If we neglect the contribution from other states, the energy shift will be given by [74]

$$V(R) = \frac{\delta}{2} + \sqrt{\frac{4U_3(R)^2}{3} + \frac{\delta^2}{4}}, \tag{5.7}$$

where $U_3(R) = e^2\langle\, 50s\,||r||\,50p\,\rangle\,\langle\, 50s\,||r||\,49p\,\rangle/4\pi\epsilon_0 R^3$. For large defects $\delta >> U_3$, the expression for the energy shift is characterized by $1/R^6$-dependence:

$$V(R) = -\frac{4U_3(R)^2}{3\delta} \sim \frac{1}{R^6}, \tag{5.8}$$

The Rydberg dipole moment scales as n^2, the energy defect as $1/n^3$, resulting in a n^{11}-dependent energy shift. Therefore the excitation to high Rydberg levels is advantageous for a practical realization of the Rydberg blockade.

The $1/R^6$ interaction can be enhanced either by applying an electric field or by using resonances. If the excitation levels can be chosen such that the energy defect is small in comparison with the interaction strength (Förster resonances), Eq. 5.7 is reduced to the dipole-dipole $1/R^3$ interactions

$$V(R) = \sqrt{\frac{4}{3}}\,U_3(R) \sim \frac{1}{R^3}.$$

Note, that an external electric field can be used to tune the Rydberg states to Förster resonances through the Stark energy shift as discussed in the recent review [78].

Another approach to increase the interatomic interaction and the corresponding energy shift relies on the application of the external electrostatic field E. For small fields, the interaction energy $e\langle\, r\rangle\, E$ between the induced dipole moment and the field is less than the energy difference with the nearest opposite parity state, Δ, and the Stark effect is quadratic in the field. As the electric field gets higher, the

mixing of states with different orbital angular momenta gives rise to a Rydberg atom with a constant electric dipole moment on the order of $n^2 e a_0$, that results in the linear Stark effect. The permanent dipole moment μ provides the strong $1/R^3$ dipole-dipole interaction, which from Eq. 5.6 can be written in SI-units as

$$V_{dd} = \frac{\mu^2}{4\pi\epsilon_0 R^3}(1 - 3cos^2\theta), \tag{5.9}$$

where θ is the angle between the interatomic axis and the electric field. Note, that the interaction is anisotropic, which may reduce the corresponding overall energy shift in a macroscopic sample. Control of the dipole-dipole interactions by an external electric field is the subject of this dissertation and is considered in more detail in Chapter 6.

5.3 Experimental Progress in Realization of Rydberg Quantum Gate

5.3.1 Traps for Neutral Atom Qubits

Thw practical realization of quantum computing devices based on neutral atoms relies on the ability to trap the atoms to constrain their motion, select and address the states of the quantum system, and provide a conditional coupling between two or more qubits. Individual atoms were successfully trapped in a MOT [79], and later in far-off resonance optical traps (FORTs) [80]. Various red- and blue-detuned optical traps were discussed in some details in the first part of this dissertation. For large trap detunings and depths, the trap lifetime is limited by the collisions with the background gas and can be many orders of magnitude longer than the desired time of qubit operations. Atomic motion within the trap beam results in AC Stark shifts of the qubit states, which can be a limiting factor for qubit coherence in FORTs [81]. For the conditional coupling realized through the Rydberg-Rydberg

interaction, the high power optical trap can cause photoionization with the rate substantially higher than the radiative decay rate. Those effects can be significantly reduced by confining the atom in dark optical traps where the atoms are localized near an intensity minimum. We are not aware of any experimental demonstration of trapping single atom qubits in blue-detuned optical potentials. Magnetic traps are characterized by very long coherence times, and an array of such traps [82] can be promising for scalability of trapping to many qubits. Unfortunately, it may be difficult to combine magnetic traps with Rydberg atoms. To achieve tightly confining magnetic traps on a chip the trap position is close to the surface of the chip, which can lead to undesired interactions between the surface and a Rydberg atom.

5.3.2 Excitation of Rydberg States

A trapped neutral atom can be encoded as a qubit using its hyperfine or Zeeman ground states. Practical realization of the conditional gates based on the atom-atom interactions requires precise excitation and deexcitation of Rydberg states. Early work of laser excitation and spectroscopy of Rydberg atoms is reviewed in reference [83]. One photon Rydberg excitation from the ground state of rubidium was recently demonstrated with 297 nm light generated by a frequency-doubled dye laser [84]. We choose to excite a Rydberg state through a two-photon transition, specifically with the intermediate state close to $5p_{3/2}$ state. In this case, the first photon is at 780 nm (red), and can be provided by one of the cooling lasers that couple the ground state with the $5p_{3/2}$ state. The second photon must be at 480 nm (blue), which can be generated by a frequency-doubled diode or Ti:Sapphire lasers. A diagram of the two-photon excitation is shown in Fig. 5.2. The first example of Rydberg spectroscopy with narrow linewidth lasers using excitation scheme was a study of Autler-Townes spectra in a cold ^{85}Rb sample [85]. Our observation of the Autler-Townes spectra in ^{87}Rb MOT is reported in Chapter 6.

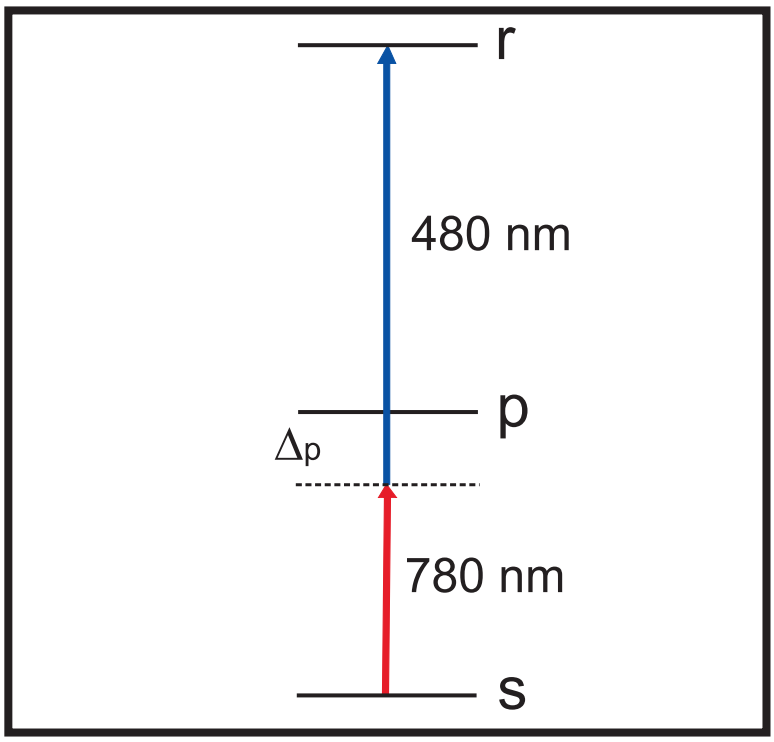

Figure 5.2: Schematic of the two-photon excitation of the Rydberg state $|\,r\,\rangle$. The excitation lasers at 780 (red) and 480 nm (blue) are detuned by Δ_p from the intermediate level $|\,p\,\rangle$ to reduce its population.

Rabi oscillations between ground and Rydberg levels were recently demonstrated for single ^{87}Rb atoms confined to an optical trap [86]. Rydberg excitation to $43d_{5/2}$ state was provided by π -polarized lasers at 780 and 480 nm. The excitation laser beams had waists that were a few times larger than the width of the optical trap so the effects of spatial variation of the Rabi frequency were minimized. The dipole trap laser was turned off before the excitation lasers were applied to avoid the photoionization of the Rydberg atoms. After a variable length excitation pulse the trap was turned on again which photoionized the Rydberg atoms before they could radiatively decay. Loss of a Rydberg atom from the trap provided a measure of Rydberg excitation. The reported Rabi oscillations are shown in Fig. 5.3. Collective excitation in ensembles were also observed using the stimu-

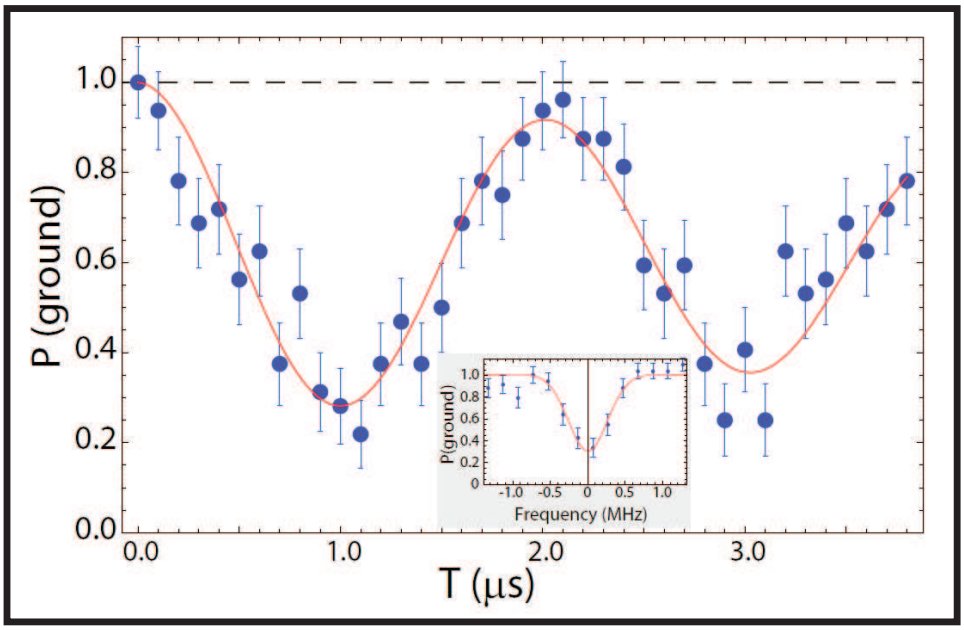

Figure 5.3: Rabi oscillations between ground and $43d_{5/2}$ rubidium Rydberg level. Reproduced from reference [86].

lated Raman adiabatic passage (STIRAP) with a counterintuitive pulse sequence where the 480 nm laser is applied before the 780 nm [87]. Excitation probabilities of up to 70% were demonstrated.

5.3.3 Experimental Realization of Two-qubit Rydberg Gates

It has recently been shown by the research groups in Wisconsin and at the Institute of Optics, Palaiseau, France that the experimental methods of single atom trapping, coherent excitations and control over Rydberg-Rydberg interactions can be combined to demonstrate Rydberg blockade [88, 89], and a two-qubit Rydberg gate [90]. The blockade experiment in Wisconsin [88] showed that excitation of a Rb atom to the $90d_{5/2}$ state blocked the subsequent excitation of the second atom at a distance $R \geq 10\mu m$ with a fidelity of about 90%. Experimental data, together with a Monte-Carlo simulation taking into account the finite blockade strength and experimental imperfections are shown in Fig. 5.4.

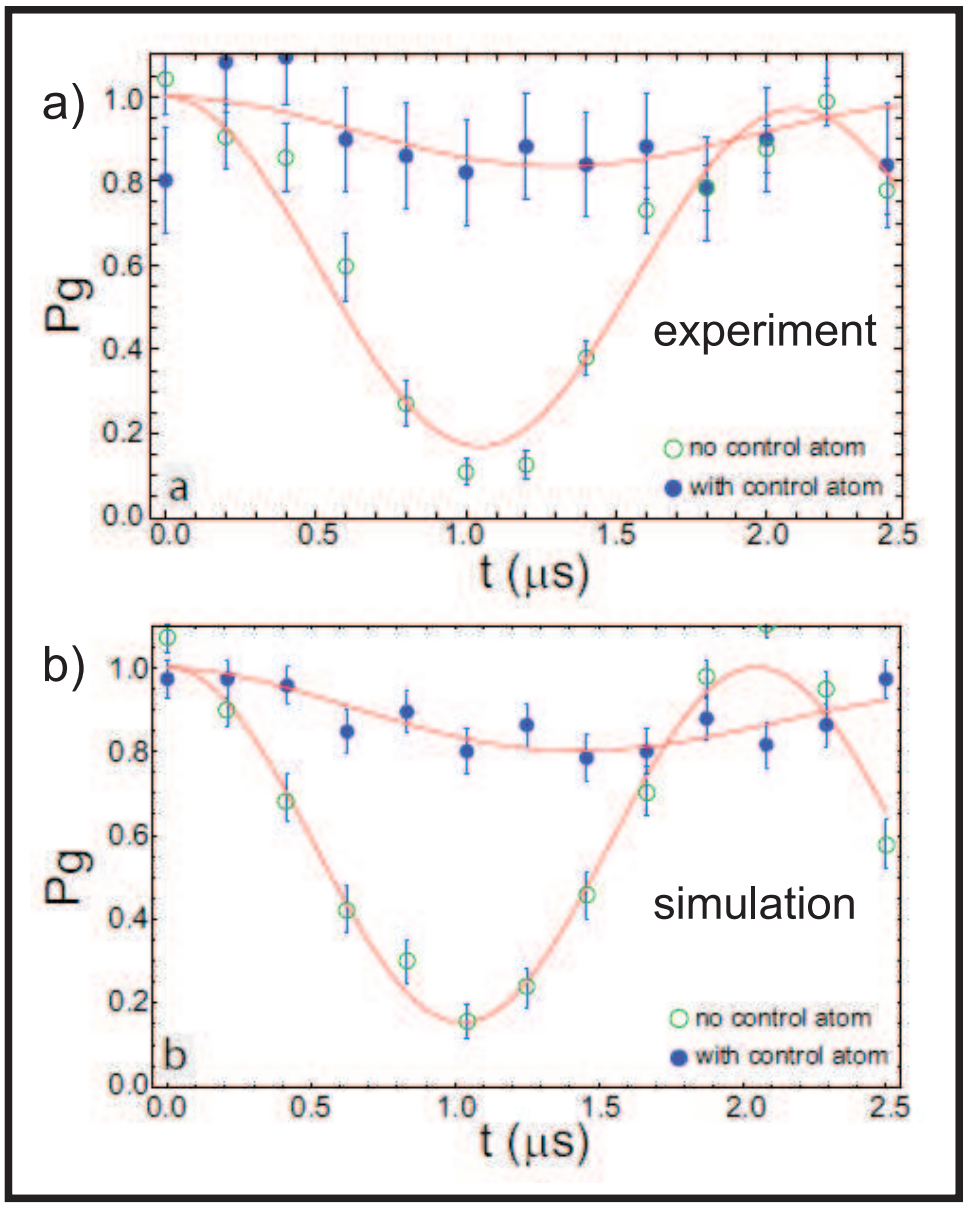

Figure 5.4: a) The experimental data for Rydberg excitation of the target atom with and without a control atom present. b) A Monte Carlo simulation accounting for experimental imperfections. The amplitude of the curve fit to the blockaded oscillations is a = 0.09 (experiment) and a = 0.11 (simulation). Reproduced from reference [88].

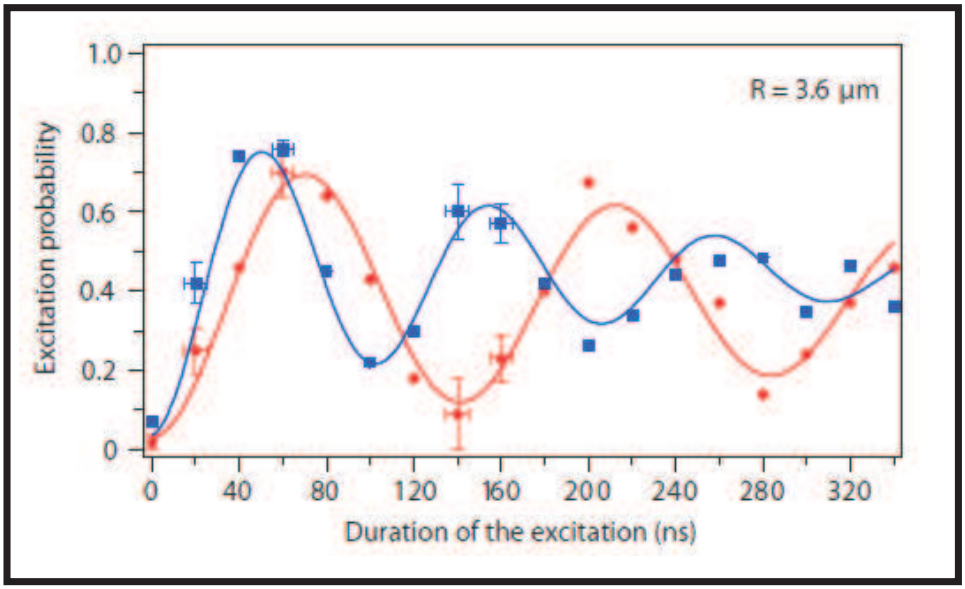

Figure 5.5: Excitation of one atom versus collective excitation of two atoms separated by $3.6\mu m$. The circles represent the probability to excite atom a when atom b is absent. A fit to the data yields a frequency of this Rabi oscillation $\Omega/2\pi = 7.0 \pm 0.2$ MHz. The squares represent the probability to excite only one atom when the two atoms are trapped and are exposed to the same excitation pulse. The fit gives an oscillation frequency $\Omega/2\pi = 7.0 \pm 0.2$ MHz. The ratio of the oscillation frequencies is 1.38 ± 0.03 close to the value $\sqrt{2}$ expected for the collective oscillation of two atoms. Reproduced from reference [89].

A closely related experiment in Palaiseau [89] used simultaneous excitation of two Rb atoms in optical traps separated by $R \sim 3.6\,\mu m$. A very strong blockade shift was obtained by using the $58d_{3/2}$ Förster resonance. The excitation was provided through the $5p_{1/2}$ state by 794 nm light. As shown in Fig. 5.5, the excitation that couples the two atom state to the singly excited state was characterized by the collectively enhanced Rabi frequency $\Omega_c = \sqrt{2}\Omega$.

The realization of the 2-atom Rydberg blockade was later combined with the coherent Rabi oscillations experiment to demonstrate a $CNOT$ gate [90]. The probabilities of the prepared initial state and the output of the Rydberg gate are

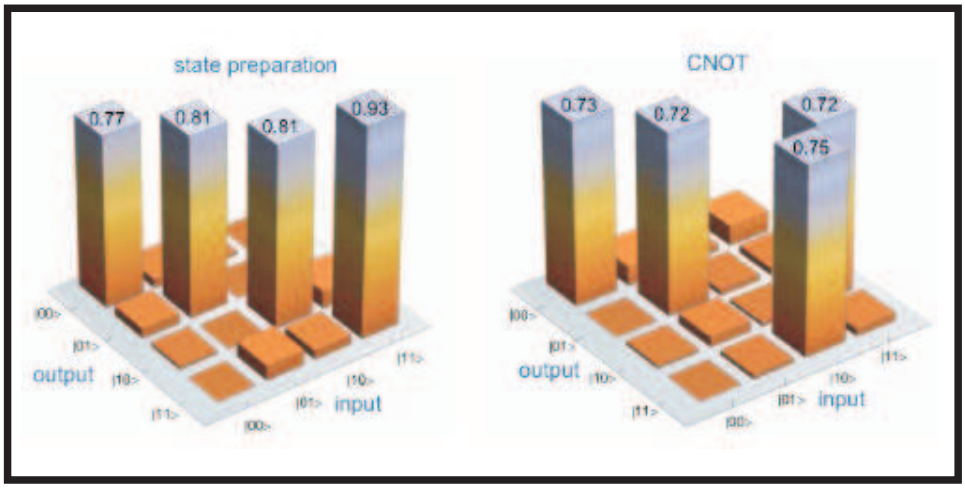

Figure 5.6: Practical realization of the Rydberg $CNOT$ gate. Measured probabilities for state preparation (left) and $CNOT$ output (right). Reproduced from reference [90].

shown in Fig. 5.6.

Although promising, the initial results should only be considered as first steps as they lag far behind the high fidelity results obtained with trapped ions [91].

5.3.4 Blockade Effect in Many-atom Systems

With the proposed application of the Rydberg blockade effect to quantum computing, most experimental efforts were aimed at the study of the Rydberg excitation and interatomic interactions in cold atomic samples of many atoms. Bulk samples are hard to envision to use for the quantum information processing but their study provides deeper understanding of the properties of Rydberg atoms and promote development of new techniques to realize a single 2-qubit gate and extend it to scalable systems required for quantum computation.

Original experiments to study the behavior of cold Rydberg atoms in MOTs showed the signatures of Rydberg-Rydberg interactions [92, 93]. In case of the large samples, the Rydberg interactions occur on the μm-scale, much smaller than

1 mm, the size of a large atomic cloud. To characterize the blockade phenomenon it is convenient to introduce a concept of the "blockade sphere" [94]: a single excited atom blocks further excitations with a sphere of radius R_b. The radius is set by the range of interatomic interactions. As the sphere contains indistinguishable N_b atoms in the ground state, they comprise an effective "superatom" that interacts with the excitation light with a collective $\sqrt{N_b}$ enhancement of the Rabi frequency Ω [95]. The blockade radius is set by the condition that the collective Rabi frequency be comparable to the dipole-dipole shift, which results in the excitation fraction to be [96]

$$\kappa \propto \left(\frac{\Omega}{\eta^2 C_6}\right)^{2/5},$$

where η is the atomic density of the sample and C_6 is the amplitude of the van der Waals interaction, which scales as n^{11}. The dependence of the excitation fraction on the excitation pulse intensity, and thus C_6, is illustrated by Fig. 5.7 [94]. A factor of 2 ratio of the excitation fraction for the $70p$ and $80p$ data was consistent with the blockade density scalings, and the comparison of either with the excitations to the $30p$ state dramatically shows the overall blockade effect.

These suppression effects could be considerably enhanced for the dipole-dipole interactions resulted by tuning a Förster resonance with an electric field. A direct comparison between the van der Waals and Förster-enhanced blockade was reported [97].

Another signature of the excitation blockade in extended samples would be a resonance broadening of the Rydberg transition. Density variations that change interatomic distances or control over the interaction strength may give rise to a shift of the atomic resonance with respect to the frequency of the excitation laser for a fraction of the atomic cloud. The resulted broadening can be observed in spectroscopic measurements. We have assembled an experimental apparatus to excite rubidium atoms to Rydberg states and investigate the excitation in the presence of an electric field when the transition from the van der Waals to the dipole-dipole

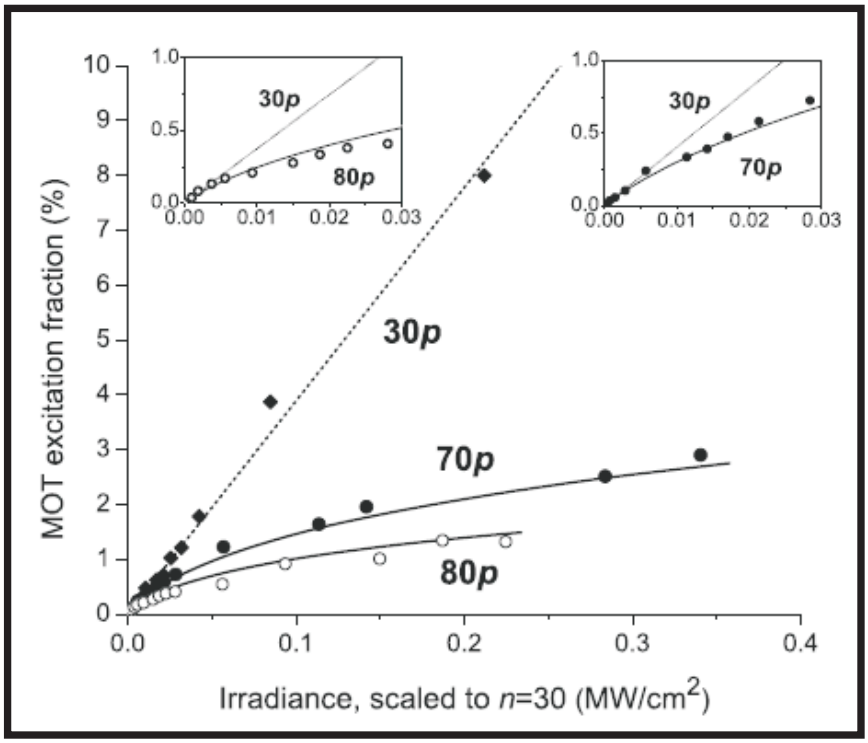

Figure 5.7: Dependence of excitation fraction on principle quantum number for the excitations to 30p, 70p and 80p Rydberg states. Reproduced from reference [94].

interactions is expected to enhance the blockade effect at higher fields.

Chapter 6

Experimental Setup

Practical realization of quantum logic gate protocols introduced in Chapter 5 relies on the efficient excitation of atoms to a specific Rydberg state. The rate of excitation to the Rydberg state depends on the convolution of the linewidth of the transition for a stationary atom (< 100 kHz), the Doppler broadening due to the atom's motion and the linewidth of the excitation laser. The Doppler broadening can be reduced to a few hundred kHz by cooling the atoms below the temperature of a few hundred μK and trapping them such that their position in space is fixed with respect to the excitation laser light. A narrow linewidth[1] of the excitation laser system is required to not limit the excitation rate and to be able to exclusively address a desired Rydberg level. To observe the blockade effect, the resolution of the excitation laser must be smaller than the energy shift of a few MHz due to the Rydberg-Rydberg interactions. In addition, the laser light should be continuously tunable, to make spectroscopic measurements of the Rydberg states and investigate the Stark shift due to an external electric field.

6.1 Cold Atom Apparatus

To cool and trap neutral atoms, and excite them to Rydberg states, we used a BEC apparatus assembled by our colleagues, Emily Edwards and Matthew Beeler, specifically designed for the experiments with rubidium atoms trapped in optical

[1]Usually, a diode laser with an extended cavity has a $\sim$ MHz linewidth.

lattices [29]. Here we briefly describe the cold atom machine, discuss its advantages and the drawbacks as an apparatus to study the Rydberg states for various parameters of the cold atomic clouds. It must be pointed out, that we did not participate in the development of this apparatus, but benefited from its existence, as it was used throughout the work reported here.

The apparatus, a sophisticated version of the laser cooling setup described in Appendix A, allowed a production of a cold rubidium cloud held in a magneto-optical trap, further cooling of the cloud in an optical molasses, its subsequent transfer to a pure magnetic trap, radio-frequency evaporation of the cloud in the magnetic trap to achieve quantum degeneracy of the trapped atoms, and its transfer to a dipole trap created by a red-detuned focused laser beam. We investigated different approaches to produce Rydbergs atoms in the MOT, molasses, the magnetic and dipole traps.

A part of the ultra-high vacuum (UHV) chamber for the BEC experiments is presented in Fig. 6.1. The chamber pressure of $\sim 3 \cdot 10^{-11}$ Torr was maintained by a combination of an ion and a titanium sublimation pump that provided a lifetime of many seconds for the trapped rubidium sample. A Zeeman slower was used as a source of atoms for a mirror-MOT setup [98] and allowed fast turn on and off times of the cloud loading. The long lifetime of the cloud allowed to excite atoms to Rydberg states for up to 50 ms, when the laser induced excitation was the sole mechanism responsible for the change of the ground state population. The setup provided a collection of $10^7 - 10^9$ atoms in a MOT, and a 50% transfer efficiency to the magnetic trap. The magnetic confinement with a depth of 1 mK was provided by an interaction of the magnetic moment of atoms in the $| F = 2, m_f = 2 \rangle$ ground state with a magnetic field generated by Z-shaped conductor in vacuum and a bias field with the components along x- and y-directions (Fig. 6.1). Further evaporative cooling in the magnetic trap allowed us to change the density of the atomic cloud by varying the evaporation time.

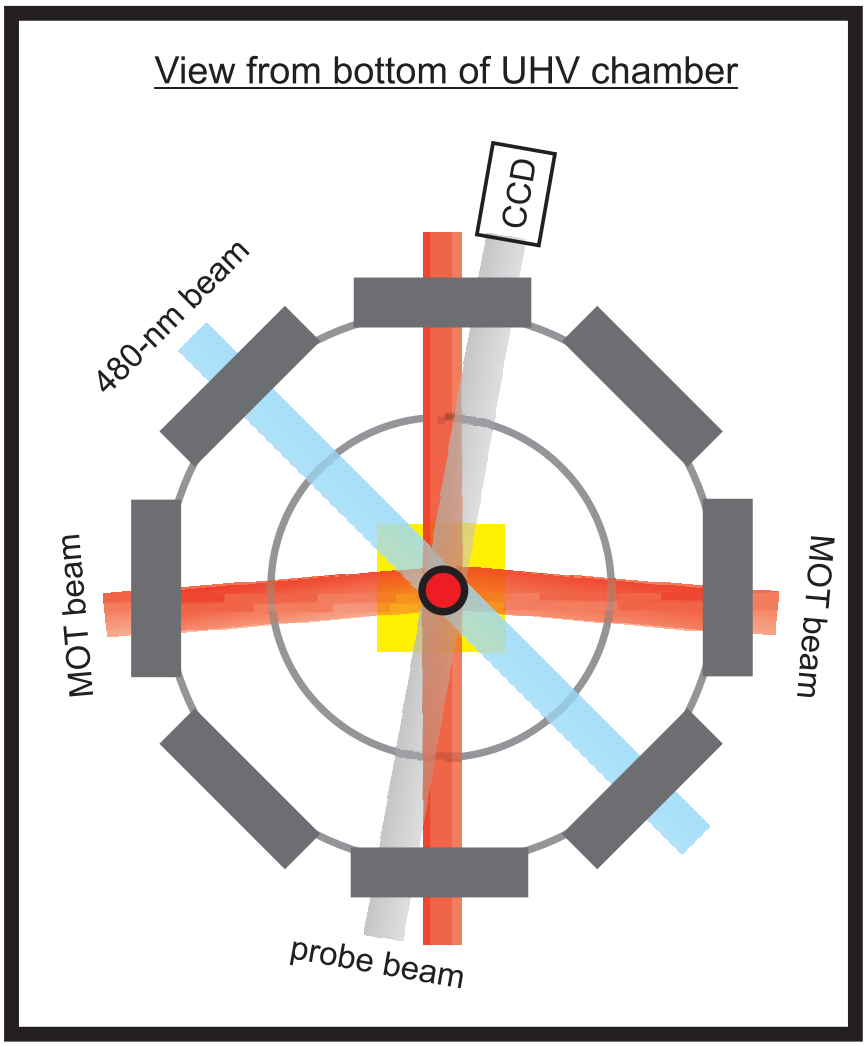

Figure 6.1: View from the bottom of the UHV chamber showing orientation of a 480-nm Rydberg excitation beam (blue) and input beams for the MOT (red). There are four MOT beams total, two from the side and two from the bottom. The reflection off the gold mirror gives the other two required beams for 3-D cooling in the MOT. Absorption from a probe beam (grey) is detected by a CCD camera to measure the MOT atom number. Detailed description of the chamber can be found in Ref. [29].

6.1.1 Generation of Static Electric Field

Both Rydberg and optical lattice experiments used the same apparatus, and modifications of the existing apparatus required for the Rydberg project were not always

performed in the optimal way in order to keep the setup compatible with the needs of both experiments. For example, to perform the Rydberg excitations in the presence of the static electric field we utilized already existing conductors in the vacuum chamber, although they were not intended to be field electrodes. The field was generated between the gold mirror, which was grounded by the way it was mounted, and two metal conductors kept at a positive voltage. We used rubidium dispensers, already inside the chamber, as the positive electrodes. The dispensers, a legacy atomic source that was unused after the installation of the slower, were connected to a high-voltage source through the UHV electrical feedthroughs. The voltage was computer generated and amplified by a high-voltage amplifier (PZD350, TREK). The dispensers were kept at a constant potential with no current flowing through them, such that their temperature remained constant, and no rubidium was released. In this configuration the dispensers can be treated simply as metal plates, 5 mm wide and 3 cm long. The arrangement of the electrodes and the atomic cloud is shown in Fig. 6.2.

The asymmetric positioning of the positive electrodes with respect to the location of the atomic cloud was set by the fixed orientation of the electrical feedthroughs. The electrodes were placed above the level of the gold mirror not to restrict the optical access and block the MOT laser beams. The spatial profile of electric field generated by the described set of electrodes and the grounded surface of the stainless steel vacuum chamber was quite complex and could not be calculated precisely, as the exact locations and sizes of all nearby electrodes and grounded surfaces were not accurately known. A simplified configuration of the electrodes was considered, and the resulting electric field was compared to the Stark shift data as discussed in details in Chapter 7. We note that the given configuration of small electrodes placed far from, and not symmetric with respect to the cloud, resulted in an inhomogeneous electric field, complicating the experimental investigation of the Rydberg excitation rate. Unfortunately, a more significant modification of the existed apparatus to improve the field homogeneity,

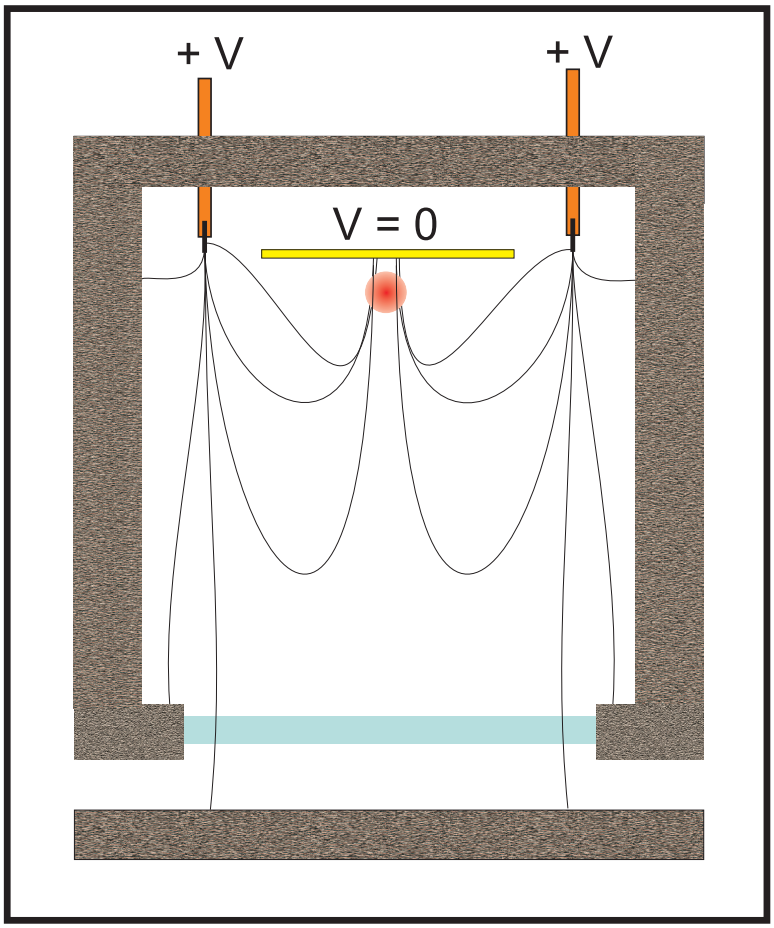

Figure 6.2: Grounded surfaces of a 3 × 3 cm gold mirror, chamber walls and the optical table, and two thin metal plates 3 cm long and 5 mm wide kept at a constant potential V formed an electric field at the location of the cold cloud, several millimeters below the mirror. A few field lines are shown inside the chamber and out through the bottom glass window.

was not possible. Originally, we tried to place an electrode outside the chamber, below the bottom glass window, to form the electric field between the electrode and the grounded gold mirror. As the Rydberg excitation is followed by a partial black-body ionization of the sample, it resulted in production of electric charges accelerating toward the appropriate electrode when the field is on. In this configuration, the charges moving towards the outside electrode hit the glass window and

accumulate on the surface of the dielectric. Indeed, we observed an accumulated surface charge at higher fields, that was sufficient to completely shield the electric field at the location of the atomic cloud.

6.1.2 Detection of Rydberg Atoms

Absorption imaging was used as the detection method to characterize a cold cloud and the Rydberg excitations[2]. The absorption imaging allowed a measurement of the cloud's atom number and its spatial profile across the probe beam for the atoms in the $5s_{1/2}|\, F = 2\,\rangle$ ground state. As the atoms are excited to a Rydberg state, they might return back to the ground state through lower levels (*e.g.,* $5p$ or $6s$), or get ionized by black-body radiation. In the case of ionization, an atom (now a positively charged ion) is not resonant with the probe beam anymore and not held by a cold atom trap. The resulting trap loss can be detected by the absorption imaging technique to measure the Rydberg excitation rate. The rate of ionization is very small in comparison with the de-excitation rate to the ground state, and long excitation times (on the order of several milliseconds) were required to observe trap loss above the noise level of the experiment. On this time scale some properties of the cloud, like density, may change significantly, which complicates the analysis of the obtained results. Excitations on much shorter time scales are usually studied by a field-ionization of Rydberg atoms in a Microchannel Plate (MCP) detector (plates and grids to accelerate ions to an electrode, and count the number of the arrived charges as electric current). Unfortunately, the MCP was not an available detection technique for our experimental setup, as it would limit optical access to the cloud making it incompatible with the optical lattice experiment. A simplified population dynamics of the Rydberg excitations is discussed in Appendix D.

[2]Absorption imaging is discussed in Appendix C

6.2 Generation of Frequency-stabilized Laser Light at 480 nm

The energy gap between the rubidium ground state and its excited state with the principal quantum number $n = 50$ corresponds to 297 nm. There is no gain medium available to construct a laser system at that wavelength; usually the light in this part of the optical spectrum is generated by frequency doubling. Another constraint is that only the lower angular momentum states can be excited from the $l = 0$ ground state as allowed by the selection rules in the dipole approximation ($\Delta l = \pm 1$). Also, in Rb the Cooper minimum makes the cross section for excitation quite small, requiring high laser intensities. However, an observation of electric quadrupole transitions to Rydberg nd states was recently reported [99]. It is advantageous to excite a Rydberg state through a two-photon transition, specifically with the intermediate state close to $5p_{3/2}$ state. In this case, the first photon is at 780 nm (red), and can be provided by one of the cooling lasers that couple the ground state with the $5p_{3/2}$ state. The second photon must be at a more convenient wavelength, 480 nm. Practically, we used the same laser beams at 780 nm to cool and trap rubidium atoms (DLX-110 laser, Toptica Photonics), and to provide the first step in the two-photon ladder excitation scheme. The frequency of the red light was controlled by a double-pass AOM, which allowed detunings of up to 56 MHz from the $5s_{1/2}|\, F = 2\,\rangle \rightarrow 5p_{3/2}|\, F = 3\,\rangle$ atomic transition. The blue light was generated by doubling the frequency of a 960-nm laser in a non-linear crystal in a build-up cavity.

An efficient excitation of Rydberg states requires narrow linewidth laser light, with frequency stabilization and tuning. A diagram of the laser system we assembled to generate the frequency-stabilized light at 480 nm is shown in Fig. 6.3.

The laser system was set up on a dedicated air-suspended optical table to damp vibrations, and enclosed in a plexiglass box to protect the setup from air

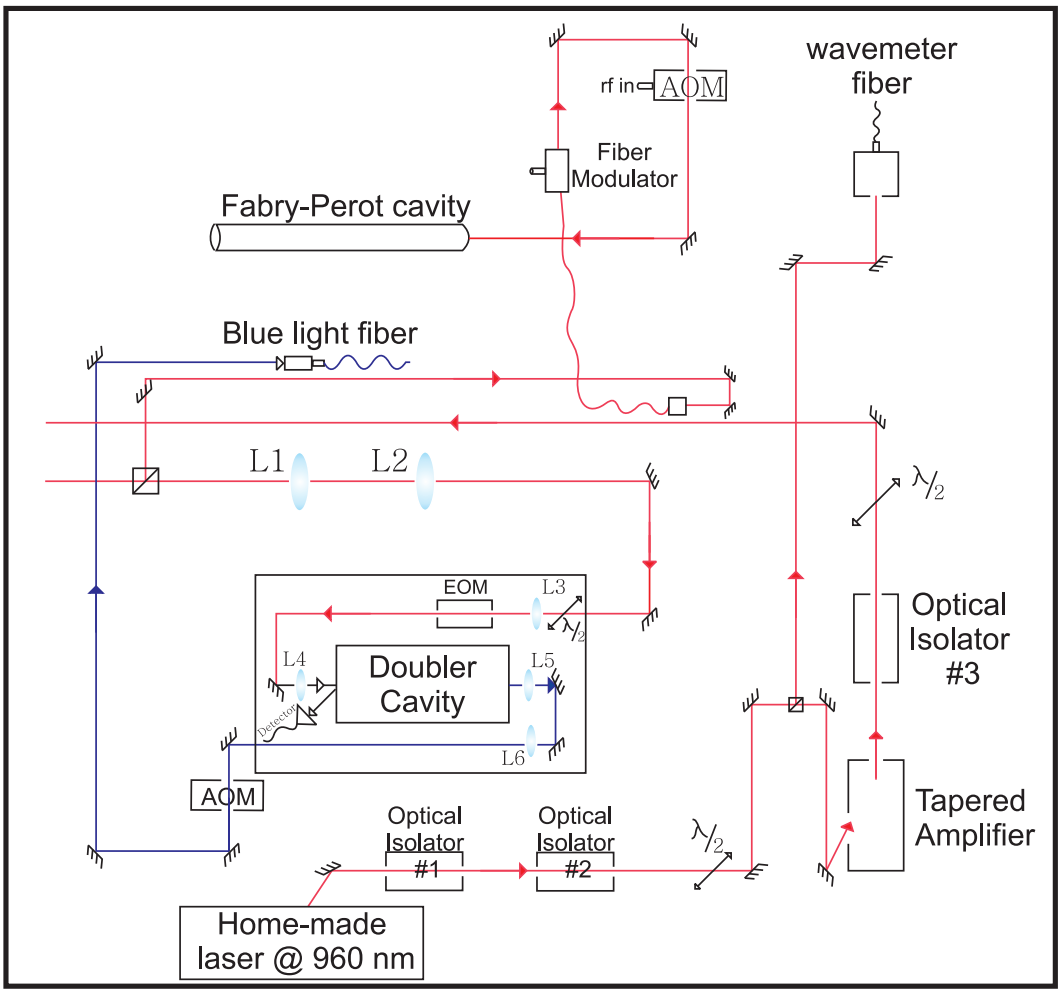

Figure 6.3: The optical layout for the blue light generation setup. The 960-nm laser seeds a tapered amplifier. The output of the amplifier is frequency-doubled to generate laser light at 480 nm. The wavelength of the red light is locked to a Fabry-Perot cavity, and monitored by a wavelength meter. Spherical lenses L1-L4 shape the 960-nm beam, L5-L6 - the 480-nm beam. Acousto-optical modulators (AOM) and an electro-optical modulator (EOM) are used to modulate the frequency of the 960-beam. Half-wave plates ($\lambda/2$) are used to rotate the beam polarization.

currents and reduce acoustic noise that might limit the stability of the laser. A home-made external cavity diode laser at 960 nm pumped a tapered amplifier. The output beam from the amplifier was shaped by a lens system to match a

fundamental eigenmode of a commercial frequency doubling cavity. The generated second harmonic of the cavity at 480 nm was beam-shaped, coupled to an optical fiber, and delivered to the optical table that hosted the cold atom apparatus. A detailed description of the components of the laser system is provided below. We also specify the manufactures and the part numbers of most of the components.

A laser diode (QLD-960-100S, QPhotonics) with an the external cavity in the Littrow configuration [100] provided up to 35 mW of light at 960 nm. The diode was controlled by a commercial DLC-200 (MOGLabs) temperature and current controller. The laser frequency was tuned by tilting an optical grating provided with two piezo elements, a stack piezo that allowed a frequency change of several GHz, and a disk piezo for fast active stabilization of the laser frequency with the tuning range of 200 MHz. The diode laser was normally operated at 18 °C, and a current of 196 mA to generate blue photons resonant with the $5p_{3/2} \rightarrow 56s_{1/2}$ Rydberg transition. The home-made 960-laser was separated from the rest of the setup by two optical isolators with the total isolation of 59 dB to avoid possible optical feedback that might disturb the operation of the laser. A small part of the beam (< 1 mW) was sent to an optical wavelength meter (WA-1500, EXFO) that was used for a crude tuning of the 960-laser frequency close to a Rydberg transition. The accuracy of the wavemeter was 65 MHz at 960 nm, not sufficient for a fine frequency control of the laser used to excite a sub-MHz linewidth transition. The laser frequency slowly drifts due to thermal effects changing the length of the external cavity, and oscillates on a shorter time scale due to acoustic noise, changes of the air pressure at the cavity or other vibrational motion of the cavity. The stabilization of the laser frequency using absorption spectroscopy is discussed in Appendix C. Unfortunately, there are no simple methods to generate a narrow absorption signal at 480 or 960 nm. Absorption spectroscopy of rubidium Rydberg states in a glass vapor cell at 480 nm was reported [101] but required a significant amount of blue light power due to the low Rydberg excitation rate in a vapor. Also, a laser locked to a spectroscopic feature of an atomic resonance can not be

efficiently tuned far away from the resonance, while some the Rydberg blockade experiments might need to be performed a few GHz off the intermediate $5p_{3/2}$ state to avoid its population at the price of even lower Rydberg production rate. Instead, we used a transfer lock approach: the length of a Fabry-Perot resonator was fixed with respect to a frequency-stabilized laser, while the frequency of the home-made 960-laser was simultaneously locked to the resonator.

After the losses on the optical isolators and splitting of the diagnostics wavemeter beam, about 25 mW of power was injected into a tapered amplifier diode laser (a converted Tiger laser, Sacher Lasertechnik) with its gain curve centered around 960 nm. The amplifier was controlled by a commercial TEC3000 temperature and current controller (Sacher Lasertechnik). The amplifier output power of 650 mW in the seeded mode corresponded to gain factor of about 25 at the current of 1650 mA at 19.5 °C. The amplifier was separated from the rest of the setup in the forward direction by an optical isolator (32 dB). The output beam was shaped by a set of four lenses to match the fundamental mode of the double cavity. A small fraction of the 960-beam (< 10 mW) was split from the main beam and coupled to an optical fiber modulator (Lucent) to provide the frequency stabilization and tunability of the home-made laser. The fiber modulator, an electro-optical modulator integrated into a polarization maintaining fiber, was driven by a Fluke 6060 radio-frequency generator. The modulated output laser beam, characterized by a carrier optical frequency plus two first-order sidebands, was sent through an acousto-optical modulator. If P_0 is the total power in the beam, then the power in the carrier is $J_0^2(\beta_m)P_0$, and the power in each sideband is $J_1^2(\beta_m)P_0$, where β_m is the modulation depth. The first order output from the AOM was coupled to a home-made Fabry-Perot confocal resonator.

The resonator was formed by a 50-cm long invar cylinder holding two concave mirrors anti-reflection coated at 780 and 960 nm. The cavity had a free spectral range (FSR) of 150 MHz and a finesse of 25 at 780 nm and 783 at 960 nm. One of the cavity's mirrors was glued to a hollow cylindrical piezo-electric transducer

(PZT), which allowed us to change the length of the cavity. The light reflected from the input mirror was collected on a photodiode detector. When the frequency of the input light is an integer number times the cavity's free spectral range, constructive interference inside the cavity increases the transmitted power and decreases the reflected power. When the laser frequency or the cavity length are continuously scanned, the minima of reflected power are evenly spaced by the free spectral range in the frequency domain. As the laser beam carried the sidebands shifted in frequency from the unmodulated zero order, the destructive interference condition for the sideband occurred at a cavity length different from that of the carrier. An example of the transmitted cavity signal, where the carrier was separated from the two sidebands by the modulation frequency, f_{mod}, and repeated every FSR, is shown in Fig. 6.4 (top). Assuming the cavity length is stable, the laser can be locked to this signal: the change in laser frequency near the cavity resonance would produce a change in the reflected signal power thus establishing the correspondence between the laser frequency and the voltage produced by the photodiode detector. The voltage is fed back to the laser to stabilize its frequency similar to locking a laser to a saturated absorption setup as discussed in Appendix C. The detected power might change not only due to the change of the laser frequency but because of the power fluctuation of the laser itself. It is therefore, advantageous to lock the laser on top of the resonance signal, where reflected power has its maximum value when the laser is resonant with the cavity. Since the resonance peak is symmetric, both positive and negative changes of the laser frequency from resonance will result in the same decrease of the photodiode signal, which can not be used to change the laser frequency back to resonance through a feedback loop. However, a first derivative of the cavity peak, as shown on the bottom scan in Fig. 6.4, is asymmetric about resonance: positive and negative frequency shifts give rise to either increase or decrease of the derivative signal.

Practically, there are several ways to generate the derivative, or error signal, from the cavity resonances, and feed the error signal back to the laser to achieve

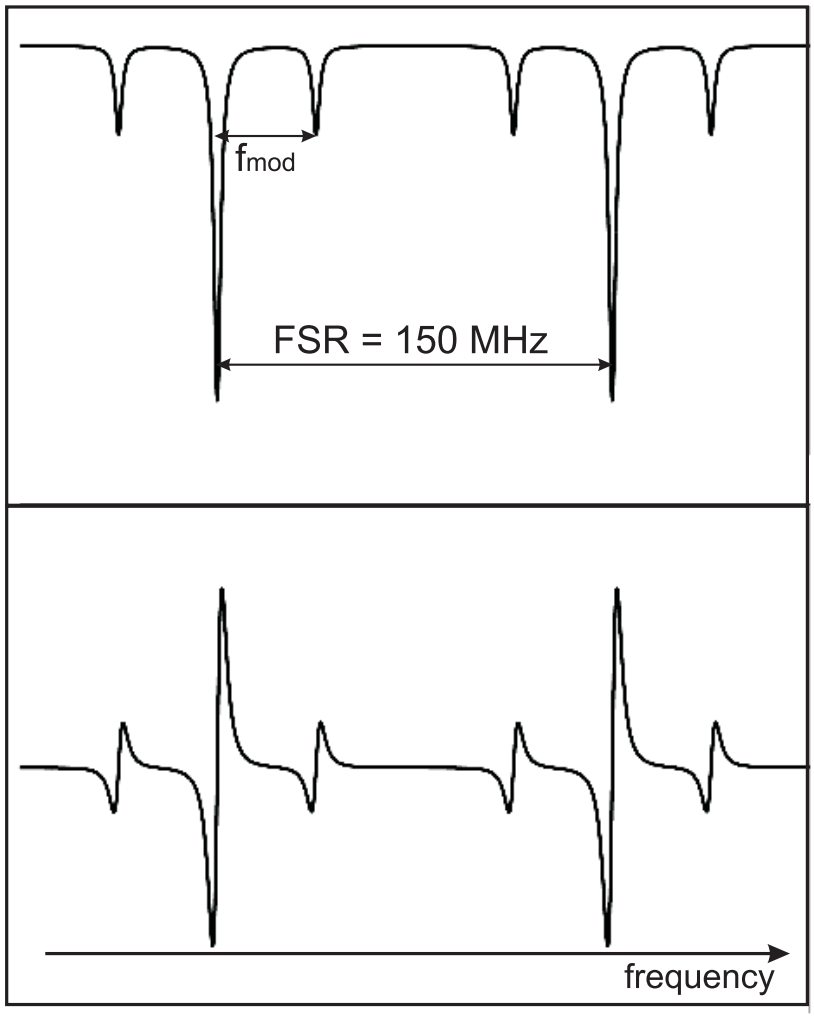

Figure 6.4: Top frame: cavity resonances of the Fabry-Perot resonator measured by a photodiode. The 960-laser beam coupled with the cavity was amplitude modulated by a fiber-modulator. The main carrier and two sidebands at the modulation frequency are separated from the next set of resonances by a free spectral range of the cavity. The corresponding derivative is shown on the bottom. The error signal was generated by a frequency modulation of each cavity resonance.

its frequency stabilization. All approaches are based on the Pound-Driver-Hall stabilization technique [102]. If the laser frequency (or amplitude) is modulated and above resonance, the reflected signal is amplitude modulated and in phase

with the frequency variation. Below resonance, the derivative is negative, and the reflected intensity varies 180° out of phase with respect to the input. Therefore, the frequency modulation allows us to distinguish between the two sides of the cavity resonance. We first consider the application of the Pound-Driver-Hall technique to stabilize the length of our Fabry-Perot cavity to a frequency stabilized laser, and then show how the stabilized cavity was used to lock the frequency of the 960-laser.

6.2.1 Stabilization of Fabry-Perot Resonator

The diode laser at 780 nm, used for the laser cooling in the cold atom apparatus, was frequency-stabilized by locking it to a rubidium saturated absorption spectroscopy signal, a part of the existing BEC apparatus. A part of the beam (< 3 mW) was coupled to a polarization maintaining fiber and delivered to the blue light optical table. The linearly polarized output from the fiber was mode-matched with the Fabry-Perot resonator as shown in Fig. 6.5.

The polarization of the beam was rotated to maximize its reflection from a polarizing beam splitter cube, and the reflected beam was sent through a standard double-pass AOM configuration. After the splitter, the beam passed through another AOM, the first diffraction order was coupled to the resonator cavity, and the reflected power was measured by a photodiode detector (PDA110, Thorlabs) with a bandwidth of 1.5 MHz. The signal was similar to that presented on the top of Fig. 6.4, but without the sideband (smaller) peaks. To realize the Pound-Driver-Hall technique, we modulated the central frequency of the second AOM by a local oscillator running at about 800 kHz, such that the sidebands were close to the carrier. The modulated photodiode signal was compared with the signal from a local oscillator with a RF-mixer. The mixer, analogous to a lock-in amplifier, multiplied the input signals to produce the output with the sum and the difference of the input frequency components, *e.g.,* the DC component and twice the modulation frequency component. The DC (frequency difference) component

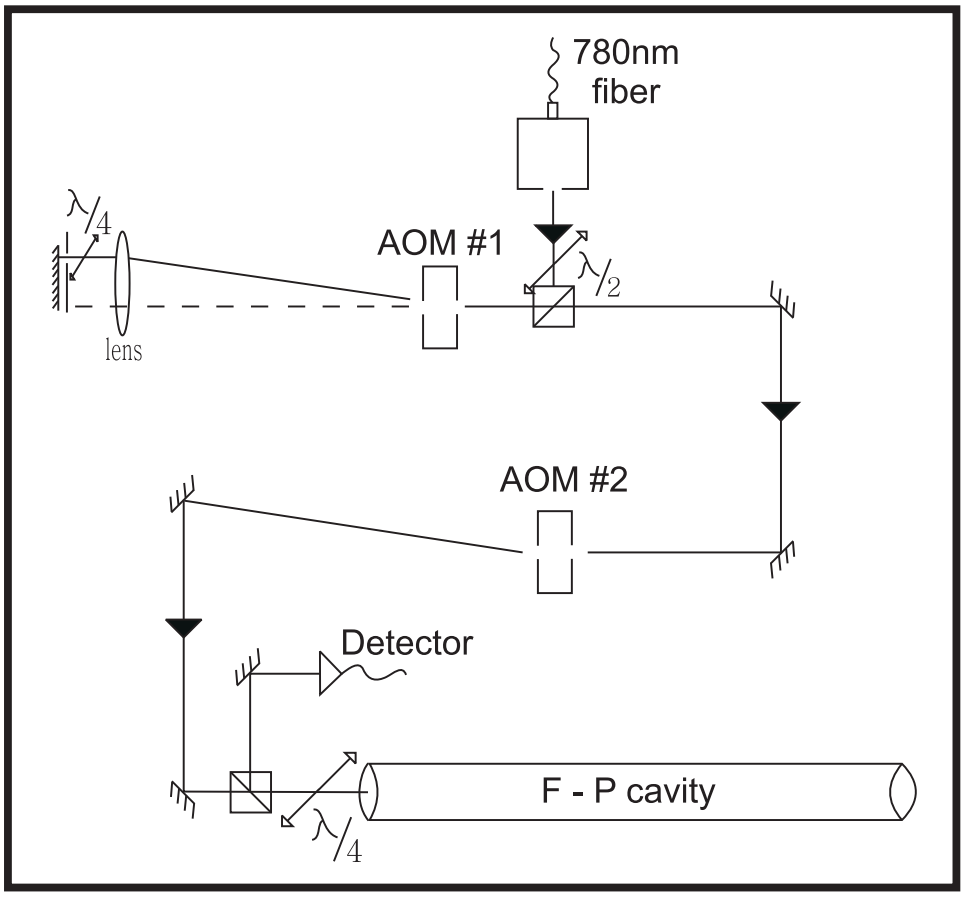

Figure 6.5: Optical layout for stabilization of the Fabry-Perot resonator. Frequency of the 780-nm laser beam from a frequency-stabilized diode laser is shifted by a double-pass AOM #1, fm-modulated by an AOM #2, and coupled with the Fabry-Perot cavity. The reflected power is measured by a fast photodiode detector.

is proportional to the derivative of the unmodulated reflected intensity. A typical output from the mixer, after the high frequency components were attenuated by a low-pass filter, is shown on the bottom part of Fig. 6.4. Thus the Pound-Driver-Hall technique provides an asymmetric error signal, suitable for a servo-lock system. The error signal is closed to a linear ramp around the resonant frequency, and standard tools of control theory [103] can be applied to correct for the laser frequency fluctuations.

The length of the resonator was controlled by an output of a high-voltage am-

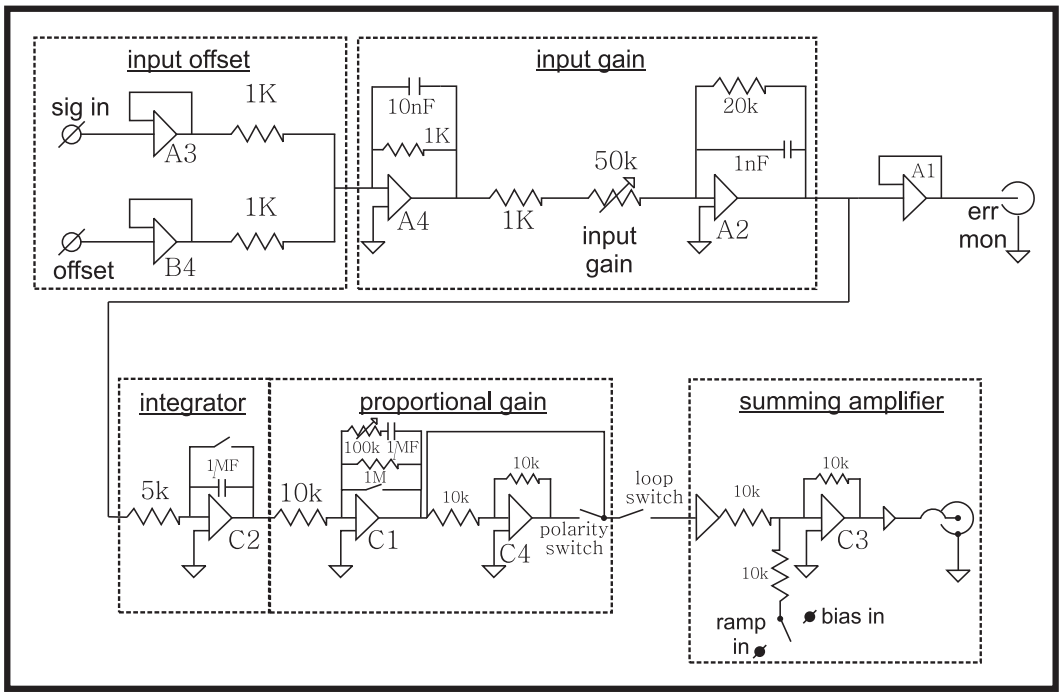

Figure 6.6: Schematics of the Fabry-Perot cavity locking circuit. The input error signal is offset, integrated, amplified, summed with the bias and ramp voltages, and fed back to control the length of the cavity.

plifier (PZD350, TREK, 250 kHz bandwidth) applied to the PZT attached to one of the cavity mirrors. The voltage was generated by an electronic circuit, whose diagram is shown in Fig. 6.6. The error signal from the rf mixer was offset and amplified by the input gain such that the middle point of the error signal slope (cavity resonance) corresponded to zero volts. The resulting signal was integrated, further amplified with a proportional gain and the voltage's polarity was inverted, if necessary, to provide negative feedback. The result was combined with an externally generated ramp and bias voltages, and sent to the high-voltage amplifier. The ramp voltage from a function generator provided a continuous scan of the cavity length around the bias voltage, similar to that Fig. 6.4. To lock the cavity length to the frequency-stabilized 780-laser, the ramp voltage was turned off, the bias voltage adjusted to set the cavity length resonant with the wavelength of light, and the

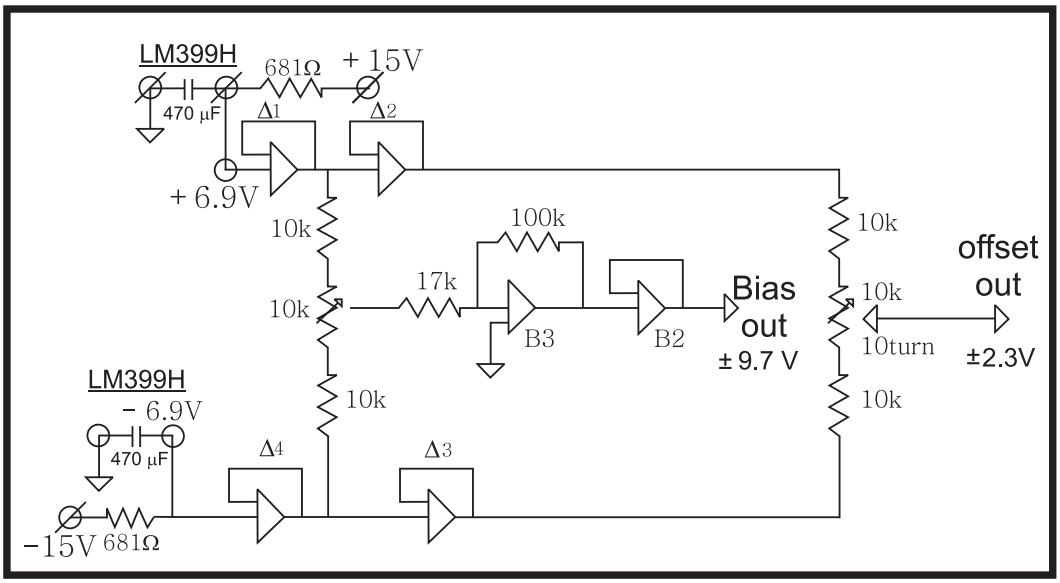

Figure 6.7: The bias and offset voltages for the servo loops generated by a LM399H precision reference.

feedback loop was closed to keep the resonator's length fixed with the respect to the wavelength of light. The offset and the bias voltages were generated according to a circuit diagram presented in Fig. 6.7. The servo's bandwidth of a kilohertz was limited by mechanical response of the cavity mirror. That was high enough to compensate for a thermal drift of the cavity length and vibrations induced by the acoustic noise, and low enough not to transfer a possible high-frequency noise from the 780-laser to the 960-laser that was locked to the stabilized Fabry-Perot cavity.

As the cavity length was stabilized, it was possible to change its length continuously without unlocking the feedback loop. For that purpose, the central frequency of the double-pass AOM #2 in Fig. 6.5 was slowly tuned, thus changing the frequency of light injected into the resonator. The servo responded accordingly controlling the cavity length to keep the laser resonant with the wavelength of light. The tuning range of 35 MHz was limited by the bandwidth of the AOM.

6.2.2 Stabilization of Laser Light at 960 nm

To stabilize the frequency, achieve a narrow linewidth, and tunability of the 960-laser, we locked the laser to the stabilized Fabry-Perot cavity. The intensity of laser light was modulated by the fiber modulator, passed through an AOM, its first diffraction order coupled with the resonator cavity, and the cavity resonances measured by a photodiode detector as shown in Fig. 6.3. The central frequency of the AOM was frequency modulated at 300 kHz by a local oscillator to generate an error signal using the Pound-Drever-Hall technique as described in the previous subsection. The cavity resonances and the corresponding error signal for each resonance dip is presented in Fig. 6.4. The error signal was fed back to the controller of the home-made laser to keep its wavelength resonant with the length of the resonator. The schematic of the employed servo loop is shown in Fig. 6.8.

The error signal was amplified, offset and the resulting signal was divided between two independent servo loops. The frequency of the diode laser could be controlled by a voltage applied to a PZT disk to change the length of the laser's external cavity, or by changing the current driving the laser diode. The piezo could be used to tune the laser frequency over a range of 0.5 GHz, but the bandwidth of such control is quite slow, below 1.5 kHz, limited by the mechanical motion of the optical grating. The current control can be fast, with a bandwidth of several MHz when the current is supplied directly to the diode; however, adjusting the current allows only a small tuning of the laser frequency, about 50 MHz in our case, before the laser hops to a different mode as the laser cavity length depends on the properties of the diode semiconductor that are very sensitive to the driving current[3]. We used the piezo voltage to control slow changes in the laser wavelength, while current can be used to control fast changes of the laser frequency. For this purpose, a low-pass filter with a cut-off frequency of $2\pi \times 200$ Hz allowed only low-

[3]In addition to that, significant changes of current result in large changes of the laser output power.

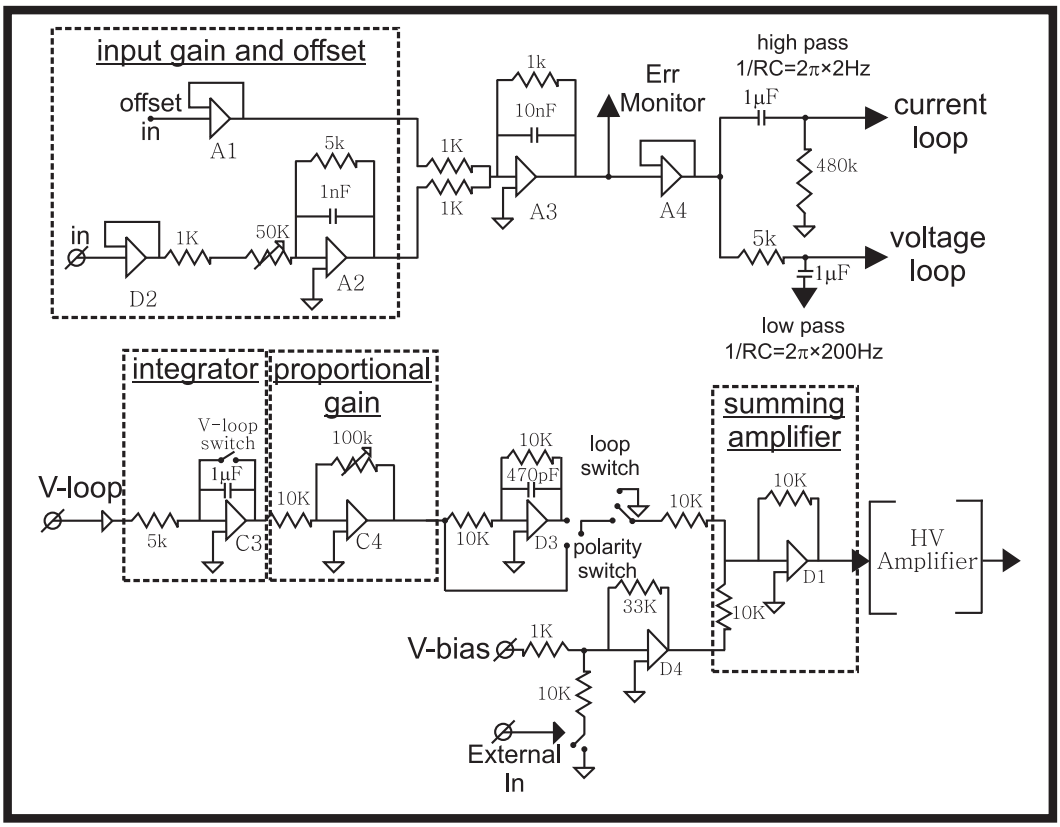

Figure 6.8: Schematics of the 960-laser locking circuit. The input error signal is amplified, offset, its DC component processed by a servo loop controlling the piezo of the 960-laser.

frequency components of the error signal to pass to the voltage loop, and high-pass filter with the cut-off frequency of $2\pi \times 2$ Hz blocked the DC-component of the signal from the current servo loop.

The voltage loop acted as an integrator of the near-DC components of the error signal; after the integration, the error signal was summed with the bias voltage. The resulting voltage was sent to the laser's piezo through a high voltage amplifier. The closed voltage servo loop provided the frequency stabilization compensating for possible long-term thermal drifts and low-frequency vibrations.

The AC-part of the error signal passed through the current loop presented in Fig. 6.9. The output voltage, a sum of the integrated and proportionally gain

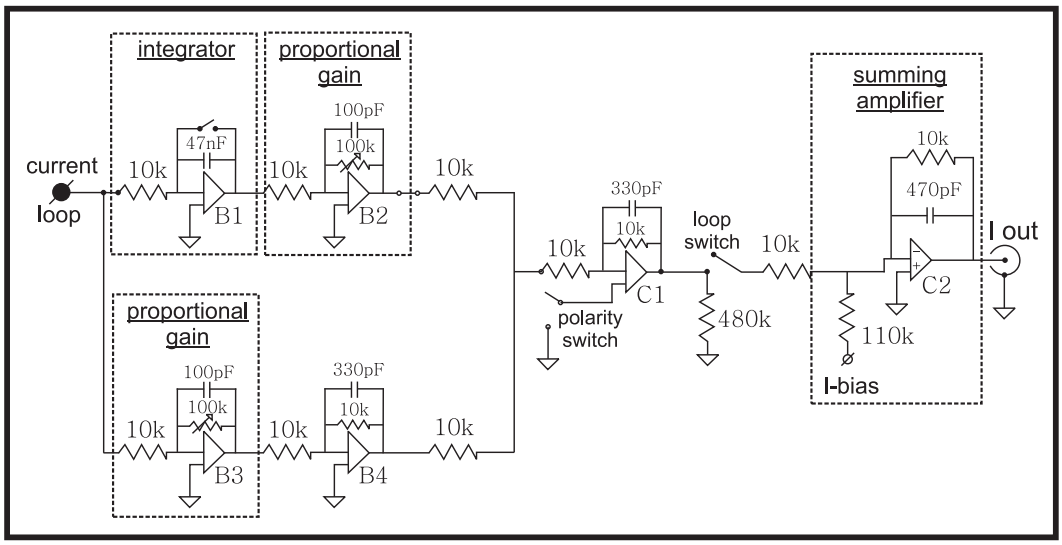

Figure 6.9: Schematics of the 960-laser current loop locking circuit. The AC-component of the error signal, generated by the circuit in Fig. 6.8, is split, integrated and amplified. The resulted voltage controls the current of the diode laser.

input signal, was sent to the diode laser current controller. The bandwidth of the current loop was limited by the bandwidth of the current controller of 10 kHz. Closing the voltage and the current loop consecutively provided the desired frequency stabilization of the 960-laser light.

We used one of the first-order sidebands produced by the fiber-modulator as the cavity resonance for locking. The sideband had a frequency $f = f_L + f_{mod}$, where f_L is the frequency of the laser, and f_{mod} is the modulation frequency of the EOM. If the modulation frequency is changed, the servo loops will change the laser frequency accordingly, such that the sum of the two, f, is resonant with the cavity. This way the laser frequency could be tuned continuously while the laser stayed locked over a range much larger than that provided by a double-pass AOM. The maximum possible tuning range can be limited by the bandwidth of the EOM, the range of frequencies generated by the local oscillator, or the mode-hop-free range of the diode laser, whichever is smaller. We were constrained by the local

oscillator, Fluke 6060, with the maximum output frequency of 500 MHz at 13 dBm of power. The free spectral range of the cavity of 150 MHz was another constraint. Intentional misalignment of the input beam with respect to the input coupler of the fiber modulator allowed us to suppress the transmission of the zeroth order through the fiber while preserving the power of the first-order sidebands at a higher modulation depth. In this case, the scan over the cavity resonances looked similar to that in Fig. 6.4 with the carrier frequency resonances much smaller than the side-band ones, and the two sets were separated by the free spectral range of the cavity. If we ignore the zeroth order features, and start increasing the modulation frequency, the first order from the left set of resonances and the negative first order from the right set will move toward each other, and the corresponding error signal will no longer be a linear ramp as the features get closer than their width. This break of the error signal profile occurs at "singularity points", where the modulation frequency is a multiple of 75 MHz, half of the free spectral range of the cavity. The width of the error signal was smaller than 1 MHz, and we changed the modulation frequency in steps of 1 MHz with the laser locked: apparently, the change of the modulation frequency of the function generator was slow enough for the servo loop to follow. The laser was still locked at the "singularity points", but as the modulation frequency was further increased the locking point might "jump" to another resonance from the other set. Practically, we needed to pass the "singularity points" several times back and forth until the laser happened to stay locked to the same sideband before and after the "singularity points". This approach allowed us to scan the 960-laser frequency over the range of 250 MHz (and 500 MHz for the frequency-doubled blue light), with the exception of the 3 MHz regions around the "singularity points", where the laser frequency was undetermined.

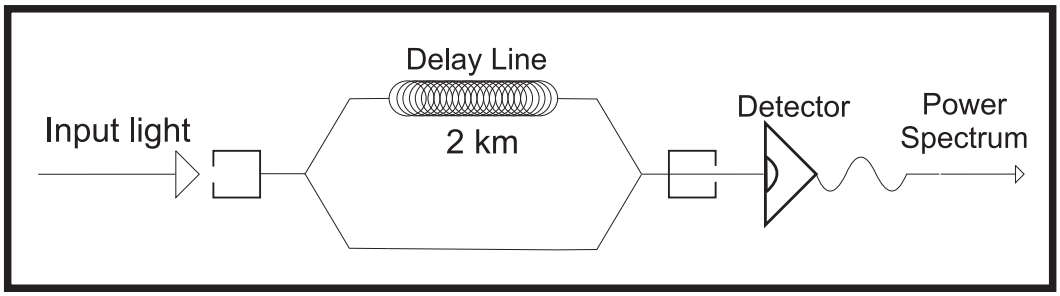

Figure 6.10: A linewidth of a laser is measured by the self-homodyne measurement technique. Frequency fluctuations of the laser are converted to variations of intensity in a Mach-Zander type interferometer. The optical fiber delay line provides uncorrelated mixture of optical fields at the detector.

6.2.3 Laser Linewidth Measurement

The excitation rate of a very narrow Rydberg transition might be limited by the linewidth of the excitation laser. We measured the linewidth of our diode laser by a self-homodyne measurement technique [104]. The optical phase or frequency fluctuations of a laser, resulting in the broadening of the Schawlow-Townes fundamental linewidth, can be converted into variations of light intensity in a unequal-arm Mach-Zehnder interferometer. In the interferometer, one arm is extended by an optical fiber, the mixture of two optical fields is measured by a fast photodiode, and the power spectrum of the photodiode current fluctuations provides the information about the laser linewidth. We used fiber splitters to divide and recombine optical fields as shown in Fig. 6.10. A 2-km optical fiber provided a delay of $\tau_0 \sim 6.7\ \mu s$ in one of the arms. The mixed power was detected by a photodiode with the bandwidth of 20 MHz, and the photocurrent spectral distribution detected by a power spectrum analyzer (E4440A, Agilient) over 4.6 ms sweep time. The setup was applied to characterize two lasers that provided the Rydberg excitations: the 780-nm Toptica and the tampered amplifier when seeded by the 960-nm home-made diode laser. The power spectra are presented in Fig. 6.11 on a logarithmic scale for the frequency-stabilized Toptica laser (graph 1), free-running

960-laser (graph 2), and the 960-laser locked to the Fabry-Perot cavity of the stabilized length (graph 3). When the delay line time, τ_0 is much larger than the laser coherence time (inverse linewidth), the interfering optical fields are uncorrelated at the detector, and the power spectrum of the photocurrent is strictly Lorentzian with a width twice the FWHM of the laser spectrum. That was the case for the recorded Toptica spectrum, where a reliable Lorentzian fit gave a linewidth value of about 1.5 MHz, with the corresponding coherence time $\tau_c = 0.67\ \mu s << \tau_0$. When the delay time is comparable or shorter than the laser coherence time, the phase dynamics of the interfering optical fields remains partially correlated, and the corresponding photocurrent power spectrum deviates from the Lorentzian profile. The power spectrum for the case of a free-running 960-laser is shown in the middle graph in Fig. 6.11, and could not be fitted solely by a Lorentzian. The Lorentzian fit with the FWHM of 750 kHz corresponded to 375 kHz of the laser linewidth, or to the coherence time of 2.7 μs, still smaller than $\tau_0 = 6.7\ \mu s$. When the 960-laser was frequency-stabilized to the Fabry-Perot resonator, the appropriate power spectrum revealed an oscillating pattern superimposed on the Lorentzian line with the period of oscillations given by $1/\tau_0$, which was an indication that the coherence time became comparable or larger than the delay time, and the laser linewidth was smaller than $1/\tau_0 = 150$ kHz. In this case, our self-homodyne measurement setup can not be used to extract the exact value of the laser linewidth as the beat signal critically depends on the length difference between the two optical paths on the wavelength scale, and an extension of the delay line or a modification of the setup was required to perform an accurate measurement, for example, as described in reference [105]. We did not pursue such measurements further, as we were satisfied with the results: the 780-laser linewidth was measured to be 1.5 MHz, much larger than the estimated linewidth of the 960-laser of about 150 kHz, or 300 kHz of the blue light at 480 nm after the frequency-doubling. As both lasers were employed for an excitation of Rydberg levels, the effective linewidth of the excitation light was limited by that of the 780-laser, and the precise measurement of the 960-laser

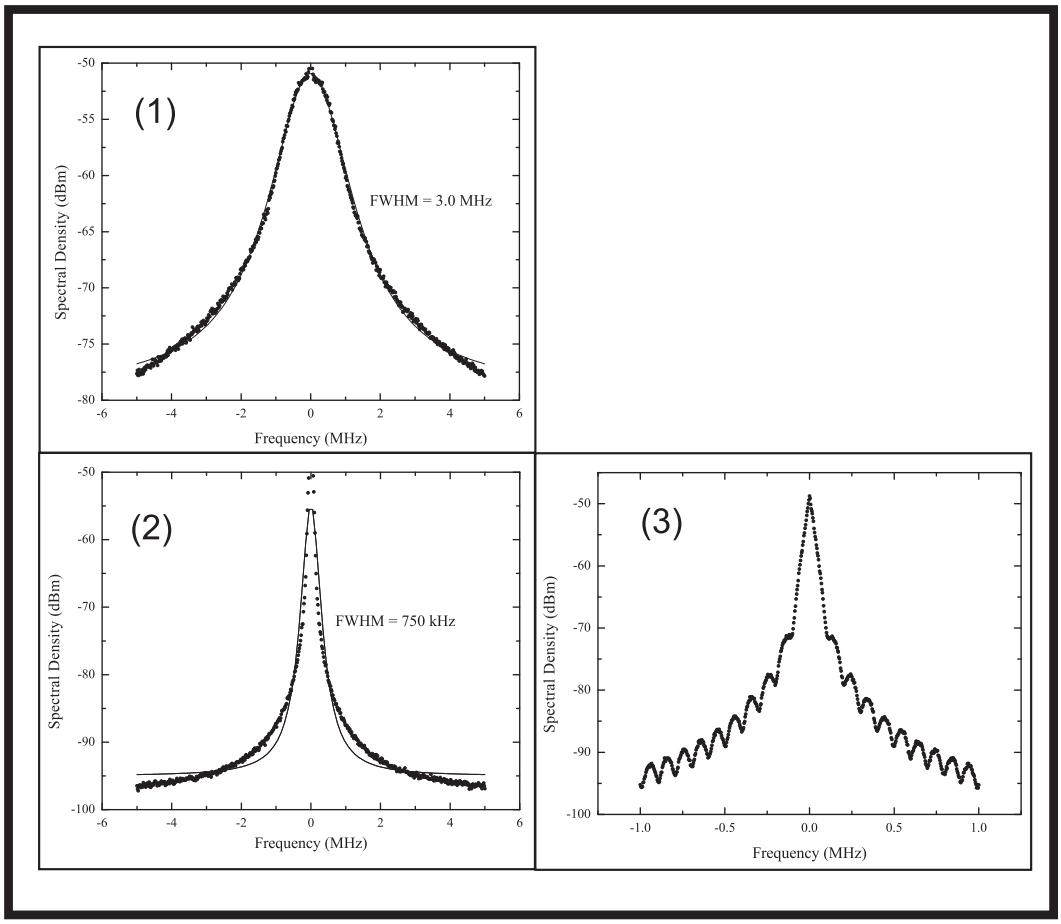

Figure 6.11: Power spectra measured with the self-homodyne technique for the frequency-stabilized Toptica (graph 1), the free-running home-made 960-laser (graph 2), and the 960-laser locked to the Fabry-Perot resonator (graph 3). The spectrum is strictly Lorentzian for Toptica when the delay line is longer than the coherence length of the laser. For a longer coherence length the spectrum deviates from Lorentzian (graph 2) and exhibits oscillations when the coherence length is longer then the delay line (graph 3).

linewidth was not found necessary. A better stabilization of the Toptica laser to reduce its linewidth was not available at the time.

6.2.4 Frequency-doubling of 960-nm Light

The stabilized and tunable light at 960 nm was converted into the 480-nm light by a second harmonic generation (SHG) process in a Lithium Triborate (LBO) nonlinear crystal in a commercial, external-cavity frequency doubler (WaveTrain, Newport). The generation of the second harmonic of a continuous wave laser requires significant input fundamental power, not available experimentally. The amplification of the optical power can be achieved in an optical build-up cavity, and the conversion efficiency from a nonlinear crystal can be increased in comparison with a direct conversion arrangement [106]. The resonator cavity schematics utilized in the WaveTrain is shown in Fig. 6.12. A ring cavity is formed by two curved dielectric mirrors and a prism. The length of the resonator is tuned by translating the prism along its symmetry axis via the piezoelectric transducer PZT. Both the prism P and the nonlinear crystal X are cut for Brewster's incidence angle to minimize reflection losses that limit the gain of the resonator. The 960-laser beam was shaped by a cylindrical lens L1, and spherical lenses L2, L3 and L4 (Fig. 6.3) to match the fundamental eigenmode of the cavity. The pump beam passed through an EOM, that modulated the frequency of the beam at 80 MHz. A reflection from the input cavity mirror M1 was measured by a photodiode. The resulting cavity resonances and the corresponding Pound-Drever-Hall error signal are shown in Fig. 6.13. The FWHM of the resonances was about 6 MHz. A servo loop controlling the piezo voltage provided the locking of the cavity on resonance with the wavelength of the pump beam to ensure the maximum build-up of power inside the resonator. Curved cavity mirrors focused the fundamental resonator mode on the LBO crystal. The critical phase matching, an equality of phase velocities of the fundamental and harmonic modes, was achieved through the angular dependence of the refractive indices of the crystal. The doubler cavity converted 300 mW of 960-nm light into a 30 mW of blue light at 480 nm. The elliptical profile of the output blue beam was corrected to a round one by two cylindrical lenses

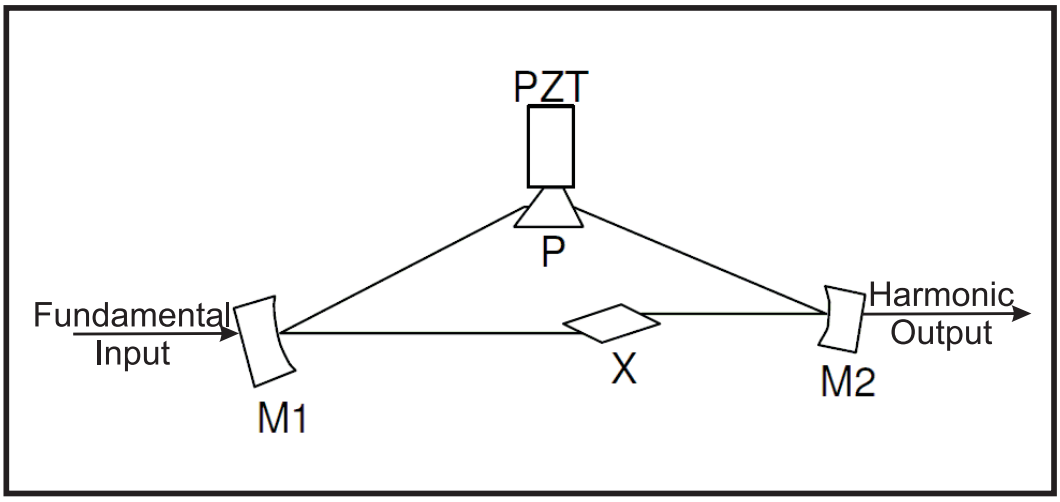

Figure 6.12: Two curved mirrors M1 and M2, and a prism P form a power build-up cavity for a second harmonic generation in a LBO crystal X. The cavity length is controlled by a transverse motion of the prism attached to a PZT. The prism and the crystal are at Brewster's angle to minimize the cavity loss.

L5 and L6. The beam passed through an AOM for amplitude control. The first diffraction order was coupled with a polarization maintaining fiber and delivered to the optical table hosting the cold atom apparatus. The central frequency of the AOM was computer-controlled, and the modulator was used as a beam deflector to provide a fast switching time of the blue beam. Routinely, 6.5 mW of power of the 1.6 mm diameter laser beam at 960 nm was delivered to a cold atomic cloud for the Rydberg excitation experiments.

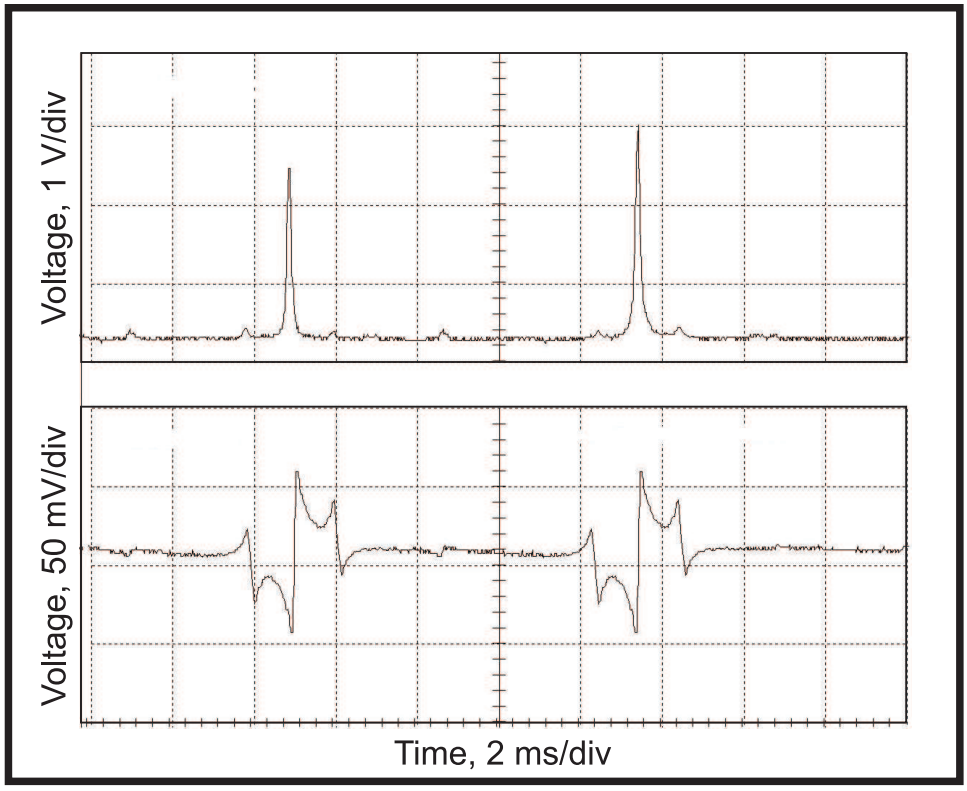

Figure 6.13: An oscilloscope screen shot of the cavity resonances of the WaveTrain doubler and the corresponding error signal. The FWHM of the resonance is about 6 MHz (one division corresponds to $\sim$ 110 MHz on a 2-ms time scale).

Chapter 7

First Experiments with Rydberg Atoms

As discussed in Chapter 5, the strength of the Rydberg-Rydberg interactions can be dramatically increased in the presence of an external electric field. The produced DC Stark effect can be used to either shift the atomic energy levels to Förster resonances or mix the energy levels to create a field-independent permanent dipole moment. In both cases, the application of the electric field results in the transition from $1/R^6$ van der Waals to $1/R^3$ dipole-dipole interactions, where R is the interatomic separation. For the $50s$ state and $R = 5\ \mu m$ the energy shift is about 1 MHz due to the van der Waals interaction and up to 150 MHz for the dipole-dipole interaction at an external field of 5 V/cm. Required density of 4 μm^{-3} is an order of magnitude higher than the peak densities of a standard MOT setup, but can be achieved in a tight magnetic trap after the some evaporative cooling. A broadening of the Rydberg transition resonance from the energy shift due to interactions can be observed with spectroscopic measurements. The first spectroscopic measurements obtained with our excitation laser system are reported in this Chapter.

7.1 Autler-Townes Splitting

The linewidth of our two-photon excitation laser system, described in Chapter 6, was measured to be about 1.5 MHz. Our first step to test the excitation system was to investigate the Rydberg production in a MOT cloud. In this set of experiments,

the MOT cooling laser, red-detuned from the $5s_{3/2}$ level, was used to provide the first excitation photons at 780 nm. I will refer to this laser as the pump. The laser intensity was above saturation of the cooling transition resulting in the strong pumping of the $5s_{3/2}$ state. The laser detuning from the atomic resonance, δ, was variable for different experiments. The second, 480-nm photon was delivered with a collimated 1.6 mm diameter laser beam (probe) of 6.5 mW of power. The frequency of the probe beam was tuned to provide the two-photon resonance between the ground $5s_{1/2}$ and the $56s_{1/2}$ excited state. The choice of the particular excitation level was not critical for the initial test of the system. To align the probe with the atomic cloud we overlapped the beam with an auxiliary near-resonant 780-beam that could destroy the trapped cloud when aligned with it. Thus, the proper alignment of the auxiliary beam guaranteed the alignment of the blue beam.

We have conducted the spectroscopic measurements in the following way. The MOT cloud was collected at the cooling laser detuning $\delta/2\pi = -24$ MHz. We used a relatively small cloud of 10^7 atoms with the diameter of 0.5 mm, smaller than the size of the blue beam. Then, the slower beam was shut off to stop the MOT loading and the atoms were exposed to the blue light for a time $t_b = 50$ ms, much shorter than the trap lifetime due to the background gas collisions. As atoms are excited to a Rydberg state, they can be ionized by the blackbody radiation and are no longer trapped. Therefore, a net trap loss due to the excitation is proportional to the number of excited Rydberg atoms. After the exposure, the number of atoms in the ground state was measured by absorption imaging technique, which destroyed the trapped cloud concluding the measurement cycle. During consecutive cycles, loading - exposure - imaging, the frequency of the probe was incremented in steps of 2 MHz. The relative trap loss, the number of atoms lost from the trap divided by the initial number of atoms in the trap, around two-photon resonance along with a two-peak Lorentzian fit is presented in Fig. 7.1 as a function of the probe frequency.

The spectrum, an Autler-Townes doublet [107], features two resonances at fre-

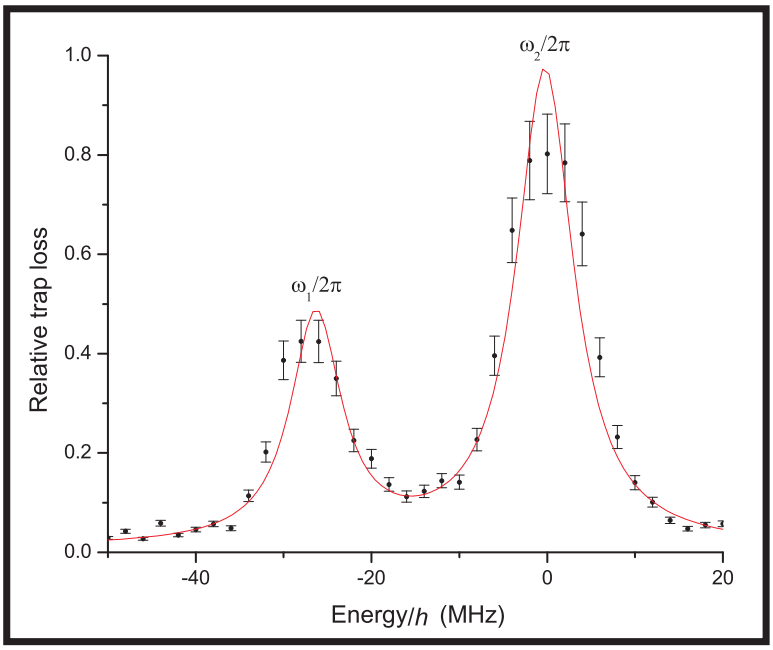

Figure 7.1: Autler-Townes splitting of $5p_{3/2}$ as probed by transition to $56s$ state. The separation between resonances is the generalized Rabi frequency of the saturated pump transition.

quencies $\omega_1/2\pi$ and $\omega_2/2\pi$. The Autler-Townes splitting resulting from a dipole transition between an unperturbed state and a pair of dressed states is considered in Appendix D. Not taking into account the width of resonances, the relative position of the two resonances can be found from the normalized spectral distribution function

$$F(\omega) = cos^2\Theta \;\; f(\omega_b - \Delta) + sin^2\Theta \;\; f(\omega_b - \Delta + \tilde{\Omega}), \tag{7.1}$$

where ω_b is frequency of the blue light, Ω is the Rabi frequency of the $5s_{3/2} \rightarrow 5p_{3/2}$ transition, the generalized Rabi frequency $\tilde{\Omega} = \sqrt{\delta^2 + \Omega^2}$, the dynamic Stark shift $2\Delta = \tilde{\Omega} + \delta$, $tan(2\Theta) = -\Omega/\delta$, δ is the detuning from the intermediate state, and $f(\omega)$ is the Dirac's delta-function[1]. The spectral distribution function sets the relative position and height of the two resonances. The spacing between resonances

[1]We use an unconventional notation for the delta-function to distinguish it from the detuning δ.

in Fig. 7.1 is $\omega_2 - \omega_1 = \tilde{\Omega}$, which allows an accurate measurement of the 780-nm Rabi frequency once the detuning δ is known. The actual spectrum in Fig. 7.1 consists of two power-broadened Lorentzian peaks with the separation between the two of $\tilde{\Omega}/2\pi = 27$ MHz as extracted from a data fit with a sum of two Lorentzian profiles.

At small detunings δ, the Rydberg excitation is step-wise as atoms are pumped to the intermediate level and spend a finite amount of time, eventually to either get excited to the Rydberg state or radiatively decay to the ground state. In this case, the width of the Lorentzian resonances, w is dominated by the saturation of the pump transition, such that $w \sim \gamma\sqrt{1+s} > 6$ MHz, where $\gamma = 6$ MHz is the natural linewidth of the cooling transition and s is the saturation parameter. For large detunings, $\delta/2\pi\gamma >> 1$ the Rydberg transition occurs through a virtual state, as atoms are pumped to the Rydberg state directly through a two-photon transition. The width of resonance is set by the convolution of the Rydberg state decay rate and the linewidth of the excitation laser. For our experimental setup, the 1.5 MHz width was limited by the resolution of the 780-laser. To ensure that there were no other broadening mechanisms present, we investigated the Autler-Townes spectra for various MOT detunings for the excitation time of 10 ms. Experiments were conducted under the same conditions as before for a set of detunings δ between 16 and 56 MHz provided by a double-pass AOM. The maximum possible detuning was limited by the bandwidth of the AOM: the power transmitted through the double pass, and therefore the corresponding Rabi frequency, was just enough to provide a detectable Rydberg excitation. The spectra for each detuning are presented in figures 7.2-7.10. Each data point represents a single measurement of the trap loss. We ascribed the vertical error bar to the data point based on 10-20% variation of the MOT atom number from one loading cycle to another.

At larger detunings the dressing interaction is weaker, so that $\Theta \approx 0$, and the spectrum reduces to a single line at the frequency of the probe light, ω_b. For $\delta > 26$ MHz, the smaller peak corresponding to the stepwise excitation is comparable with

the background level making the fitting procedure with the sum of two Lorentzian functions dependent on the initial parameters of the fit. Therefore, we fitted the experimental data around the taller, two-photon excitation peak with a single Lorentzian function. For each data set, we chose a subset to fit around the peak, limited to several data points on the lower energy side of the peak to avoid possible contribution from the other, smaller peak. We ensured that the fit results did not depend on a particular choice of the subset within the uncertainty of the fit results. That was not true for higher detunings, $\delta > 32$ MHz, where the width of the peak of a few megahertzs was close to the scan step of 2 MHz, and only a few data points represented the peak complicating the fitting procedure. For figures 7.6-7.10, we show a specific subset of data that provided a converging fit resulted in a peak height between the maximum value of the data (within the corresponding error bar) and one, the maximum possible value of the trap loss. The corresponding fits are shown in solid lines in each figure along with a distribution of the normalized residuals (bottom plots). The uncertainties of the fit results were increased as necessary to make the results independent of the data subset. The fit results, values of the peak widths, their respective uncertainties, and the reduced χ^2_{red} values are reported in captions of each figure.

The width of the taller, two-photon resonance peak as a function of the detuning is presented in Fig. 7.11. We see that the width drops from about 6 MHz at the standard MOT detunings to about 1.5 MHz at larger detunings, which is consistent with the value of the linewidth of our excitation laser. At higher values of the detuning, the fits are quite poor resulting in large values of uncertainties and reduced $\chi^2_{red} \sim 10$. Nevertheless, we were satisfied with the results as no broadening above the value of the excitation laser linewidth was observed. As an example, the solid line in Fig. 7.11 shows the power broadening due to detuning of a 100 kHz resonance of the two-level atom that models Rydberg excitations at large detunings from the intermediate state.

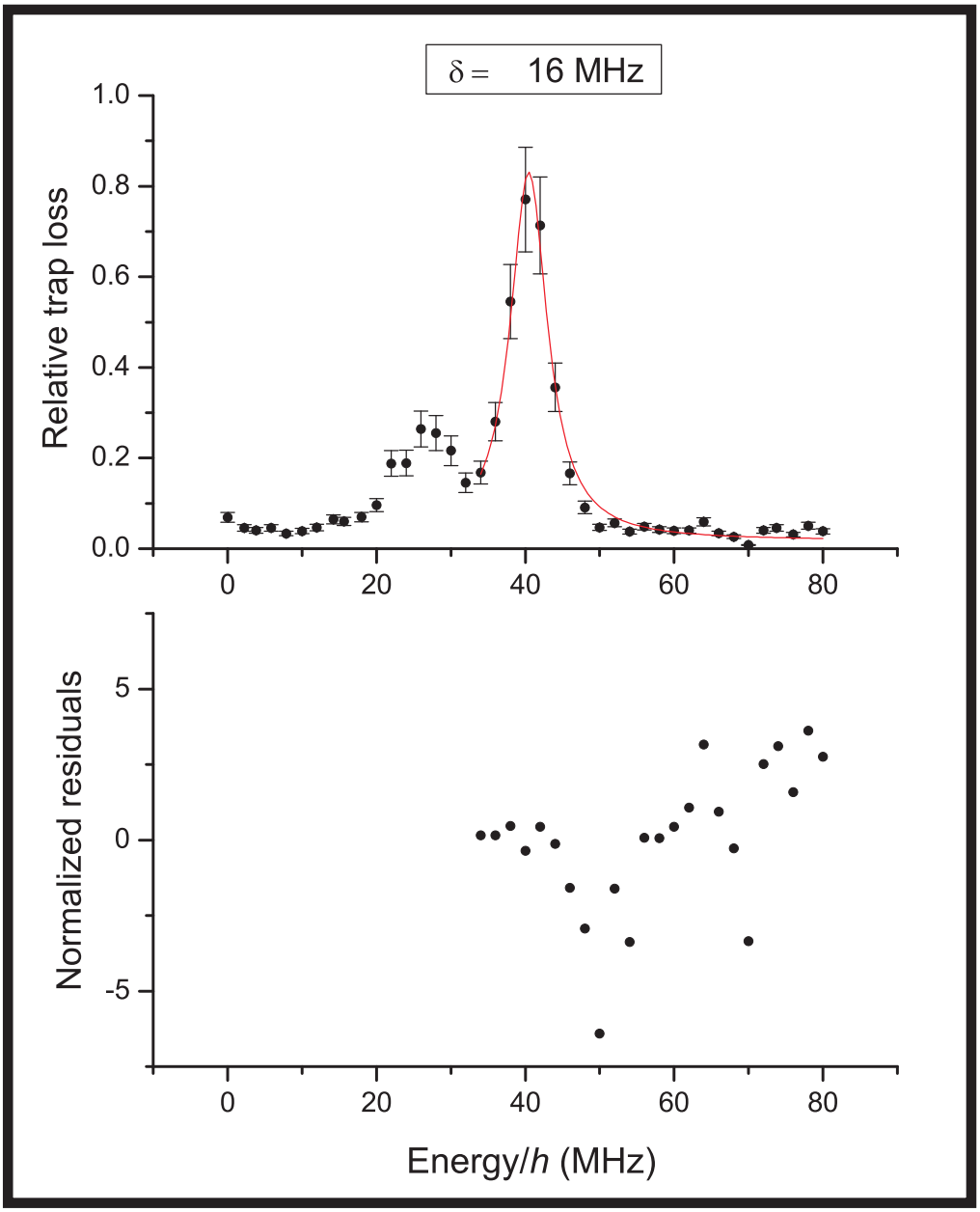

Figure 7.2: Autler-Townes splitting for the MOT detuning of 16 MHz (top) and the Lorentzian fit of the two-photon transition peak with the width, $w_c = (6.06 \pm 0.31)$ MHz. The normalized residuals of the fit are shown on the bottom plot. The corresponding reduced χ^2_{red} =2.42.

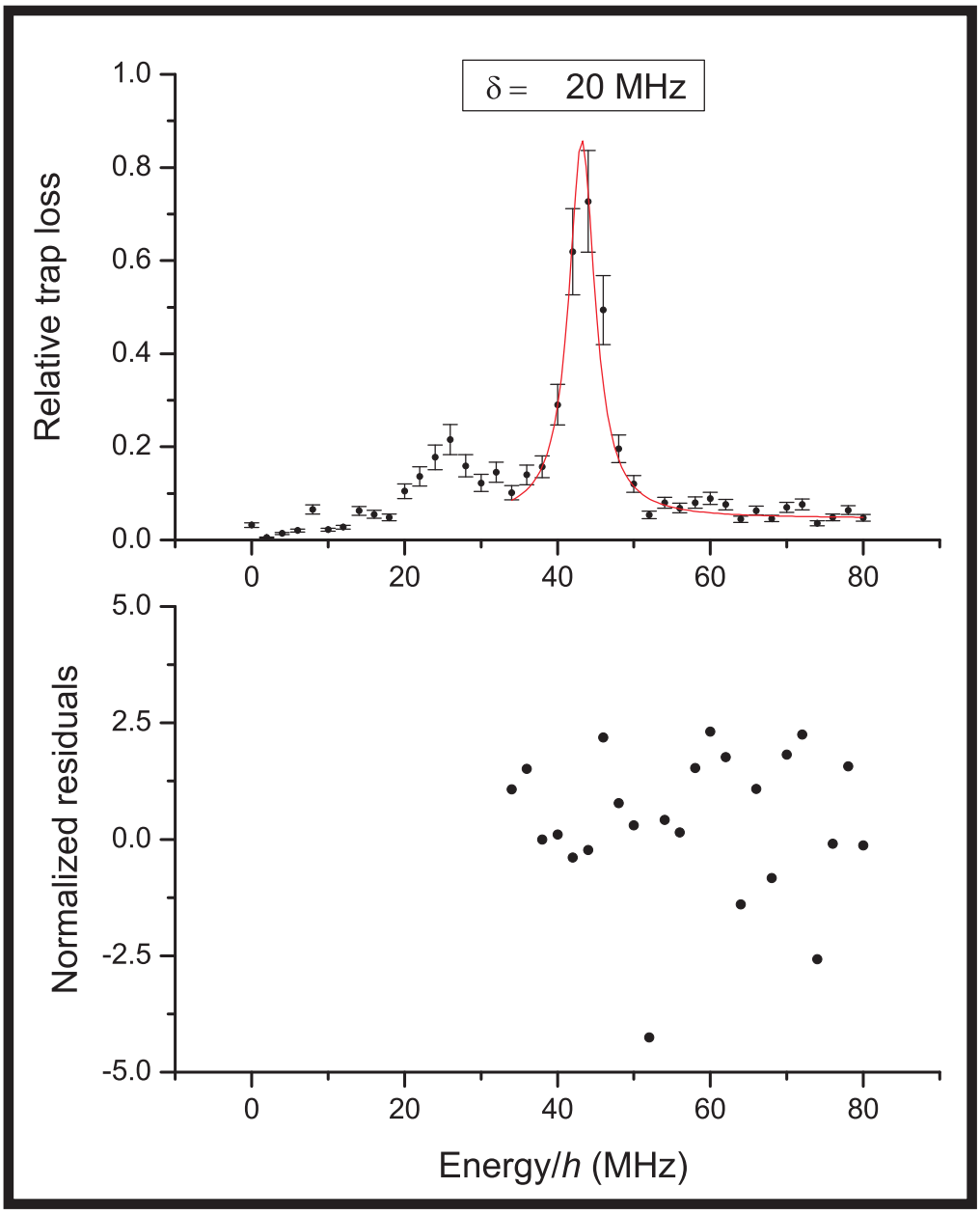

Figure 7.3: Autler-Townes splitting for the MOT detuning of 20 MHz (top) and the Lorentzian fit of the two-photon transition peak with the width, $w_c = (4.13 \pm 0.77)$ MHz. The normalized residuals of the fit are shown on the bottom plot. The corresponding reduced χ^2_{red} =2.98.

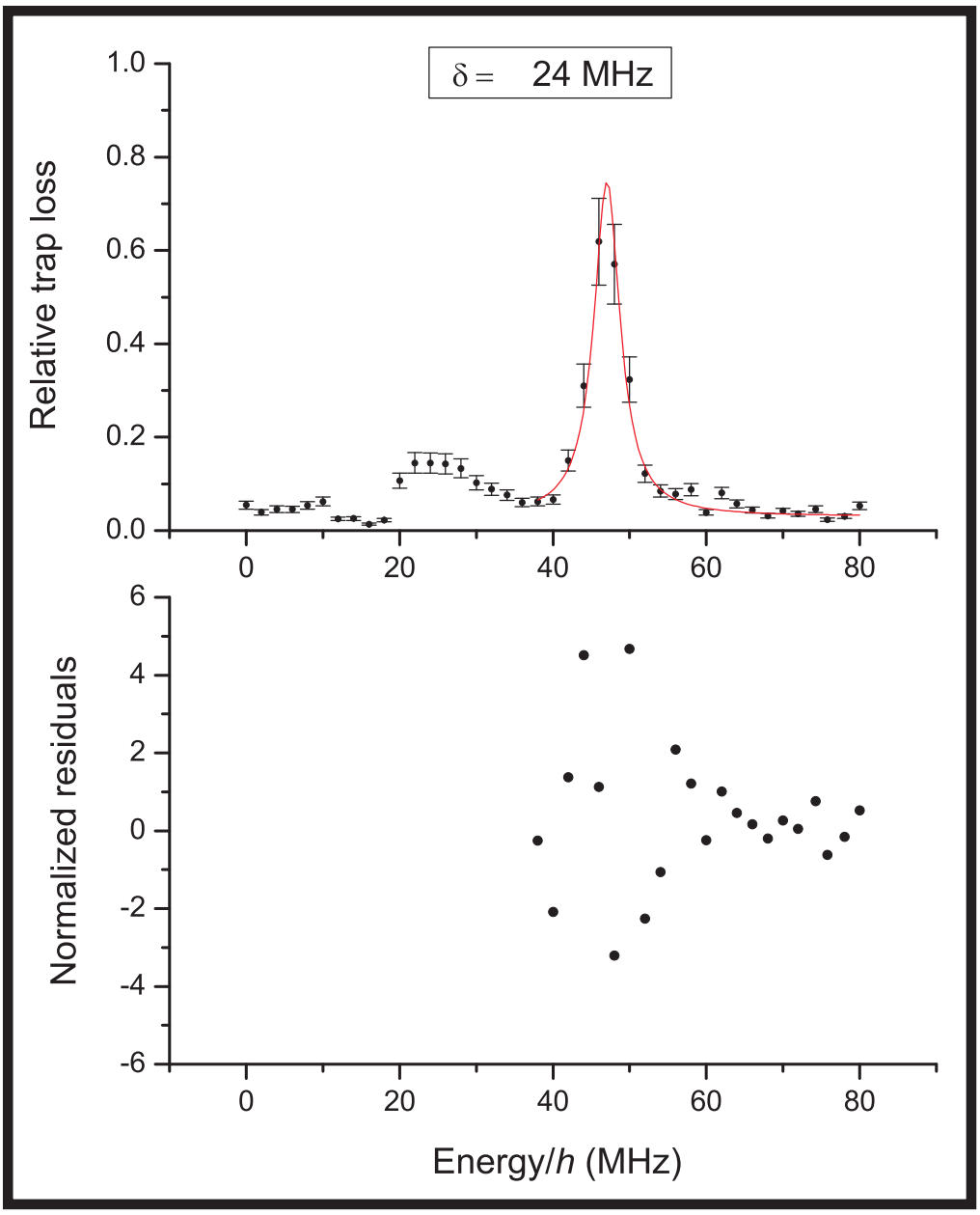

Figure 7.4: Autler-Townes splitting for the MOT detuning of 24 MHz (top) and the Lorentzian fit of the two-photon transition peak with the width, $w_c = (4.14 \pm 0.71)$ MHz. The normalized residuals of the fit are shown on the bottom plot. The corresponding reduced χ^2_{red} =2.89.

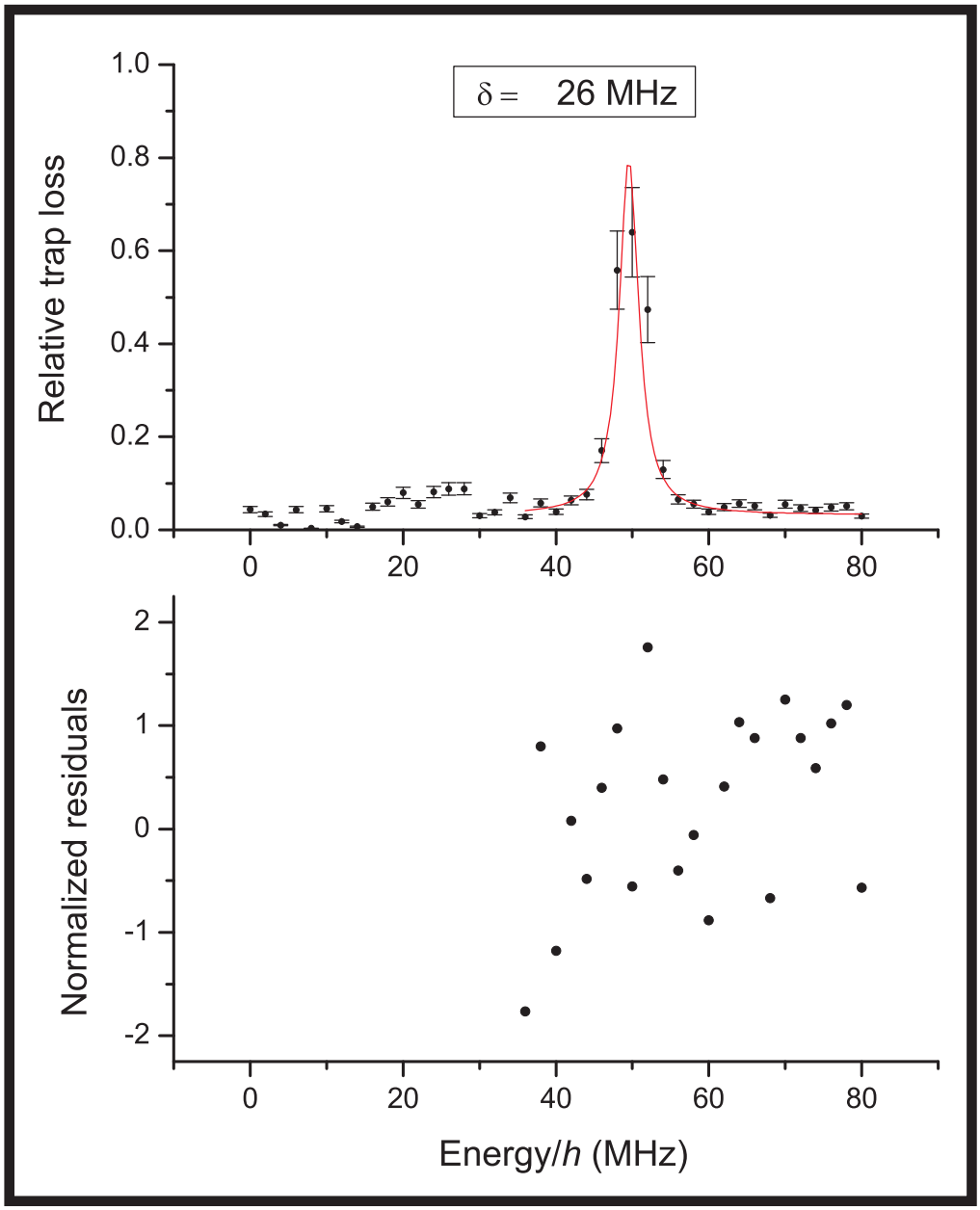

Figure 7.5: Autler-Townes splitting for the MOT detuning of 26 MHz (top) and the Lorentzian fit of the two-photon transition peak with the width, $w_c = (3.05 \pm 0.63)$ MHz. The normalized residuals of the fit are shown on the bottom plot. The corresponding reduced χ^2_{red} =3.32.

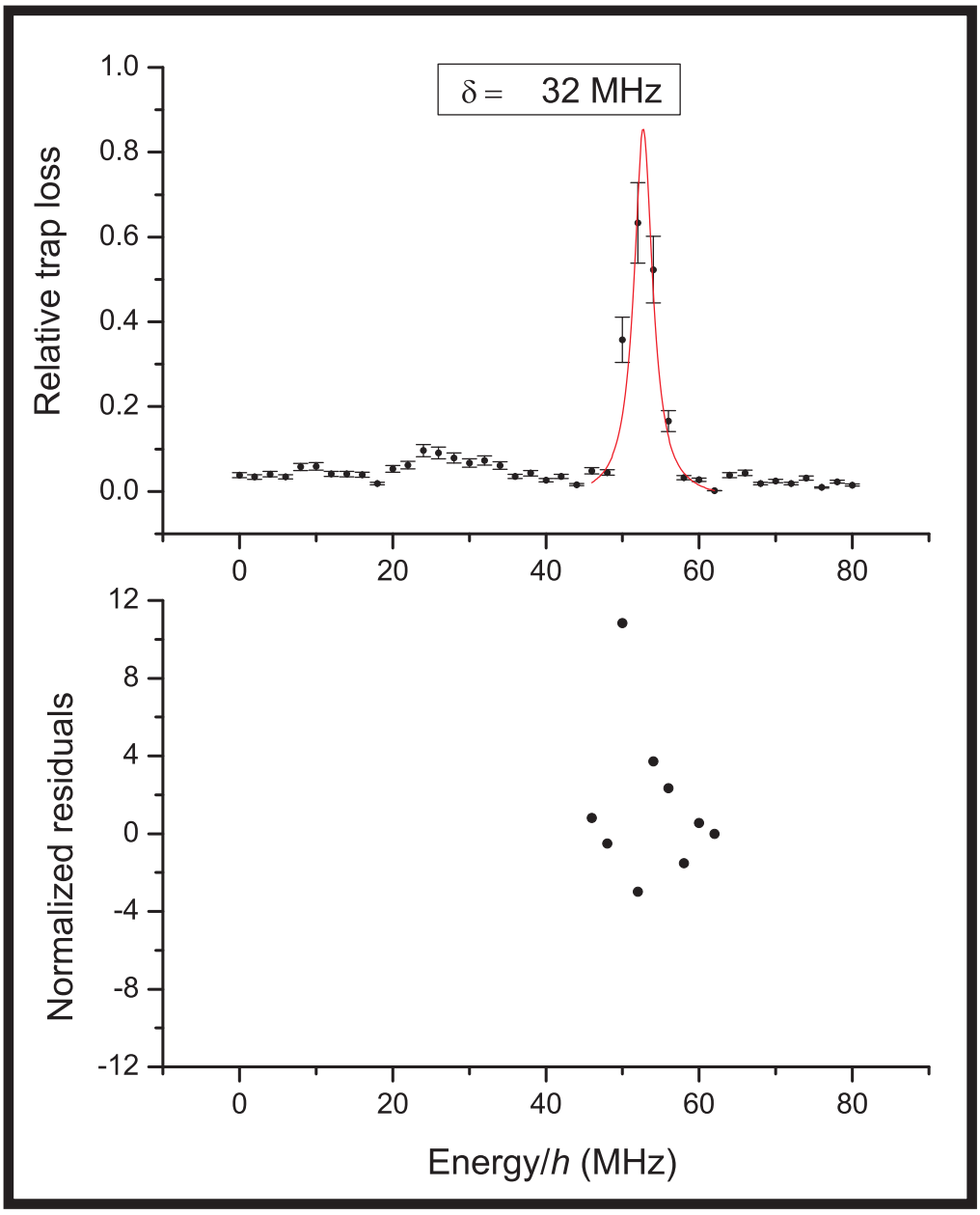

Figure 7.6: Autler-Townes splitting for the MOT detuning of 32 MHz (top) and the Lorentzian fit of the two-photon transition peak with the width, $w_c = (2.97 \pm 1.26)$ MHz. The normalized residuals of the fit are shown on the bottom plot. The corresponding reduced χ^2_{red} =9.38.

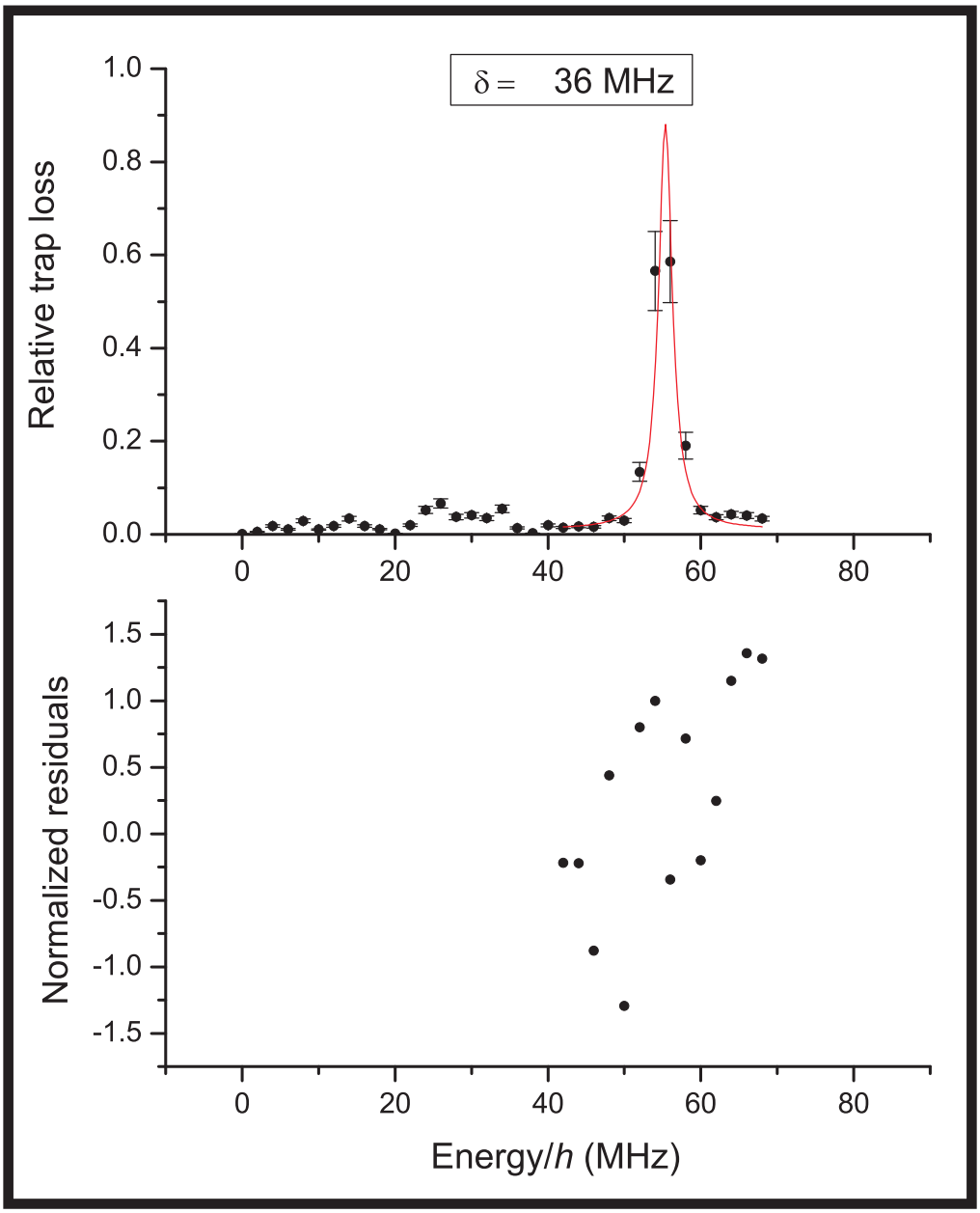

Figure 7.7: Autler-Townes splitting for the MOT detuning of 36 MHz (top) and the Lorentzian fit of the two-photon transition peak with the width, $w_c = (2.18 \pm 0.82)$ MHz. The normalized residuals of the fit are shown on the bottom plot. The corresponding reduced χ^2_{red} =6.63.

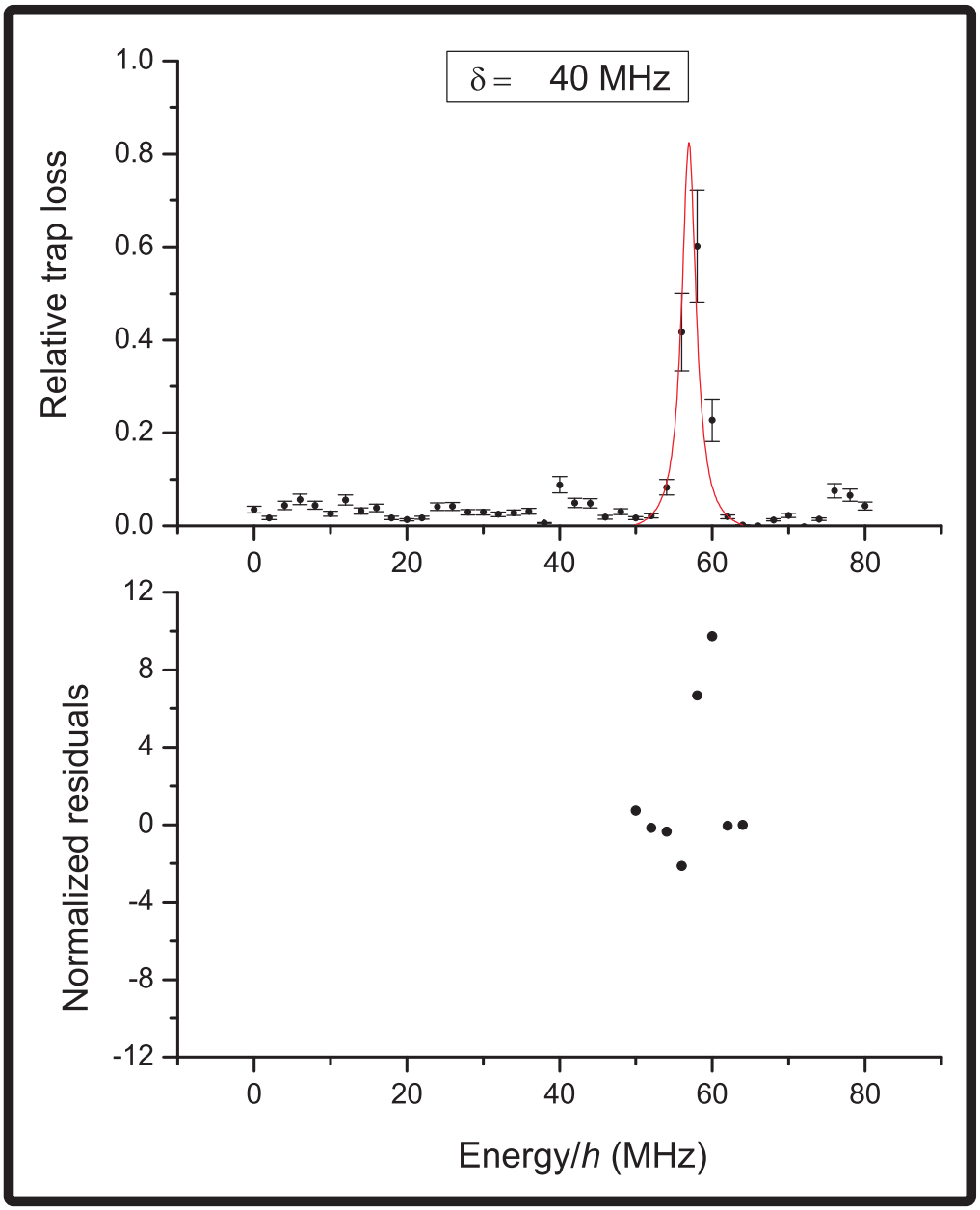

Figure 7.8: Autler-Townes splitting for the MOT detuning of 40 MHz (top) and the Lorentzian fit of the two-photon transition peak with the width, $w_c = (2.29 \pm 1.17)$ MHz. The normalized residuals of the fit are shown on the bottom plot. The corresponding reduced χ^2_{red} =7.89.

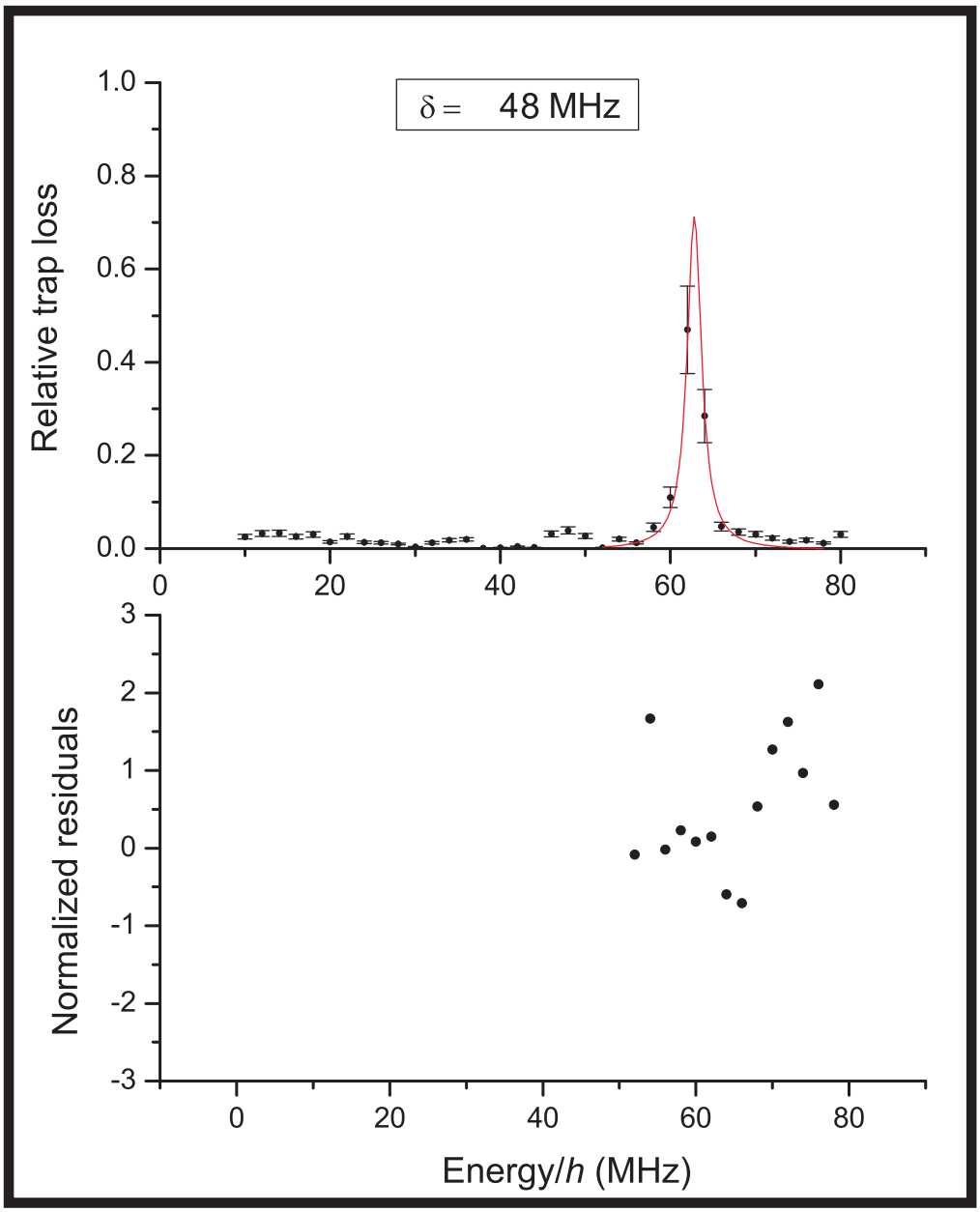

Figure 7.9: Autler-Townes splitting for the MOT detuning of 48 MHz (top) and the Lorentzian fit of the two-photon transition peak with the width, $w_c = (2.06 \pm 1.39)$ MHz. The normalized residuals of the fit are shown on the bottom plot. The corresponding reduced χ^2_{red} =12.1.

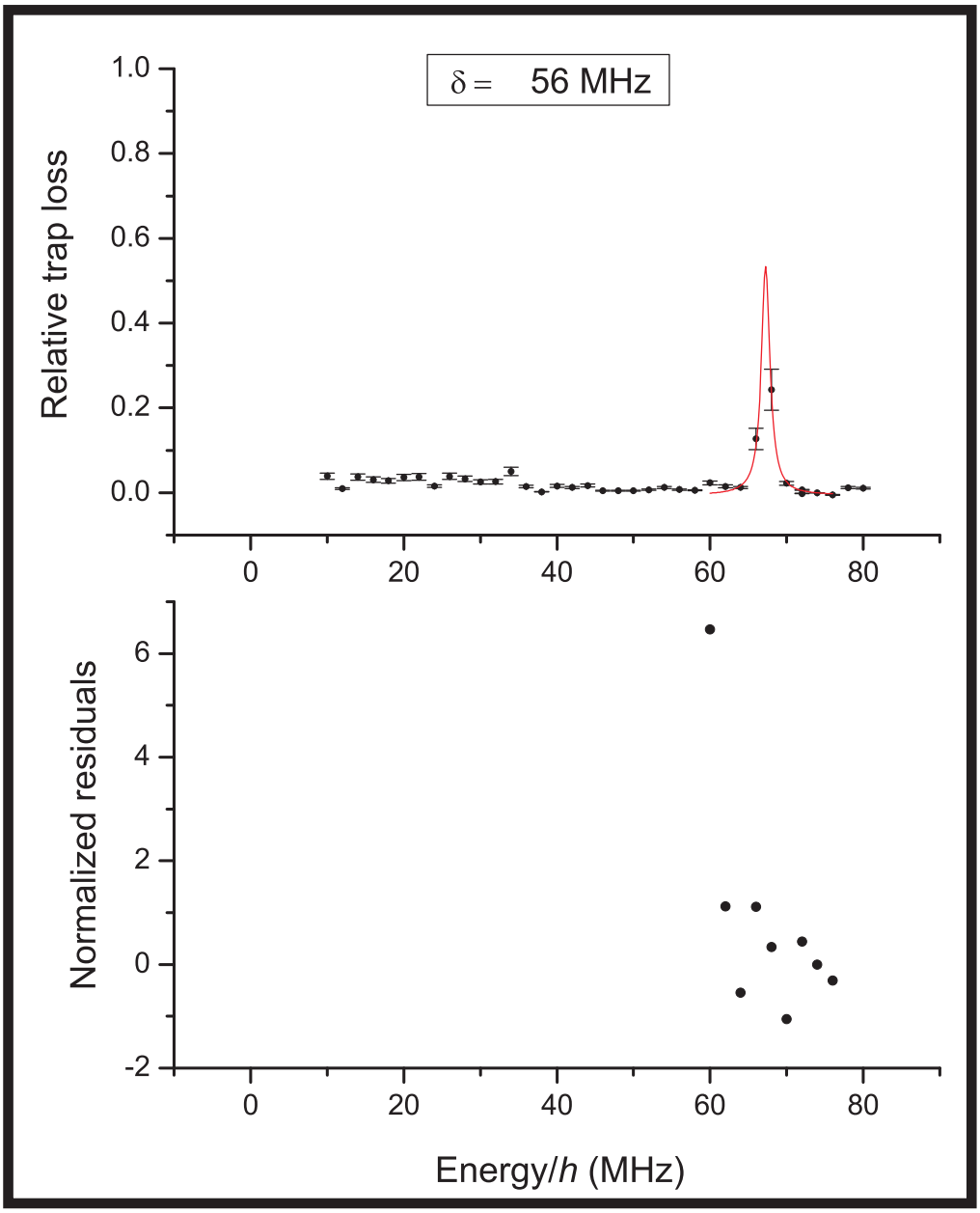

Figure 7.10: Autler-Townes splitting for the MOT detuning of 56 MHz (top) and the Lorentzian fit of the two-photon transition peak with the width, $w_c = (1.35 \pm 1.30)$ MHz. The normalized residuals of the fit are shown on the bottom plot. The corresponding reduced χ^2_{red} =10.9.

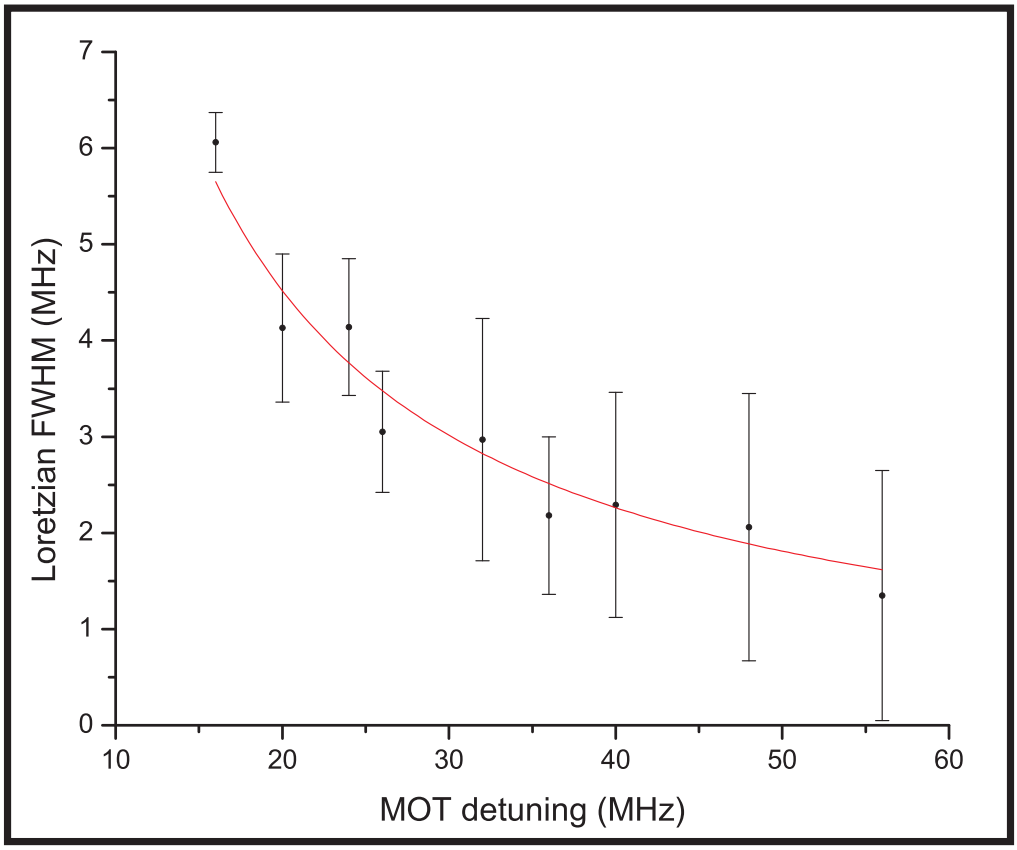

Figure 7.11: The width of the two-photon resonance peak of the Autler-Townes splitting for various MOT detunings. The error bars represent the uncertainties of the corresponding Lorentzian fits of the resonances. The solid line is an example of power broadening of a 100 kHz resonance.

7.1.1 Rydberg Production Rate Measurement

Strong Rydberg-Rydberg interactions can result in a broadening of the two-photon resonance. Another signature of the strong interactions is the reduction of the Rydberg production rate at a fixed detuning from the intermediate level. It is useful to be able to measure the production rate with the possibility of its further investigation under conditions of suppressed excitations.

At large detunings, the population of the intermediate level can be adiabatically eliminated, and three-level atom system can be considered as effective two-level

system. The population dynamics of a two-level system with the ionization decay is considered in Appendix D. The $56s$ Rydberg state radiatively decays to the ground state with the rate $1/\tau_{nl}^0 = 1/170\,\mu s$ and gets ionized by blackbody radiation with the rate $1/\tau_{bb} = 1/150\,\mu s$. The trap loss is given by the number of ionized atoms, N_i, and for the case of close radiative and ionization rates $1/\tau_{nl}^0 \sim 1/\tau_{bb} = \gamma$, can be written as

$$N_i = N_0 \left(-\frac{\gamma}{\gamma + R_R}\, e^{-(\gamma+R_R)t} + e^{-\gamma t} - \frac{R_R}{\gamma + R_R} \right), \tag{7.2}$$

where N_0 is the initial trap number and R_R is the Rydberg production rate.

We experimentally measured the number of atoms lost from the trap as a function of the excitation time at a fixed detuning $\delta = 36$ MHz, and the probe frequency tuned to the two-photon resonance. The trap loss data is presented in Fig. 7.12 (top), and was fitted with the rate Eq. 7.2 to obtain the Rydberg production rate $R_R = 1/(2.62 \pm 0.16)$ ms with the reduced χ^2_{red} of 0.25. Each data point represents a single measurement of the atom number left in the trap after the excitation. We ascribed the vertical error bar to the data point based on the 10% variation of the MOT atom number from one loading cycle to another. The normalized residuals for the fit are shown on the bottom plot of Fig. 7.12.

7.2 Rydberg Atoms in External Electric Field

As discussed in Chapter 5, the application of an external constant electric field allows us to dramatically enhance the Rydberg-Rydberg interactions. At low fields, the atom's induced dipole moment interacts with the field resulting in the Stark energy shift quadratic in field for an s state. At higher fields of about 5-6 V/cm, the atom in $n \sim 50$ state obtains a permanent dipole moment independent of the field due to the opposite parity level mixing. In this work we investigated the effect of the low fields. In particular, we measured the energy shift due to the field and observed a resonance broadening that can be an indication of the

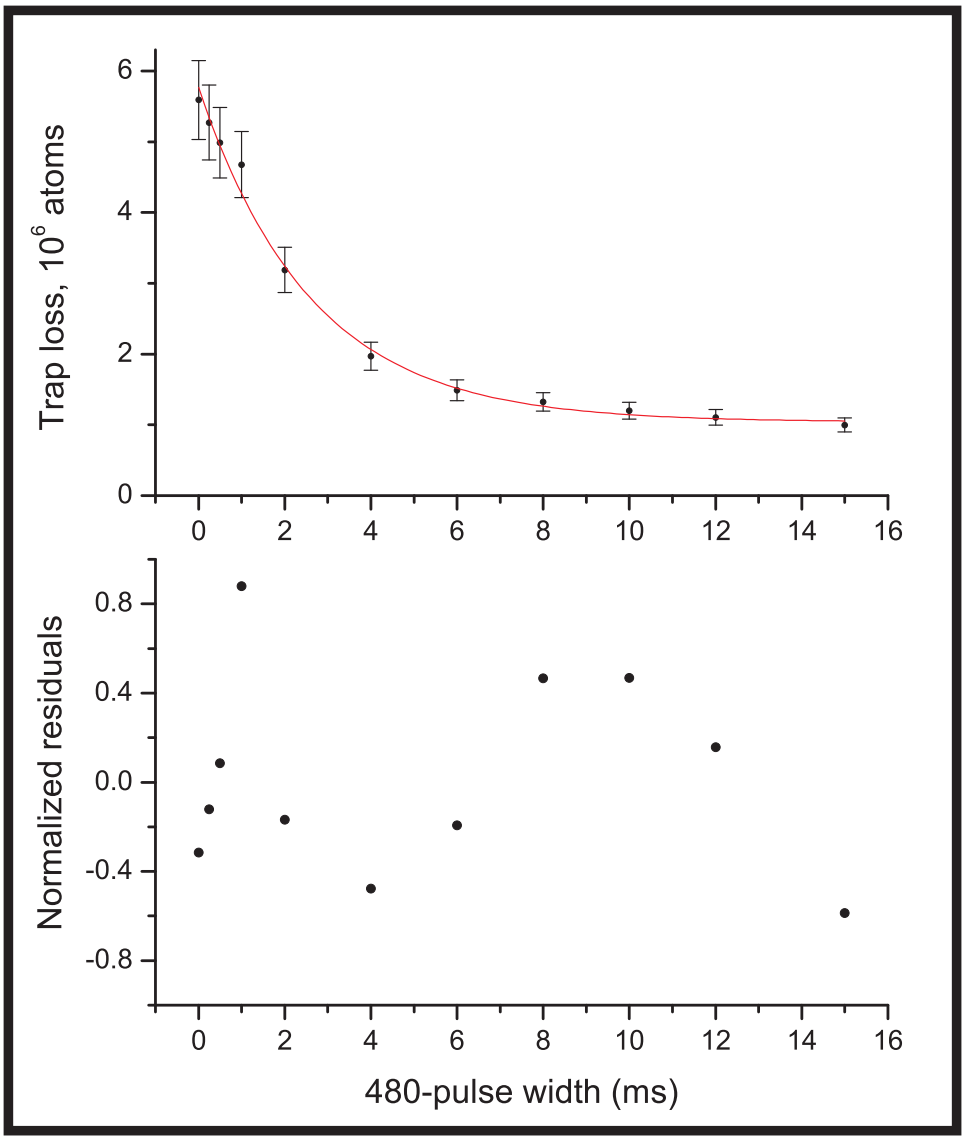

Figure 7.12: The decay of trapped atom number due to blackbody ionization (top plot). The solid curve represents the exponential fit (Eq.7.2) that provides the value of the Rydberg production rate $R_R = 1/(2.62 \pm 0.16)$. Normalized residuals for the fit are shown on the bottom plot.

increased Rydberg-Rydberg interactions. The developed experimental procedure can be directly extended to the domain of higher fields.

To investigate the effects of the external electric field we used the same exci-

tation scheme as before. A MOT cloud at the cooling light detuning of 40 MHz was exposed to the blue light for 5 ms. At this detuning, the Autler-Townes splitting reduces to a single resonance peak. The probe frequency was scanned around two-photon resonances in steps of 2 MHz. The electric field was generated by two metal electrodes as described in Chapter 6. The measured spectra for several voltages from 0 to 46.8 V applied to the electrodes are shown in Fig. 7.13-Fig. 7.17. Each data point represents a single measurement of the trap loss. We ascribed the vertical error bar to the data point based on 10-20% variation of the MOT atom number from one loading cycle to another. To illustrate the energy shift and broadening due to the increasing electric field we plotted all resonances on the same graph as shown in Fig. 7.18. The energy level shift responsible for the shift of the peak position is the expected DC Stark effect.

We used Lorentzian fits to extract the width and relative position of each resonance. The results are reported in the caption of the corresponding figure and are plotted in black for the peak position and in blue for resonance width in Fig. 7.19 (top). The error bar of each data point represents its uncertainty obtained from the Lorentzian fit of the corresponding spectroscopic feature. The data set for the peak position was fitted with a parabola (black solid line in Fig. 7.19), $y = a(x - x_0)^2$, where the offset of the independent variable x_0 is due to possible stray electric fields. The found the fit parameters $a = (-5.18 \pm 0.12) \cdot 10^{-2}$ MHz/V^2 and the electric field offset (in units of the electrode voltage) $x_0 = (-2.51 \pm 0.45)$ V. The normalized residuals for the peak position fit are shown on the bottom of Fig. 7.19. The data set for the resonance width was fitted with a parabola (blue solid line in Fig. 7.19), $y1 = Ax^2 + y_0$, and the fit parameters were found to be $a = (2.06 \pm 0.15) \cdot 10^{-3}$ MHz/V^2, $y_0 = (3.22 \pm 0.14)$ MHz.

The exact values of the electric field could not be calculated precisely due to the complicated geometry of the conducting surfaces of constant potential. To calibrate the electric field we perform numerical calculations of the Stark shift for 56s state. For that, we numerically evaluated the unperturbed radial wavefunctions

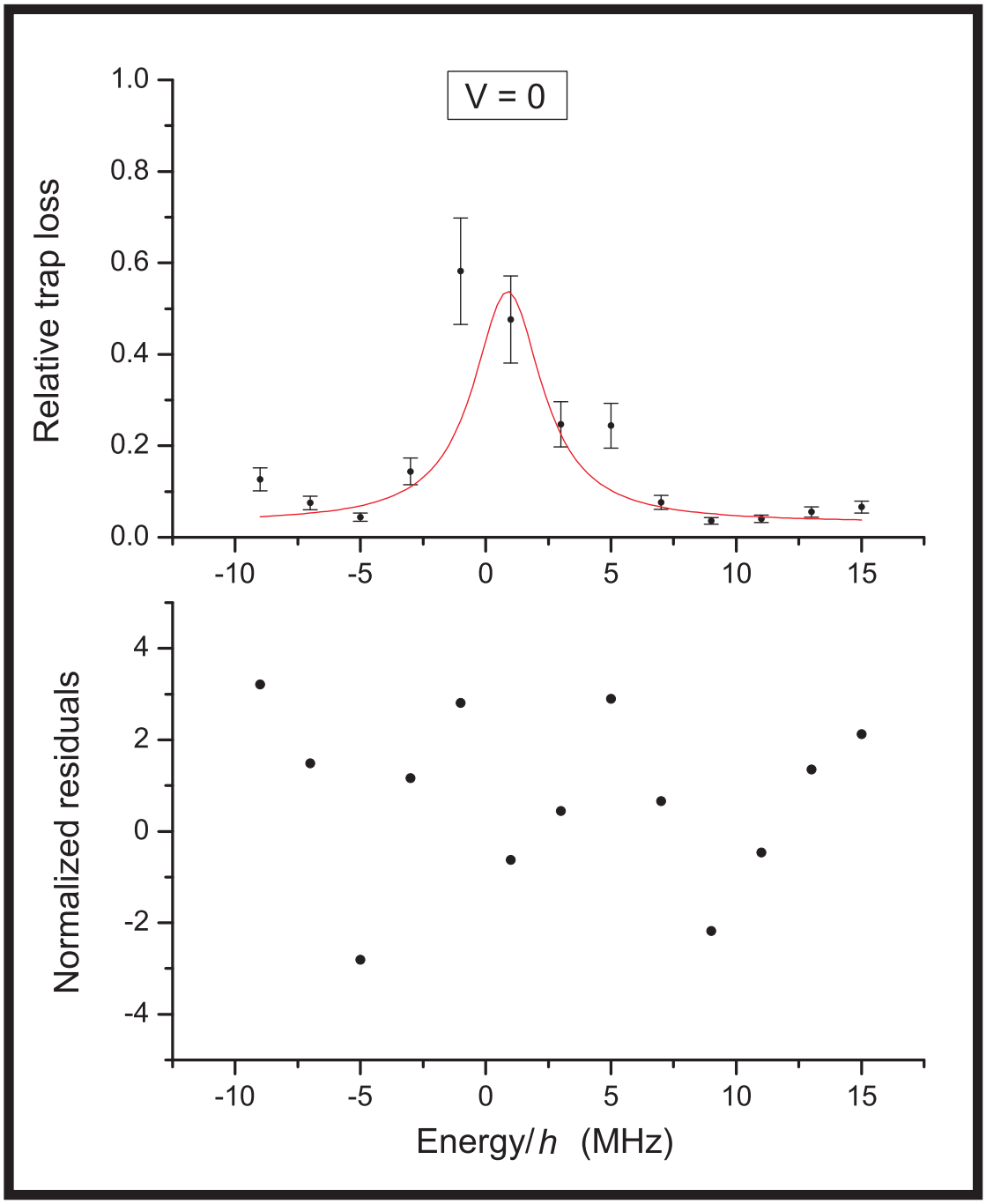

Figure 7.13: The Rydberg spectrum of the 56s state with both electrodes grounded (top) and the Lorentzian fit of the two-photon transition peak at $x_c = (0.88 \pm 0.71)$ MHz with the width, $w_c = (3.05 \pm 0.63)$ MHz. The normalized residuals of the fit are shown on the bottom plot. The corresponding reduced $\chi^2_{red} = 5.60$.

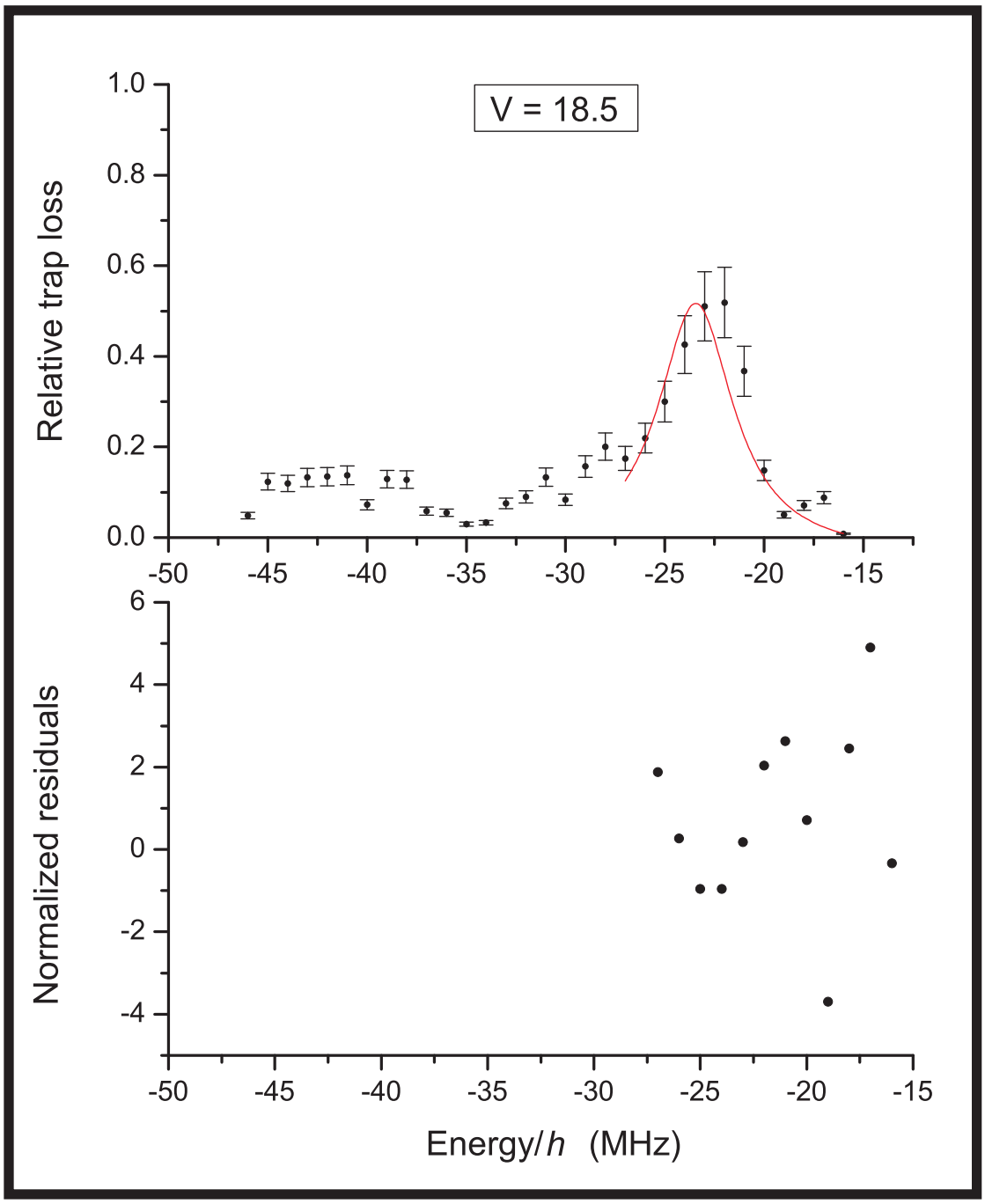

Figure 7.14: The Rydberg spectrum of 56s state in the presence of the external electric field generated by two electrodes at the voltage of 18.5 V (top) and the Lorentzian fit of the two-photon transition peak at $x_c = (-23.4 \pm 0.4)$ MHz with the width, $w_c = (3.69 \pm 1.14)$ MHz. The normalized residuals of the fit are shown on the bottom plot. The corresponding reduced $\chi^2_{red} = 7.61$.

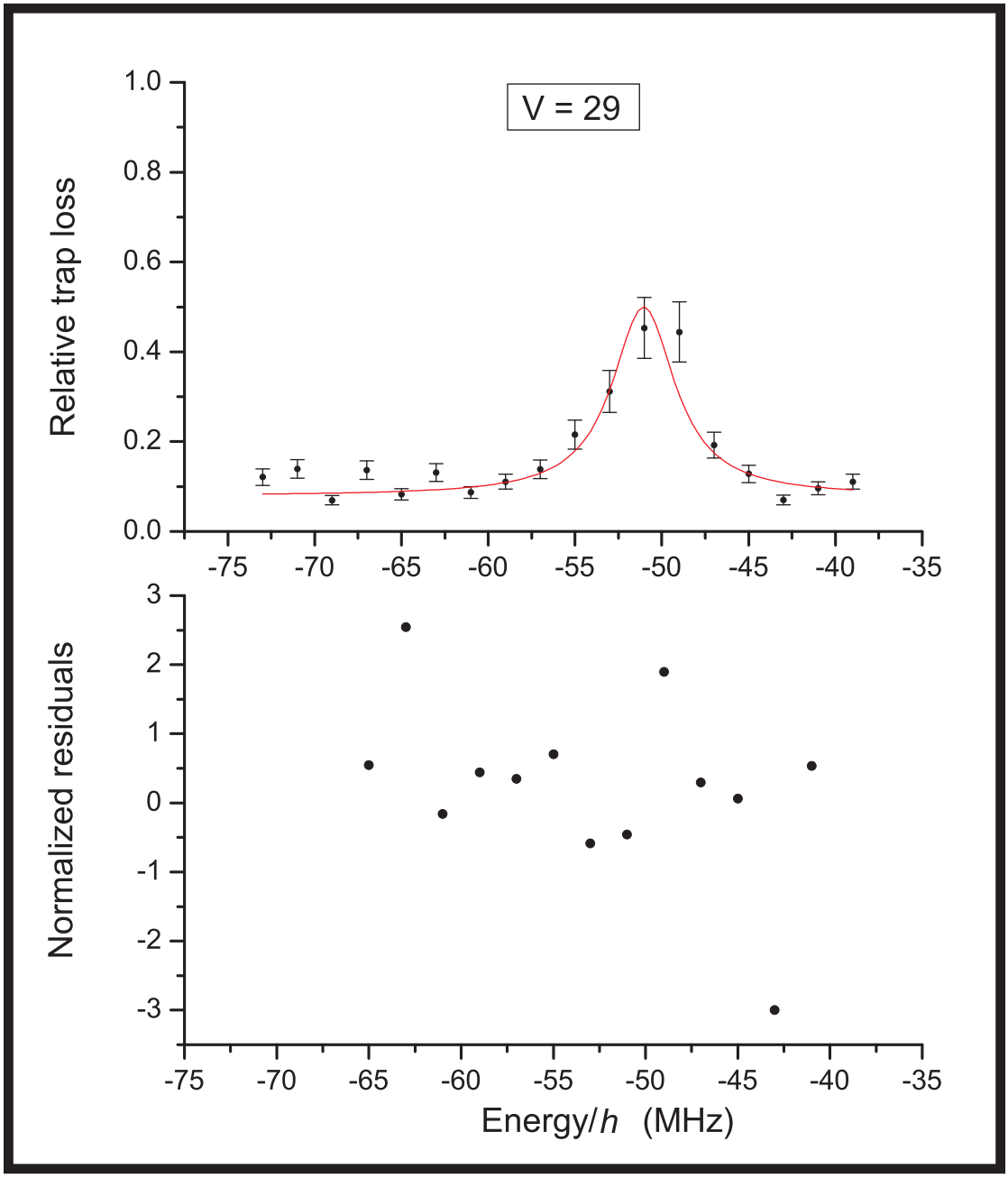

Figure 7.15: The Rydberg spectrum of 56s state in the presence of the external electric field generated by two electrodes at the voltage of 29 V (top) and the Lorentzian fit of the two-photon transition peak at $x_c = (-51.1 \pm 0.5)$ MHz with the width, $w_c = (5.04 \pm 0.82)$ MHz. The normalized residuals of the fit are shown on the bottom plot. The corresponding reduced $\chi^2_{red} = 2.35$.

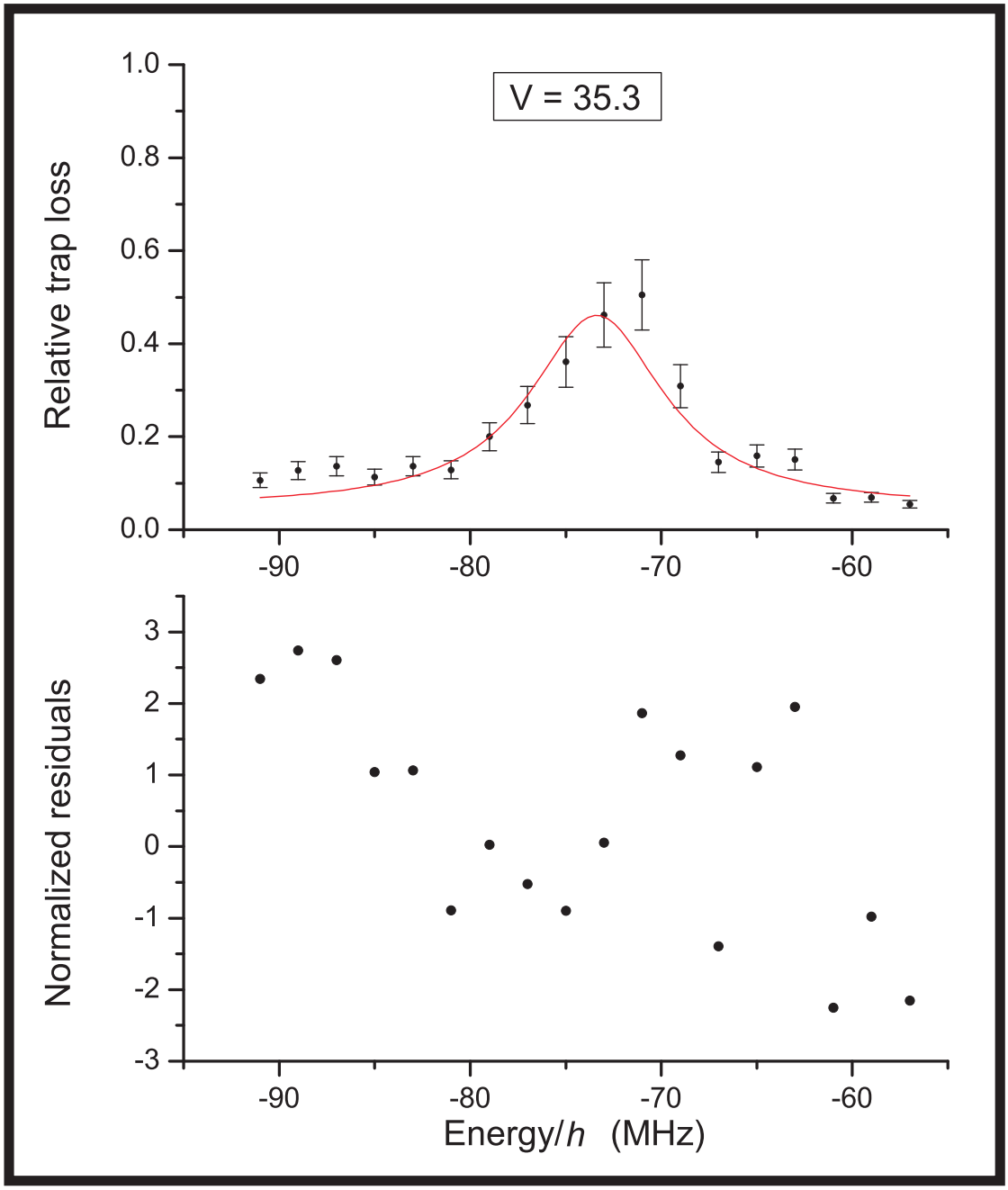

Figure 7.16: The Rydberg spectrum of 56s state in the presence of the external electric field generated by two electrodes at the voltage of 35.3 V (top) and the Lorentzian fit of the two-photon transition peak at $x_c = (-73.4 \pm 0.6)$ MHz with the width, $w_c = (5.82 \pm 1.80)$ MHz. The normalized residuals of the fit are shown on the bottom plot. The corresponding reduced $\chi^2_{red} = 3.71$.

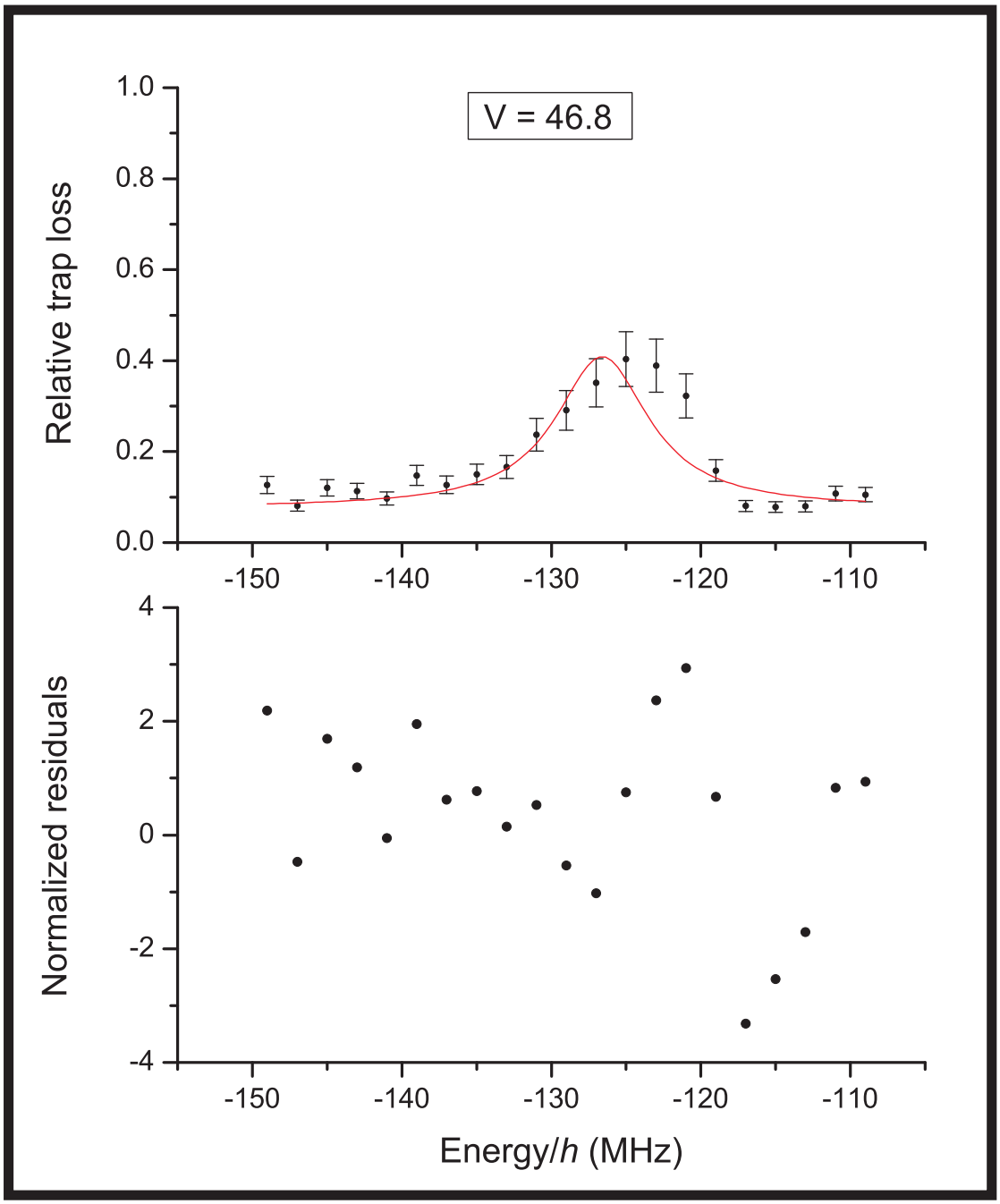

Figure 7.17: The Rydberg spectrum of 56s state in the presence of the external electric field generated by two electrodes at the voltage of 46.8 V (top) and the Lorentzian fit of the two-photon transition peak at $x_c = (-126.6 \pm 0.7)$ MHz with the width, $w_c = (7.59 \pm 2.16)$ MHz. The normalized residuals of the fit are shown on the bottom plot. The corresponding reduced $\chi^2_{red} = 3.11$.

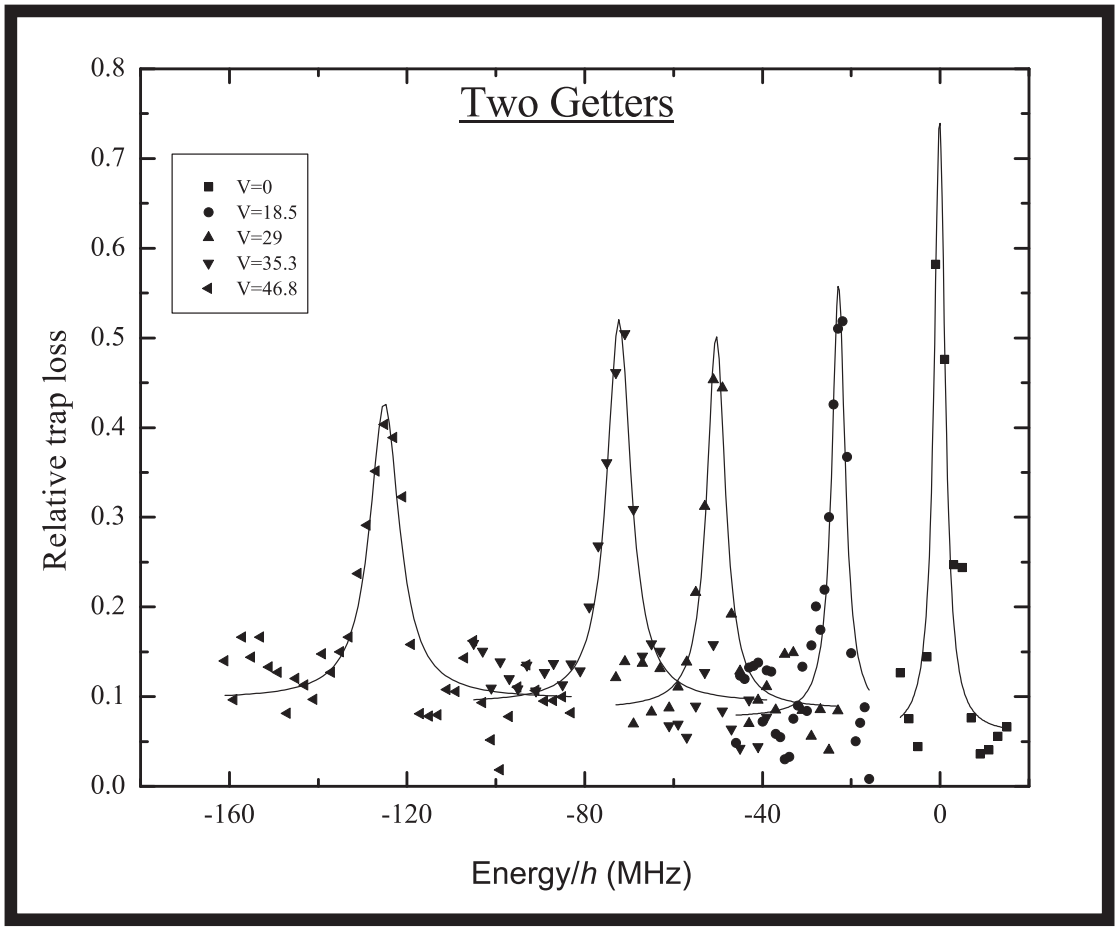

Figure 7.18: The Rydberg spectrum of 56s state for various electrode voltages

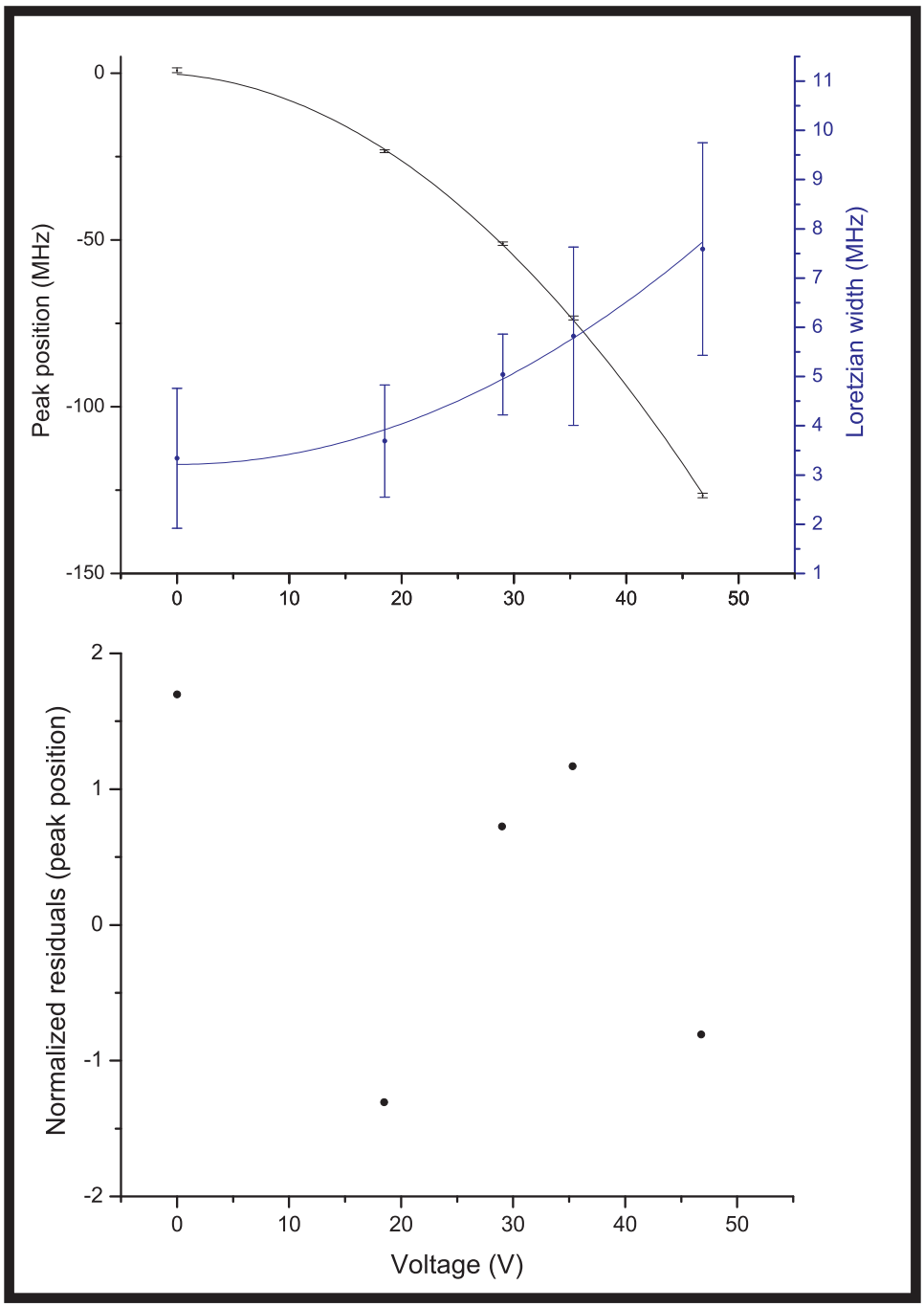

Figure 7.19: Dependence of the energy shift of the 56s state on the applied voltage resulted from the quadratic Stark effect. The shift of the resonance peak position is shown in black, peak width - in blue on the top plot. The bottom plot presents the normalized residuals from the parabolic fit of the peak position data. The reduced

chi^2_{red} was found to be 2.38.

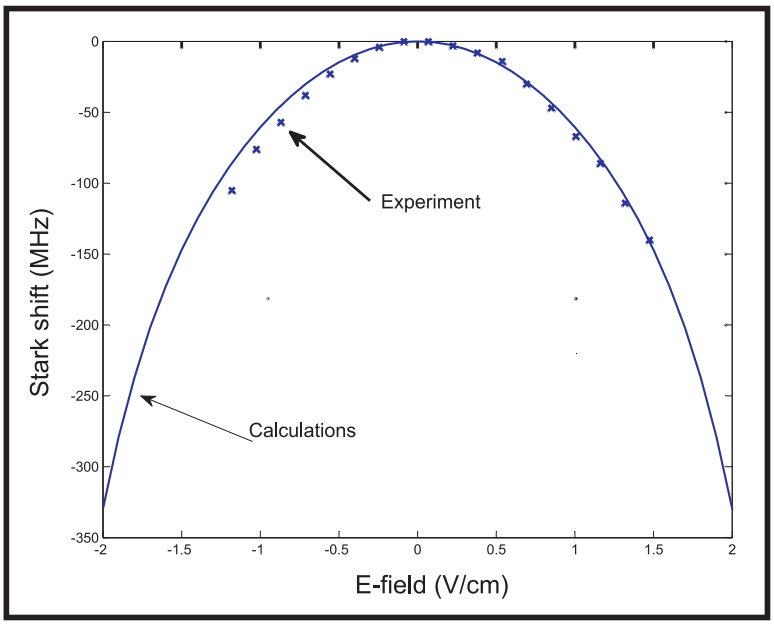

Figure 7.20: The calculated energy shift of the $56s$ state due to the DC Stark effect (solid line) the experimental data (crosses) were fit together to provide the calibration of the electrode voltage.

of a hydrogen-type one-electron atom for the known energy eigen-values given by the quantum defect theory [75]. The Stark shift Δ_{th} was then calculated from the perturbation theory for a mixture of four energy levels adjacent to $56s$ as discussed in Appendix D, and can be written in units of frequency as a parabolic function $\Delta_{th} = -82.5E^2$, where the coefficient of proportionality is in units of MHz/V^2/cm^2, and E is the electric field in units of V/cm. Comparison with the fit results for the peak position in Fig. 7.19 gives rise to the conversion factor between the electric field and the electrode voltage, $\alpha_{E-V} = (2.51 \pm 0.03) \cdot 10^{-2}$ cm^{-1}, such that $E = \alpha_{E-V}V$, where V is the electrode voltage.

Both calculated and measured energy shifts for positive and negative values of the electric field are presented in Fig. 7.20. Note, that the experimental data is asymmetric with respect to the vertical axis as a result of stray fields, which illustrates that the Stark effect can be a very sensitive tool to measure small elec-

tric fields. The results of the electric field calibration were qualitatively consistent with calculations performed by the SIMION ion and electron optics simulator software based on a simplified geometry of the electrodes. It was quite obvious that the quadratic broadening of the resonances as shown in Fig. 7.19 was dominated by the inhomogeneity of the electric field across the atomic cloud. To investigate the results of the inhomogeneity we conducted the Stark shift spectroscopy measurements with only one electrode kept at a constant voltage to enhance the field inhomogeneity. The applied voltage was chosen such that the resonances occur at the same probe frequencies as those for the case of two electrodes. Obtained spectra are shown in Fig. 7.21 (top), along with the 2-electrode spectra (bottom) for comparison.

It is clear that the intentionally introduced inhomogeneity dramatically broadened the resonances. The SIMION simulations showed a 20% variation of the field across a 1 mm cloud for the case of one electrode and 3% for the two-electrode configuration qualitatively consistent with the observed broadening. Therefore it is an open question whether the resonance broadening due to the Rydberg-Rydberg interactions increasing with the field can be separated from the inhomogeneity-induced width of resonance.

7.3 Discussion and On-going Work

In conclusion, we constructed a narrow linewidth laser system and successfully used it for Rydberg excitations of rubidium. Spectroscopic measurements of Rydberg resonances revealed a broadening of the resonances that could be induced by the interactions between the Rydberg atom and the inhomogeneity of the applied electric field. The field inhomogeneity was found to be the primary source of the broadening, and it needs to be suppressed to separate the effects of interactions and the inhomogeneous field. There are several ways to approach this goal. Higher electric fields and smaller excitation volumes may increase the strength of inter-

actions as atoms gain permanent dipole moments, while the inhomogeneity of the field is kept small. Smaller excitation volumes can be achieved by either focusing the 480-beam, or conducting the excitations of a smaller cloud produced by the evaporative cooling.

The current detection system relies on the trap loss due to ionization by black-body radiation, which is limited by a low ionization rate. The rate can be greatly enhanced by radiative ionization with a high power far off-resonant laser beam at 1550 nm, which is available in the laboratory.

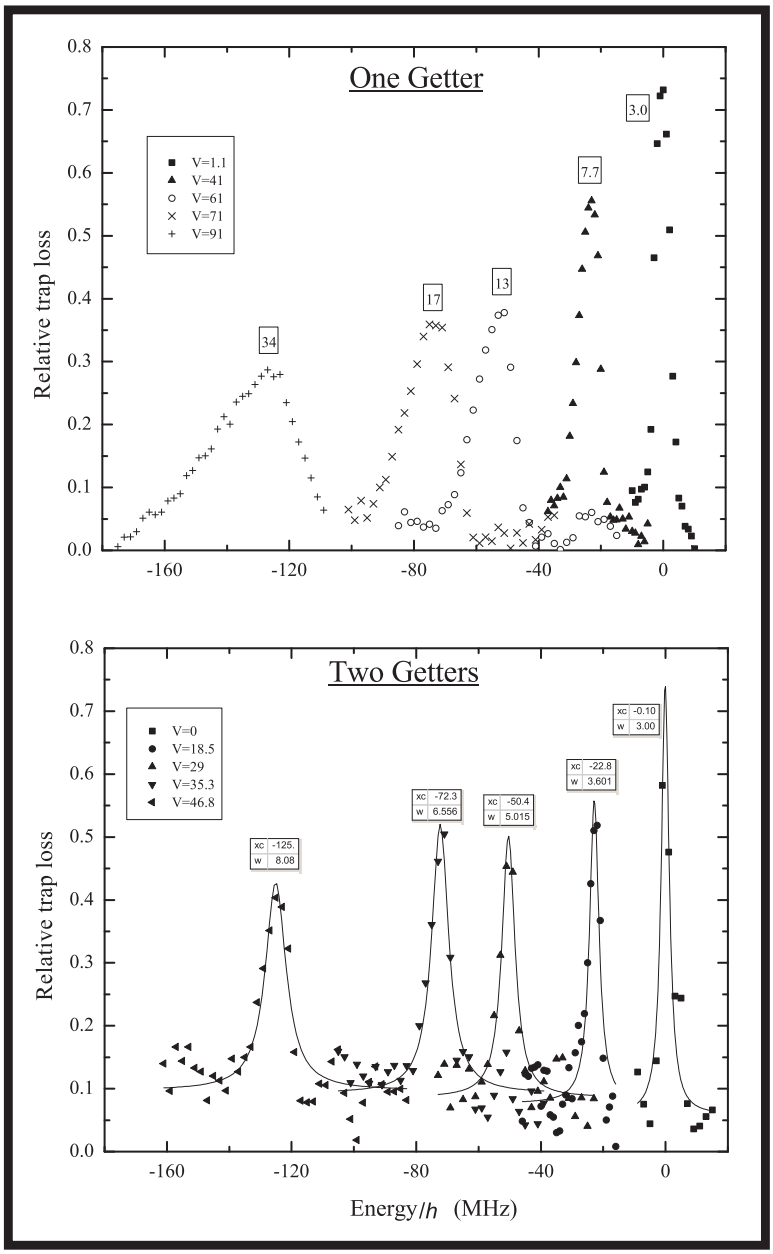

Figure 7.21: Stark shifted spectra for one- and two-electrode configuration. In case of one electrode, the generated field inhomogeneity results in a large resonance broadening (top). The two-electrode configuration results in more homogeneous field and smaller broadenings (bottom).

Chapter 8

Summary of Dissertation

In this dissertation we reported the results of two experimental projects with laser-cooled rubidium atoms. The first part of the thesis is devoted to the development of new elements of atom optics based on blue-detuned high-order Bessel beams. We assembled a cold atom apparatus to produce a 1-mm cloud of about 10^8 rubidium atoms in a MOT at 250μK. A 4th-order Bessel beam of 1 mm in diameter generated by an SLM was used to guide the atoms. The properties of this type of guide were investigated for various parameters of the hollow beam, such as the detuning from an atomic resonance, size and the order of the Bessel beam. We extended its application to create more complicated interferometer-type structures by demonstrating a *tunnel lock*, a novel device that can split an atomic cloud, transport it, delay, and switch its propagation direction between two guides. We reported a first-time demonstration of an atomic beam switch based on the combination of two crossed Bessel beams. We achieved the 30% efficiency of the switch limited by the geometrical overlap between the cloud and the intersection volume of the two tunnels, and investigate the heating processes induced by the switch. We also showed other applications of crossed Bessel beams, such as a 3-D optical trap for atoms confined in the intersection volume of two hollow beams and a splitter of the atomic density.

The second part of this dissertation is devoted to the spectroscopic measurements of the Rydberg blockade effect, a conditional suppression of Rydberg excitations depending on the state of a control atom. We assembled a narrow-linewidth,

tunable, frequency stabilized laser system at 480 nm to excite laser-cooled rubidium atoms to Rydberg states with a high principal quantum number $n \sim 50$ through a two-photon transition. We applied the laser system to observe the Autler-Townes splitting of the intermediate $5p_{3/2}$ state and used the broadening of the resonance features to investigate the enhancement of Rydberg-Rydberg interactions in the presence of an external electric field. The observed broadening was mainly due to the inhomogeneity of the applied electric field across the atomic cloud. Experiments are currently in progress to distinguish between the two sources of broadening using smaller excitation volumes, higher detection sensitivity of Rydberg excitations and the dependence of the atom-atom interactions on density.

Appendix A

Appendix A. Aspects of Light-matter Interactions

In this section we outline several basic concepts of light interaction with a two-level atom. The derived light force illustrates the idea of the laser cooling and trapping of atoms. If an atom initially in a lower energy level absorbs a photon of momentum k from a laser beam, the former receives momentum $\hbar k$ and is excited to a higher energy level. Consecutive irradiation of a photon leads to de-excitation of the atom and momentum transfer (recoil) from the photon with a corresponding recoil energy of

$$E_{rec} = \frac{\hbar^2 k^2}{2M}. \tag{A.1}$$

Emission processes occur along two channels, spontaneous and stimulated. Each one of them in combination with preceding absorption gives rise to two different forces the light exerts on the atom, spontaneous emission and stimulated emission forces.

A.1 Spontaneous Emission Force

In case of spontaneous emission, the angular distribution of the irradiated photons is symmetric and scattering of a large number of photons results in zero net recoil momentum. Indeed, momentum conservation after summation of N scattering events

$$\boldsymbol{p}_N + N\hbar\boldsymbol{k} = \boldsymbol{p}_0 + \sum_i \hbar\boldsymbol{k}_i, \tag{A.2}$$

shows that the atom gains momentum in direction of the laser beam, $\boldsymbol{k}$, when the last term can be neglected for a large N. In the Eq. A.2, $\boldsymbol{p}_0$, $\boldsymbol{p}_N$ are corresponding initial and final momenta of the atom, $\boldsymbol{k}_i$ is the recoil momentum of the i_{th} emitted photon. If one introduces the force as an expectation value of a force operator $\mathcal{F}$ = d$\boldsymbol{p}$/dt, then according to the Ehrenfest theorem

$$F = \langle \mathcal{F} \rangle = -\langle \ \nabla V(\mathbf{r}) \ \rangle, \tag{A.3}$$

where V is a potential corresponding to the light-atom interaction exerting the force F. The part of the interaction potential contributing to the expectation value is (for a rigorous derivation, see, for example [108])

$$V = -e\,\boldsymbol{\mathcal{E}} \cdot \boldsymbol{r}, \tag{A.4}$$

where $\boldsymbol{\mathcal{E}}$, $\boldsymbol{r}$ are the electric field and atomic dipole operators accordingly. For optical wavelengths the spatial variation of the electric field over the atomic size is negligible (electric dipole approximation) and the expectation value can be taken before the gradient in Eq. A.3. We consider the electric field operator of the monochromatic traveling wave in the form

$$\boldsymbol{\mathcal{E}} = \frac{E_0}{2}\boldsymbol{\varepsilon}(e^{i(kz-\omega t)} + c.c.), \tag{A.5}$$

where E_0 is the amplitude, $\boldsymbol{\varepsilon}$ is the polarization vector and ω is the frequency of the laser field.

We further ignore quantum correlations (semi-classical radiation theory) and replace the operators in Eq. A.4 by their corresponding expectation values. In that case, $\langle \boldsymbol{\mathcal{E}} \rangle$ is interpreted to be a classical electric field vector. It is convenient to calculate the expectation values in (A.3) using the density matrix formalism: for an operator $\mathcal{A}$, its expectation value $\langle \mathcal{A} \rangle = \mathrm{Tr}(\rho \mathcal{A})$. The density matrix operator ρ evolves in time as follows:

$$i\hbar\frac{d\rho}{dt} = -[\rho, \mathcal{H}], \tag{A.6}$$

where $\mathcal{H} = \mathcal{H}_0 + \boldsymbol{V}$ is the full Hamiltonian of the system comprised of a field-free, time-independent Hamiltonian $\mathcal{H}_0$ and the atom-light interaction part $\boldsymbol{V}$. The time-dependent Schrödinger equation corresponding to the full Hamiltonian

$$i\hbar\frac{\partial\Psi(\boldsymbol{r},t)}{\partial t} = \mathcal{H}\Psi(\boldsymbol{r},t) \tag{A.7}$$

is equivalent to

$$i\hbar\frac{dc_j}{dt} = \sum_k c_k(t)V_{jk}(t)e^{i\omega_{jk}t}, \tag{A.8}$$

where $\omega_{jk} \equiv \omega_j - \omega_k$ is the difference between the eigenvalues ω_j of the Hamiltonian $\mathcal{H}_0$, $c_j(t)$ are the expansion amplitudes of the atom wavefunctions Ψ in the basis of the eigenfunctions $\{\phi_j\}$ of $\mathcal{H}_0$, and V_{jk} are the matrix elements of the interaction Hamiltonian in the same representation[1].

For a pure state, the density matrix can be expressed in terms of the expansion amplitudes c_j,

$$\rho_{jk} = c_j c_k^*, \tag{A.9}$$

and can be calculated after solving Eq. A.8 for c_j for the case of a specific interaction V. Knowing the matrix density operator one can obtain the expression for the light force from Eq. A.3.

We assume that the laser light frequency ω is close to the energy difference (in units of frequency) $\omega_a \equiv \omega_{12} = \omega_{21}$ between the two levels of the atom, $j, k = 1, 2$, *i.e.*, the laser detuning from the atomic resonant frequency $\delta \equiv \omega - \omega_a \ll \omega, \omega_a$. This assumption (two-level atom model) is reasonable for a variety of experiments in Atomic Physics and justifies the truncation of the summation of Eq. A.8 to

[1]Note that V_{jk} contains only off-diagonal elements as V is odd under parity

just two terms. The complete solution of the Eq. A.8 contains "non-resonant" $\frac{1-exp(i(\omega_0+\omega_a)t)}{\omega_0+\omega_a}$ and "resonant" $\frac{1-exp(i(\omega_0-\omega_a)t)}{\omega_0-\omega_a}$ terms, and only the latter have the dominant contribution to the elements of the density matrix at small detunings δ. We therefore retain only the "resonant" terms in Eq. A.8 when calculating the $V_{jk}e^{i\omega_{jk}t}$ products (rotating-wave approximation). For a rigorous application of the rotating-wave approximation to the two-level atom refer, for example, to Ref.[109].

Time evolution of the density matrix in terms of amplitudes c_j can be obtained by differentiating Eq. A.9

$$\frac{d\rho_{jk}}{dt} = c_j\frac{dc_k^*}{dt} + c_k^*\frac{dc_j}{dt}. \tag{A.10}$$

The semi-classical radiation theory does not include spontaneous emission, and it must be introduced phenomenologically. We choose the lower energy level of the atom, $j = 1$ to be the ground state that does not decay ($\gamma_1 = 0$), and describe the spontaneous emission by an exponential decay of the upper level, $j = 2$

$$\frac{dc_2(t)}{dt} = -\frac{\gamma_2}{2}c_2(t), \tag{A.11}$$

such that the upper level population decays with the rate $\gamma_2 \equiv \gamma$ with lifetime $\tau = 1/\gamma$. Spontaneous emission can now be included in Eq. A.8

$$i\hbar\frac{dc_j}{dt} = \sum_k c_k(t)V_{jk}(t)e^{i\omega_{jk}t} - i\hbar\frac{\gamma_j}{2}c_j(t) \qquad j,k = 1,2. \tag{A.12}$$

Substituting dc_j/dt and c_j from Eq. A.12 and A.9 correspondingly into Eq. A.11 give rise to the optical Bloch equations (OBE)

$$\frac{d\tilde{\boldsymbol{\rho}}}{dt} = \begin{pmatrix} 0 & -\frac{i}{2}\Omega & -\frac{i}{2}\Omega^* & \gamma \\ -\frac{i}{2}\Omega^* & -(\frac{\gamma}{2}+i\delta) & 0 & \frac{i}{2}\Omega^* \\ \frac{i}{2}\Omega & 0 & -(\frac{\gamma}{2}-i\delta) & -\frac{i}{2}\Omega \\ 0 & \frac{i}{2}\Omega & -\frac{i}{2}\Omega^* & -\gamma \end{pmatrix}\tilde{\boldsymbol{\rho}}, \tag{A.13}$$

where we have introduced a 4-vector $\tilde{\boldsymbol{\rho}} = (\rho_{11} \quad \rho_{12}e^{-i\delta t} \quad \rho_{21}e^{-i\delta t} \quad \rho_{22})^T$ composed of the elements of the density matrix operator, and expressed the interaction via the Rabi frequency

$$\Omega \equiv -\frac{eE_0}{\hbar}\langle\phi_2|r|\phi_1\rangle. \tag{A.14}$$

We can now re-write the expectation value in Eq. A.3 with the elements of the density matrix and the Rabi frequency for the light force along the direction of the laser beam $\hat{z} = \frac{\boldsymbol{k}}{|\boldsymbol{k}|}$

$$F_z = \hbar\left(\frac{\partial\,\Omega}{\partial z}\rho_{21}^* + \frac{\partial\,\Omega^*}{\partial z}\rho_{21}\right). \tag{A.15}$$

Off-diagonal matrix element ρ_{21} (note, $\rho_{jk} = \rho_{kj}^*$)) can be calculated from a steady-state solution of the optical Bloch equations (A.13). Particularly,

$$\rho_{21} = \frac{i\Omega}{2(\gamma/2 - i\delta)(1+s)}, \tag{A.16}$$

and

$$\rho_{22} = \frac{s}{2(1+s)}, \tag{A.17}$$

where the saturation parameter s is given by

$$s = \frac{2|\Omega|^2}{4\delta^2 + \gamma^2}. \tag{A.18}$$

The force can be expressed in terms of the real, q_r, and imaginary, q_i, parts of the logarithmic derivative of Ω, $\partial \lg\Omega/\partial z = (q_r + iq_i)$, and Eq. A.15 will be

$$F = \hbar\frac{s}{s+1}(-\delta q_r + \frac{1}{2}\gamma q_i), \tag{A.19}$$

where the first term is proportional to the gradient of the electric field amplitude and second - to the gradient of the field's phase.

For the case of multiple absorption and consecutive spontaneous emission events, Eq. A.2 gives rise to the expression of the spontaneous (light or radiation pressure) force

$$F_{sp} = \hbar k \gamma \rho_{22} = \hbar k \frac{\gamma/2}{1 + \gamma^2/2\Omega^2 + 4\delta^2/2\Omega^2}, \tag{A.20}$$

which coincides with the second term in Eq. A.19 for the case of a traveling wave.

For practical purposes, it is convenient to introduce the saturation parameter on resonance, $s_0 = s|_{\delta=0}$, and the expression for the spontaneous force will be

$$F_{sp} = \hbar k \frac{\gamma}{2} \frac{s_0}{1 + s_0 + (2\delta/\gamma)^2}. \tag{A.21}$$

The on-resonance saturation parameter can be expressed via the intensity of the laser beam I,

$$s_0 \equiv 2\frac{|\Omega|^2}{\gamma^2} = I/I_s, \tag{A.22}$$

where we follow Citron *et al.* [30] definition of the saturation intensity

$$I_s \equiv \frac{h\pi c\gamma}{3\lambda^3}. \tag{A.23}$$

We can apply the derived expression for the scattering rate (A.17) to calculate the heating rate of a 1 mm rubidium cloud with a Gaussian density distribution placed inside a 1 mm hollow core of a $4th$-order Bessel beam. Consider a thermal cloud in cylindrical coordinates (r, ϕ, z) with the Gaussian density distribution along the z-axis, ρ_z, and uniform, ρ_r and ρ_ϕ in the (r, ϕ)-plane:

$$\rho(r, \phi, z) = \begin{cases} N_r/R & r \leq R, \\ N_\phi/R & 0 \leqslant \phi \leqslant 2\pi, \\ N_z e^{-(z-z_0)^2/2\sigma_z^2} & -\infty < z < +\infty, \end{cases} \tag{A.24}$$

where N_r, N_ϕ, N_z, z_0 are constants, σ_z is the width of the Gaussian distribution in z-direction, and R is the radius of the cloud in the transverse plane. If N_0 is the total number of atoms in the cloud, then normalization of the distribution (A.24) gives rise to $N_0 = \sqrt{2\pi^3} N_r N_\phi N_z$.

The total number of photons absorbed by the whole cloud is given by the integral

$$N_{ph} = \int_V \mathcal{R}\rho \, dV \tag{A.25}$$

over the elementary volume V. There, $\mathcal{R} = \gamma\rho_{22}$ is the photon scattering rate per atom, which for a large detunings and high laser intensities is reduced to

$$\mathcal{R} = \frac{\gamma}{2} \frac{s_0(r)}{(2\delta/\gamma)^2}, \tag{A.26}$$

where the saturation parameter on resonance $s_0 = I(r)/I_{sat}$ is determined by the intensity of the Bessel beam in the transverse plane $I(r) = I_0[J_4(k_r r)]^2$, $J_4(k_r r)$ is the $4th$-order Bessel function of the first kind, and $k_r = 10635\ \mathrm{m}^{-1}$ is the transverse spatial frequency of the 1 mm diameter Bessel beam. For 70 mW of power in the first ring of the Bessel beam, $I_0 = 6 \cdot 10^4\ \mathrm{mW/cm^2}$, and the total number of the absorbed photons (A.25) will be

$$N_{ph} = \frac{2}{R^2} N_0 \int_0^R r\mathcal{R}(r) \, dr.$$

Numerical calculation of the radial integral leads to the number of photons absorbed by each atom per second at a given detuning δ:

$$N_{ph}/N_0 \sim 10^{-3} \left(\frac{2\delta}{\gamma}\right)^2. \tag{A.27}$$

A.1.1 Absorption from Laser Beam by Atomic Cloud

Consider a laser beam of intensity I traveling along z-axis through an atomic cloud of density n. The amount of scattered power per unit volume is given by $\hbar\omega\mathcal{R}n$,

and thus $\mathrm{d}I/\mathrm{d}z = -\hbar\omega\mathcal{R}n$, where $\mathcal{R}$ is the scattering rate given by Eq.(A.26). For low intensity light near the atomic resonance,

$$\frac{\mathrm{d}I}{\mathrm{d}z} = -\sigma_{eg} n I, \tag{A.28}$$

where the two-level atom cross section σ_{eg} for scattering light out of the beam on resonance is given by

$$\sigma_{eg} = \frac{3\lambda^2}{2\pi}.$$

The solution of Eq.(A.28) is $I(z) = I_0 e^{-\int \sigma_{eg} n(z) I \mathrm{d}z}$ and allows to study the density of the absorbing cloud if the laser beam intensities after the absorption, $I(z)$, and without absorption, I_0, can be measured by a CCD array. This approach is widely used in AMO physics, and we refer to it as the absorption imaging technique throughout the thesis.

A.2 Velocity Dependent Force

The radiation pressure force (A.21) is conservative and does not account for the motion of an atom. One can include the atomic velocities into the optical Bloch equations (A.13) or consider them as small corrections to the solutions of the OBE for the atom at rest [110]. A simpler (but less rigorous) approach is to introduce the velocity dependence through a Doppler shift contribution to the effective detuning of the laser beam frequency from the atomic resonance $\delta - \boldsymbol{k}\cdot\boldsymbol{v}$, where $\boldsymbol{v}$ is the velocity of the atom. We can now write the velocity-dependent expression for the radiation pressure force

$$F_v = \hbar k \frac{\gamma}{2} \frac{s_0}{1 + s_0 + 4((\delta - \boldsymbol{k}\cdot\boldsymbol{v})/\gamma)^2}. \tag{A.29}$$

For the case of an atom moving with a small velocity v in a counter-propagating non-saturated laser beam, the last equation can be linearized in v to obtain the expression for the velocity-dependent force

$$F_{sp}(v) = F_{sp} - \beta v, \tag{A.30}$$

where F_{sp} is velocity-independent force given by the Eq. A.21, and the damping coefficient β is given by

$$\beta = -\hbar k^2 \frac{4s_0(\delta/\gamma)}{(1 + s_0 + 4(\delta/\gamma)^2)^2}. \tag{A.31}$$

For the red-detuned ($\delta < 0$) laser beam the damping coefficient is positive, thus resulting to the deceleration of the atom. If a collection of atoms with Maxwellian velocity distribution is exposed to a near-resonant laser beam, only a certain velocity class of the ensemble will decelerate. The slow atoms that have the velocity component in the direction opposite to the propagation direction of the laser beam ($\boldsymbol{k} \cdot \boldsymbol{v} = -(kv)_z$) such that the effective detuning does not exceed the width of the profile of the radiation pressure force (A.29)

$$(\delta + kv)^2 < \gamma^2(1 + s_0), \tag{A.32}$$

and for small detunings only atoms with the initial velocity below a capture velocity

$$v_c = \frac{\gamma}{k} \tag{A.33}$$

will undergo multiple scattering events and be efficiently decelerated to small velocities. For ^{87}Rb, $v_c = 4.7$ m/s, while the average velocity of Maxwell distribution at room temperature is about 170 m/s. Therefore, only a small fraction of the ensemble can scatter photons from the laser beam. The recoil velocity is only 5.88 mm/s, and thus multiple scattering events are required to slow down the atoms substantially.

A.3 Optical Molasses

Consider an atom scattering photons from two counter-propagating but otherwise identical laser beams[2]. In the one-dimensional case the light pressure force from the two beams will be, according to Eq. A.30[3]

$$\boldsymbol{F}_{sp} = -2\,\beta \boldsymbol{v}. \tag{A.34}$$

For the red-detuned laser beams ($\beta > 0$) the light pressure force viscously damps the atomic motion. This cooling mechanism is called optical molasses: an atom traveling along one of the laser beams scatters less photons from that beam than it does from the other, the counter-propagating beam, which is closer to the atomic resonance due to the Doppler shift. Thus the atom gains net momentum opposing its velocity in agreement with Eq. A.34. The damping force fluctuates around its average value due to discrete momentum transfer upon the absorption/emission events. When these events are uncorrelated, atomic momentum undergoes a random walk, and the mean square of the momentum $< p^2 >$ (kinetic energy) increases. Equilibration of this heating mechanism with the damping sets the Doppler-cooling limit. In case of a single laser beam, the momentum diffusion coefficient from the spontaneous emission

$$D_{sp} =< \dot{p}^2 >= \hbar^2 k^2 \, \frac{\gamma}{2} \frac{s_0}{1 + s_0 + 4(\delta/\gamma)^2} \tag{A.35}$$

is equal to the momentum diffusion coefficient from absorption D_{abs} in the low intensity limit as the mean number of emitted photons is equal to that of absorbed.

Equating the heating rate with the rate of the damping cooling

$$< \dot{E}_{heat} >= \frac{D_{sp} + D_{abs}}{M} = - < \dot{E}_{cool} >= \beta < v^2 >, \tag{A.36}$$

[2]Intensities are low and stimulated emission is neglected.

[3]This could be obtained directly from the second term of Eq. A.12 representing the electric field in the standing wave form.

we obtain the cooling limit in units of temperature

$$k_B T = -\hbar \frac{\gamma}{2} \frac{1 + s_0 + (2\delta/\gamma)^2}{2\delta/\gamma}, \tag{A.37}$$

and for the low intensity limit $s << 1$ the temperature reaches its minimum value, the Doppler-cooling limit

$$k_B T_D = \frac{\hbar\gamma}{2} \tag{A.38}$$

at $\delta = -\gamma/2$. Early time-of-flight measurements in sodium, however, revealed the molasses temperatures of an order of magnitude lower than the expected Doppler-cooling limit [111]: in Zeeman-degenerate atoms, sub-Doppler cooling mechanisms permit temperatures substantially below this limit [112].

Optical molasses may slow the atoms down but do not provide a trapping mechanism that would allow collection of a long-lived large atomic sample. The atoms in the molasses undergo diffusion with the maximum diffusion time given by [111]

$$t_d = \frac{4k^2 \langle r^2 \rangle}{27 N^2 \gamma}, \tag{A.39}$$

where $\langle r^2 \rangle$ is the mean square distance diffused and N is the molasses dimension. For rubidium it takes about 200 ms to diffuse a 1 mm distance. Moreover, for a static optical field that produces a radiation pressure force linearly proportional to the light intensity (Eq.A.29), it is not possible to create a 3-D stable trap [113].

A.4 Magneto-optic Trap

One can build upon the optical molasses setup by creating a radiation pressure force that selectively interacts with the Zeeman sublevels of the upper state such that an atom displaced from the origin scatters photons preferably from the laser beam that pushes it back to the origin. Such configuration was first demonstrated as a 3-D

trap by Raab, *et al.* [114]. The combination of the optical molasses and two anti-Helmholtz coils constitutes the Magneto-optical Trap (MOT) and is schematically presented in Fig. A.1 (left). The anti-Helmholtz coils create a magnetic field B which is zero at the origin and linear with the distance away from the origin in its small vicinity. The upper state Zeeman splitting for such an arrangement in 1-D is shown in Fig. A.1 (right): the energy of $m = +1$ sublevel increases linearly along the positive direction of the z-axis while the energy of the $m = -1$ sublevel decreases, and the frequency shift can be written as $\omega_z = \mu B/\hbar = bz$, and b is proportional to the magnetic field gradient. Optical molasses are formed by two counterpropagating laser beams with opposite directions of the circular polarization $\sigma^+$and σ^-, and the atom absorbing from the σ^+-beam gets excited to the $m = +1$ uppers state while the σ^--beam excites the atom into the $m = -1$ state. The molasses beams are red-detuned from the $|g, m = 0\rangle \rightarrow |e, m = 0\rangle$ transition (dashed line in Fig. 1). Therefore, an atom displaced by z from the origin will be preferably excited into $m = -1$ state by the σ^--beam (relative detuning of $\delta - bz$) rather than into $m = +1$ state by the σ^+-beam (relative detuning of $\delta + bz$). The preferred scattering from the σ^+-beam provides a restoring force that pushes the atom back to origin. A similar argument applies if the atom is placed the distance $-z$ away from the origin.

In the low intensity limit, the total force exerted by the two beams on an atom dispaced by a distance z is given by

$$F = \hbar k \frac{\gamma}{2} \left[\frac{s_0}{1 + s_0 + 4((\delta - kv - bz)/\gamma)^2} - \frac{s_0}{1 + s_0 + 4((\delta - kv + bz)/\gamma)^2} \right]. \quad \text{(A.40)}$$

For small velocities and a low magnetic field ($kv, bz << \gamma$), we can write the force as a function of the velocity and the displacement

$$F = -2\beta v - \kappa r, \quad \text{(A.41)}$$

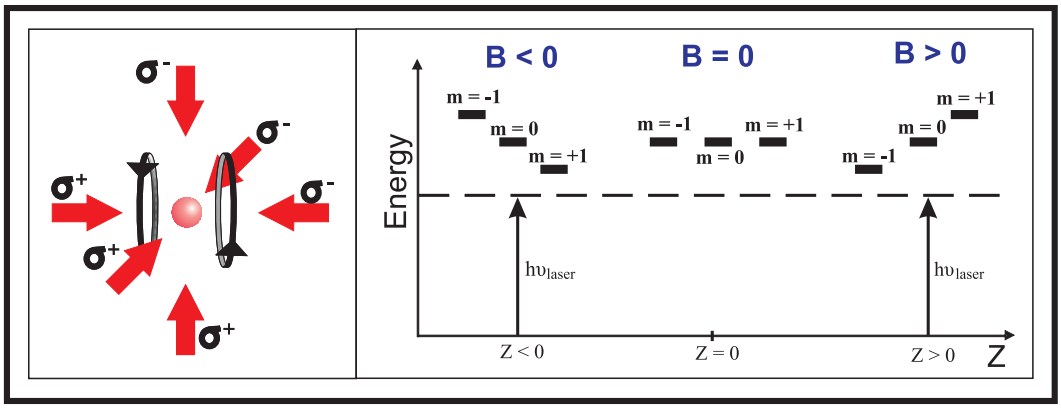

Figure A.1: Magneto-optical trap. Proper polarization of six molasses beams in combination with a magnetic field gradient provide a cooling mechanism to slow atoms down and a restoring force to keep them trapped in the intersection region of the beams (left). The right panel illustrates an energy splitting of the upper level in the presence of a magnetic field gradient.

where the dumping coefficient β is given by the Eq. A.31 and the spring constant is

$$\kappa = \frac{\mu b}{\hbar k}\beta. \tag{A.42}$$

For typical magnetic field gradients $b \approx 10$ G/cm, harmonic motion of atoms is overdumped (damping rate $\beta/m > 1$).

A.4.1 Density and Velocity Distribution in MOT

Consider a non-interacting 1-D gas of particles of mass m characterized by a distribution function $f(r, v, t)$ in the phase space. The gas is subjected to a conservative force $F = F(r, t)$. The Boltzmann's equation $df = 0$ in a steady-state $\partial f/\partial t$ will be

$$v\frac{\partial f}{\partial r} + \frac{F}{m}\frac{\partial f}{\partial v} = 0,$$

or, expressing the force as a gradient of a potential U, the last equation will be

$$v\frac{\partial f}{\partial r} - \frac{1}{m}\frac{\partial U}{\partial r}\frac{\partial f}{\partial v} = 0, \tag{A.43}$$

with the solution

$$f(r,v) = f_0 e^{-\beta U(r)}\, e^{-\beta\frac{mv^2}{2}}, \tag{A.44}$$

where β is the equilibrium temperature of the Maxwellian velocity distribution, and f_0 is the normalization constant. For a cloud trapped in a harmonic oscillator potential with a spring constant k, $U(r) = -kr^2/2$, the spatial 1-D density distribution in the MOT is a Gaussian,

$$f(r) \propto e^{-r^2/2\sigma^2},$$

where the cloud size $\sigma = \sqrt{\beta k}$.

If the MOT, initially characterized by a Gaussian density and Maxwellian velocity distribution at $t = 0$, starts evolving freely ($U(r) = 0$), the corresponding Boltzmann's equation,

$$\frac{\partial f}{\partial t} + v\frac{\partial f}{\partial r} = 0,$$

has a partial solution $f(t,r) = e^{-r^2/\sigma^2(t)}$, where the cloud size, $\sigma(t) = \sqrt{\sigma^2(0) + v^2t^2}$, ballistically expands in time.

A.5 Dipole Force

The first term in the Eq. A.19 is proportional to the gradient of the electric field amplitude. This force is called the dipole (or stimulated) force and is usually expressed as a gradient of a potential

$$U = \frac{\hbar\delta}{2}\ln\left[1 + \frac{s_0}{1 + (2\delta/\gamma)^2}\right], \tag{A.45}$$

where the sign of the detuning δ determines if the dipole potential is repulsive ($\delta < 0$) or attractive ($\delta > 0$), while the spatial variation of the light intensity, $s_0 = I(\boldsymbol{r})/I_s$ sets the shape of the potential. Note that the dipole force is conservative and due to the absorption and the consecutive stimulated emission. The original derivation of the Eq. A.45 can be found in Ref. [115].

Appendix B

Appendix B. Elements of the Scalar Diffraction Theory

Appendix B is devoted to the scalar diffraction theory applied to the generation of the non-diffracting beams.

B.1 Nondiffracting Solutions of Wave Equation

We look for monochromatic solutions of the scalar wave equation in free space

$$\left(\nabla^2 - \frac{1}{c^2}\frac{\partial^2}{\partial t^2}\right) E(\boldsymbol{r}, t) = 0, \tag{B.1}$$

which represent nondiffracting wavefields, whose corresponding intensity distribution have the property that

$$I(x, y, z \geq 0) = I(x, y, 0), \tag{B.2}$$

along the propagation direction z.

The wave equation can be reduced to the two-dimensional Helmholtz equation if we consider solutions of frequency ω in the form

$$E(\boldsymbol{r}, t) = U(x, y)Z(z)e^{-i\omega t}, \tag{B.3}$$

such that $|Z|$ is independent of z to satisfy relation (B.2).

Consecutively, we obtain

$$\frac{d^2Z}{dz^2} + \beta^2 Z = 0, \tag{B.4}$$

for the longitudinal direction, and

$$\left(\nabla_\perp^2 + \alpha^2\right) U(x,y) = 0, \tag{B.5}$$

transverse plane accordingly. There, $\alpha^2 + \beta^2 = k^2 = (\omega/c)^2$, and $\nabla_\perp^2 = \partial^2/\partial x^2 + \partial^2/\partial y^2$.

We limit the family of solutions of Eq. (B.4) along the propagation direction by the Sommerfeld radiation condition to find

$$Z(z) = Ce^{i\beta z}, \tag{B.6}$$

where C is a constant, and β is real and positive to satisfy the condition (B.2).

The solution for the Eq. (B.5) can be written in an integral form [116] as

$$U(x,y) = \int_0^{2\pi} F'(u) e^{i\alpha(x\,cos\,u + y\,sin\,u)} du, \tag{B.7}$$

where F' is an arbitrary complex function of a real parameter $u = [0..2\pi]$.

We can re-write the wave equation nondiffracting solution (B.3) as

$$E(\boldsymbol{r},t) = e^{i(\beta z - \omega t)} \int_0^{2\pi} F(u) e^{i\alpha(x\,cos\,u + y\,sin\,u)} du, \tag{B.8}$$

where $F(u)$ is an arbitrary and well-behaved complex function. The nondiffracting wave field of this type were originally introduced by Durnin [117]. For a special case of $F(u) = exp\,(in\,u)$[1], we obtain an axially symmetric solution with the transverse profile given by a nth-order Bessel function of the first kind

$$E(\boldsymbol{r},t) = 2\pi e^{i(\beta z - \omega t)} J_n(\alpha\rho), \tag{B.9}$$

where $\rho^2 = x^2 + y^2$.

[1]If we treat the parameter u as a polar angle of the cylindrical coordinate system.

It is impossible to produce an ideal Bessel beam since the wave field (B.9) carries the infinite amount of energy. One, however, can create such a beam over a finite area: we will show that the finite-aperture approximation of a wave field with a Bessel transverse profile similar to Eq. B.9 can be generated from a collimated laser beam with a help of single hologram[118]. Consider a unit-amplitude plane wave illuminating a thin circular finite-size hologram of radius r_0 characterized by the following transmission function

$$T(r,\phi,0) = \begin{cases} e^{in\phi}e^{-ik_r r} & r \le r_0, \\ 0 & r > r_0, \end{cases} \tag{B.10}$$

where (r,ϕ) are the polar coordinates in the plane $z = 0$ of the hologram, and k_r is a radial spatial frequency.

The wave field behind the hologram is given by the Kirchhoff integral in the Fresnel approximation

$$U(r,\phi,z) = \frac{1}{i\lambda z}e^{ik(z+\frac{r^2}{2z})}\int_0^{r_0} r' e^{ik\frac{r'^2}{2z}}\left[\int_0^{2\pi} T(r',\phi',0)e^{-i\frac{krr'\,cos(\phi'-\phi)}{z}}d\phi'\right]dr'. \tag{B.11}$$

Substituting the transmission function (B.10) into the last equation and evaluating the angular integral yields

$$U(r,\phi,z) = \frac{2\pi}{\lambda z}e^{ik(z+\frac{r^2}{2z})}e^{in\phi}\int_0^{r_0} r' J_n(\frac{krr'}{z})exp\left[i\left(\frac{kr'^2}{2z} - k_r r'\right)\right]dr'. \tag{B.12}$$

The radial integral can be evaluated using the principle of the stationary phase [119]. Omitting the position-independent factors, intensity distribution behind the hologram in the observation plane z = constant is given by [118]

$$I(r,\phi,z) \propto |e^{in\phi}J_n(k_r r)|^2, \tag{B.13}$$

or in Cartesian coordinates

$$I(x,y,z) \propto |\int_0^{2\pi} e^{in\phi} e^{ik_r(x\,cos\,\phi + y\,sin\,u\phi)} d\phi|^2, \tag{B.14}$$

similar to the intensity distribution of the nondiffracting solution (B.7) of the wave equation when $k_r = \alpha$ is the radial spatial frequency of the Bessel wave, and $F'(\phi) = e^{in\phi}$, which is the hologram transmission function.

The finite aperture of the holographic element results in a finite propagation-invariant distance while the ideal Bessel beam is invariant in propagation. The maximum propagation-invariant distance derived from geometric optics is given by

$$z_{max} = \frac{1}{k_r}\frac{\pi D}{\lambda}, \tag{B.15}$$

where D is the diameter of the hologram and λ is the wavelength of light.

A hologram transmission function (B.10) can be realized as a circular wedged dielectric disk whose optical thickness is $(-k_r r + n\phi)$ in polar coordinates. Practically, it is convenient to adjust the phase by a 2-dimensional spatial light modulator, which acts as a holographic phase mask generated by a computer. Application of this technique is described in Chapter 3.

Appendix C

Appendix C. Apparatus for Bessel Beam Experiment

Appendix C is devoted to the descriptions of the experimental apparatus assembled for the Bessel beam experiment. The apparatus includes a laser-cooling machine to produce cold rubidium clouds and the setup to generate the Bessel beams that were applied to manipulate the atomic clouds. We include the names of manufacturers and model numbers for various devices constituting the experimental setup.

C.1 Magneto-optical Trap Setup

As we show in Chapter 3, we can generate Bessel beams with corresponding optical potentials of a few hundred microkelvins. Such potentials are high enough to confine atoms cooled and trapped in a standard magneto-optical trap (MOT). The basic ideas of laser cooling and trapping in a MOT are discussed in Appendix A. Below we provide the details of our realization of the MOT.

When the MOT loading is stopped, the cloud life-time and therefore the accessible time of the experiment is determined by the collisions with the background gas, which is at room temperature. Therefore a cold atom experiment needs to be conducted under high vacuum. The required pressure in a vacuum chamber is set by the desired time of the experiment after the MOT loading stage (a few hundred milliseconds), which corresponds to $p \sim 10^{-8}$ Torr of rubidium vapor pressure. To reach this pressure we assembled a stainless steel chamber with several glass

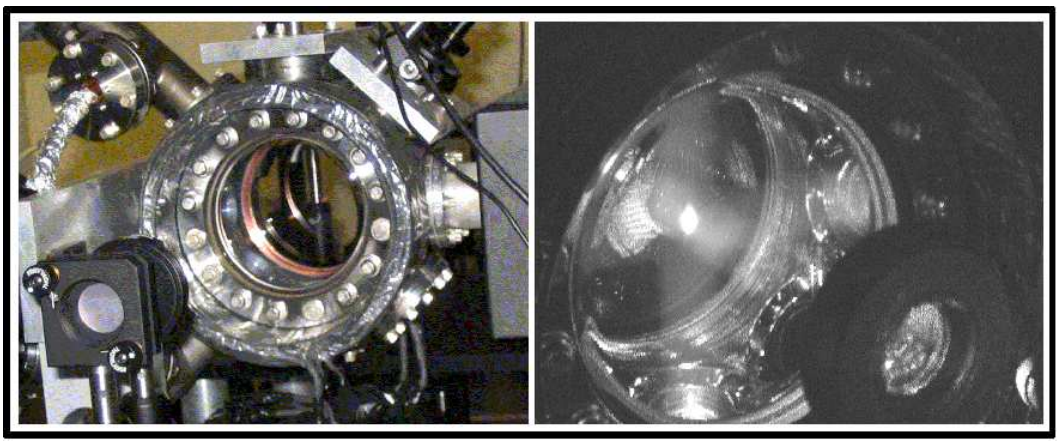

Figure C.1: Stainless steel vacuum chamber for laser-cooling and guiding rubidium atoms (left). Fluorescence of the cooling laser beams and the MOT in the chamber is shown on the right.

windows to provide optical access of the cooling laser light to the atomic vapor. The chamber consisted of a spherical octagon ultra-high vacuum chamber from Kimball Physics that has two 6" and eight 2 3/4" conflat flanges. The 6"-flanges were sealed by two uncoated glass viewports, one 2 3/4" flange was used to connect the chamber to a 40 l/s ion pump (Varian Starcell), and two more were extended by conflat tees. The rest of the open 2 3/4" flanges were sealed by glass windows anti-reflection coated for 780 nm. A part of the chamber is presented in Fig. C.1 (left image) along with a photograph of a MOT cloud collected at the intersection of the six cooling laser beams. After the vacuum chamber was sealed, it was evacuated by a turbo pump (Pfeiffer TPH170) to about 10^{-7} Torr and pumped down below 10^{-8} Torr by the ion pump. The low pressure in the chamber was maintained by the ion pump alone from that moment on, and the value of the pressure was measured by the ion pump current.

To simplify the experimental setup we loaded the MOT from rubidium vapor [120]. As a source of atoms, we used a glass ampule with rubidium placed in a 4-mm inner diameter copper tube. One end of the tube was pinched off and thus vacuum sealed, while the other end was welded to a copper gasket, which sealed

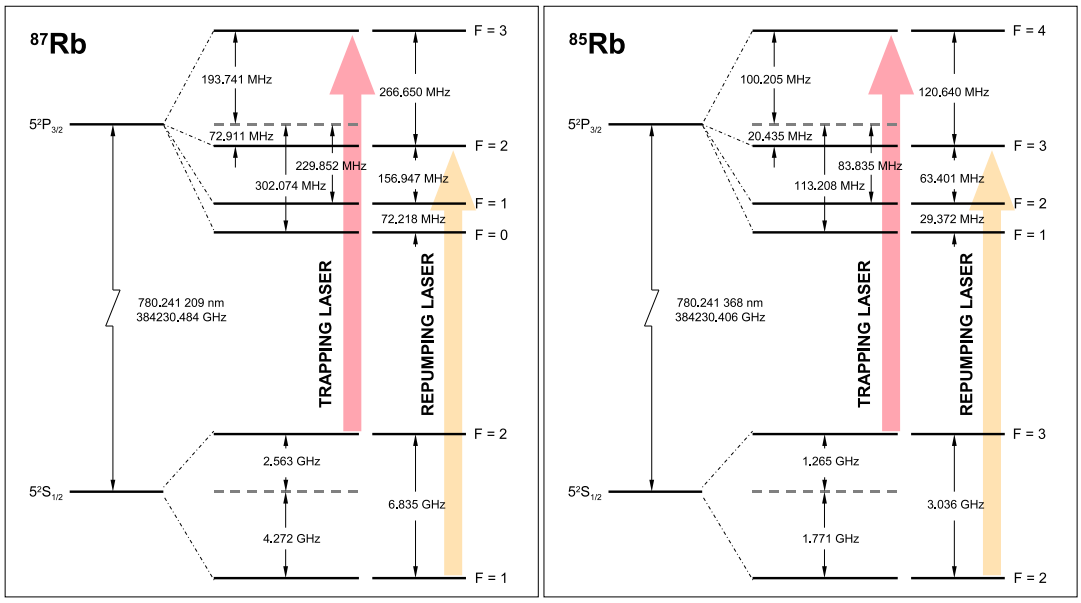

Figure C.2: Hyperfine level structure of the ground and the first excited states of ^{87}Rb (left) and ^{85}Rb (right) showing the corresponding frequencies of the trapping and the re-pumping lasers. Adopted from reference [121]

the connection between the chamber and an stainless steel end cap with an on-axis hole. The tube - aluminum foil wrapped finger - can be seen in the left top corner of Fig. C.1. As the base pressure in the chamber was reached, the rubidium ampule was cracked by bending the tube. The tube was equipped with a heater to evaporate atoms into the chamber as needed to maintain the rubidium vapor pressure of 10^{-8} Torr[1].

The laser cooling light was provided by two diode lasers at 780 nm. The hyperfine structure of rubidium $5s$ and $5p$ levels is shown in Fig. C.2.

The $5s_{1/2}|\, F = 2\,\rangle \rightarrow 5p_{3/2}|\, F' = 3\,\rangle$ transition from the ground state to the first excited state was chosen as the cycling cooling transition and was driven by a frequency-stabilized diode laser (Toptica, DL100). As required by the laser cooling mechanism, the laser frequency was about 20 MHz red-detuned from the atomic

[1]Rubidium saturated vapor pressure at room temperature is $2 \cdot 10^{-7}$ Torr

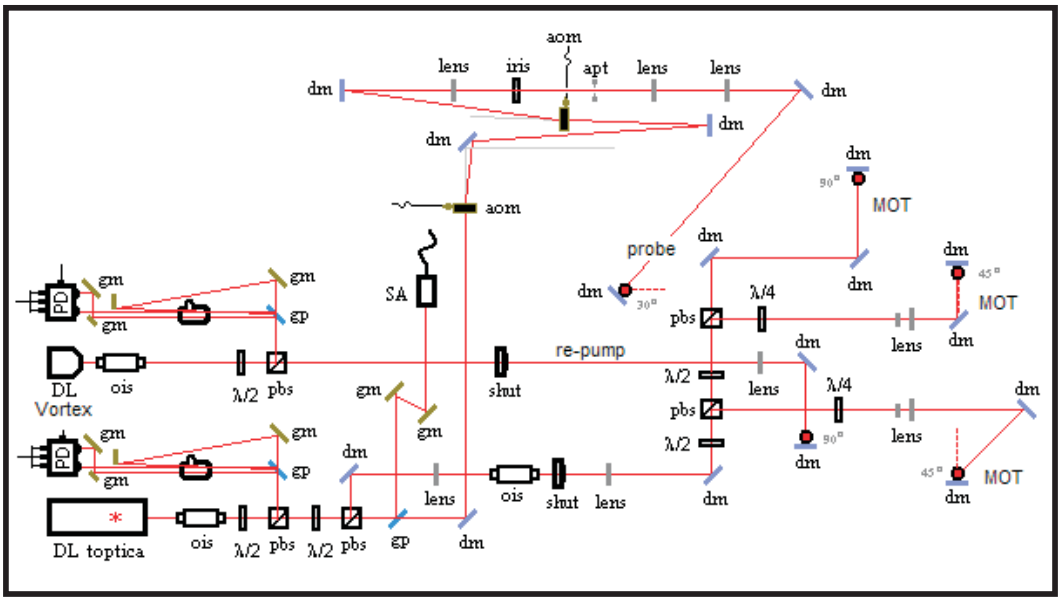

Figure C.3: Layout of the optical system for the laser cooling setup. Two frequency stabilized diode lasers were used to provide six cooling and trapping beams, and a probe (Toptica), and repumping beam (Vortex).

transition. Since the atoms may decay into $5s_{1/2}|\, F = 1\,\rangle$ state from the excited state, they were re-pumped back to the cooling cycle by the second stabilized diode laser (New Focus, Vortex 6000 series) driving the $5s_{1/2}|\, F = 1\,\rangle \rightarrow 5p_{3/2}|\, F' = 2\,\rangle$ transition. The energy difference between the cooling and the repumping transition larger than 8 GHz required the usage of two separate lasers.

The cooling and the repumping light was delivered to the chamber as shown on the optical layout in Fig. C.3. The Toptica DL100 laser produced 90 mW of power. The laser was separated from the rest of the experiment by an external optical isolator (OI) of 32 dB isolation (Isowave, I-80-T5-H) to prevent possible optical feedback to the laser that might disturb the laser oscillations. Several milliwatts were sent to a saturated absorption spectroscopy setup that provided a marker to stabilize the laser frequency. Another 2-3 mW of power were used to generate a probe beam for the absorption imaging of the $5s_{1/2}|\, F = 2\,\rangle$ ground state popula-

tion[2]. To maximize the absorption by a low density cloud the probe beam needs to be on resonance with an atomic transition (*e.g.*, $5s_{1/2}|\, F = 2\,\rangle \rightarrow 5p_{3/2}|\, F' = 3\,\rangle$). As the frequency of the Toptica beam was detuned about 20 MHz below the transition, two acousto-optical modulators (AOM) (Isomet, 1205C-2-804B) were employed to shift the frequency to resonance. Each AOM was characterized by a central frequency of 80 MHz and the bandwidth of 30 MHz; the first AO was driven at 70 MHz, its negative first diffraction output order coupled with the second AOM driven at 90 MHz. Thus the frequency of the first order of the second AOM output was upshifted by 20 MHz with respect to the original Toptica beam and resonant with the cooling transition. The transverse intensity profile of the first order was cleaned by a spatial filter, the beam diameter increased to 1 cm by a telescope consisted of two spherical lenses, and the resulting beam was applied as the probe beam of the shadow imaging technique.

The main Toptica beam was divided into three independent beams by a combination of a half-wave plate and a polarizing beam splitting cube, each beam expanded to a 2 cm diameter. The beams were properly circularly polarized by quarter-wave plates, crossed at 90° with respect to each other in the center of the vacuum chamber. Each beam was then retro-reflected to counter-propagate itself inside the chamber thus forming six molasses beams (Fig. C.3, right). The cooling beams were switched on and off by a mechanical shutter (Uniblitz, LS6 T2) in 1.7 ms. The appropriate magnetic field gradient inside the chamber was provided by two sets of coils with electric current in anti-Helmholtz configuration. Each coil consisted of 42 loops of hollow copper refrigeration tubing wound around the large 6" window of the vacuum chamber. The coils were arranged such that the magnetic field in the center of the chamber was zero and increased linearly away from the center of the chamber with the gradient of 15 G/cm at the current of 25 A. The heat produced by the current was dissipated by water running inside the

[2]The basics of the absorption imaging are described in Appendix A

copper tubing.

The re-pumping beam was provided by the 5 mW Vortex diode laser. The laser was separated from the rest of the setup by an optical isolator (Isomet, 1205C-2-804B). A part of the beam was sent to the saturated absorption spectroscopy setup to stabilize the laser frequency. The main Vortex beam of about 3 mm in diameter was aligned with the intersection region of the cooling beams.

In order to stabilize a laser one has to establish a one-to-one correspondence between its frequency and a voltage generated by a device external to the laser. Spectroscopy of a medium absorbing light at the wavelength of interest provides frequency markers that are independent of the environmental conditions and repeatable. As our lasers had to be frequency-stabilized close to atomic transitions in rubidium we used the appropriate spectroscopic features to establish the frequency-voltage correspondence. A saturated rubidium vapor in a glass cell is characterized by a Doppler-broadened absorption profile of a gigahertz as atoms from each velocity class are detuned differently from the resonant frequency of a stationary atom. Such profile does not provide enough resolution to keep the laser frequency stable within a linewidth of an atomic transition of several megahertz. A narrow atomic transition can be resolved by a Doppler-free saturated absorption spectroscopy. Consider two laser beam at the same frequency, one above (pump) and the other below (probe) the saturation intensity, counter-propagating in a Rb glass cell such that the power of the weaker beam is detected by a photodiode. The photodiode current proportional to the probe beam power is converted to a voltage signal. If the laser frequency is detuned (within the Doppler profile) with respect to resonance of the stationary atom, the probe beam is resonant with a certain velocity class and partly absorbed by the media, while the pump beam is resonant with the opposite velocity class. As the laser detuning is zero (within the linewidth of the laser), both beams are interacting with the same zero-velocity class, the high intensity pump beams saturates the atomic transition, and the low intensity probe is not absorbed by the medium any more producing a sharp dip in the Doppler

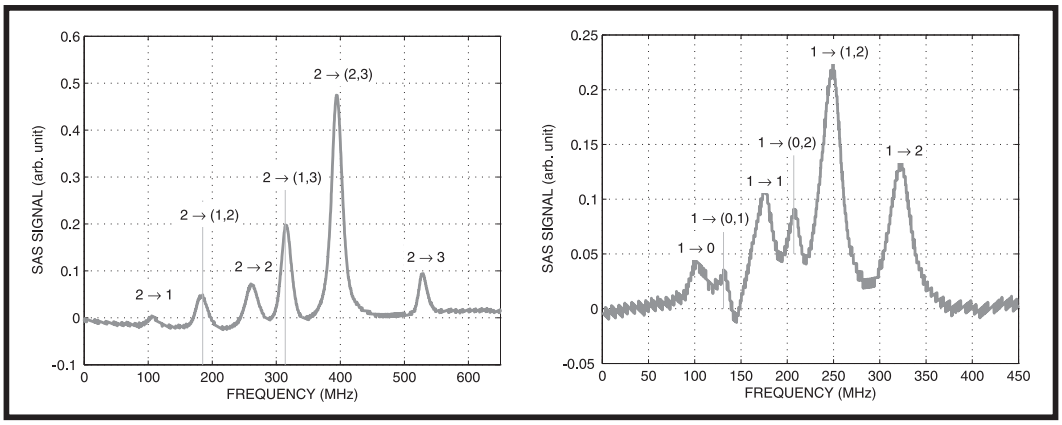

Figure C.4: Saturated absorption spectroscopy of $5s_{1/2}|\,F=2\,\rangle \rightarrow 5p_{3/2}|\,F'\,\rangle$ (left) and $5s_{1/2}|\,F=1\,\rangle \rightarrow 5p_{3/2}|\,F'\,\rangle$ (right) transitions. Cross-over peaks (denoted by excited state quantum numbers in round brackets) do not correspond to real atomic transitions. They are due to a reduced absorption of the probe beam when the laser frequency is tuned to the middle between two atomic transitions. There, both the probe and the pump interact with the same velocity classes but excite them to different atomic transitions thus suppressing absorption of the weak probe. The $(2 \rightarrow 3)$ and $(1 \rightarrow 2)$ peaks were used as the frequency markers to stabilize the cooling and the re-pumping lasers accordingly.

absorption profile of the probe beam. Another weak laser beam at the same frequency, not overlapped with the probe or the pump can be sent through the cell and detected by a second photodiode. Further subtraction of the two photodiode signals leaves only the peak at the resonance frequency of the stationary atom. The spectroscopy of the $5s_{1/2}|\,F=2\,\rangle \rightarrow 5p_{3/2}|\,F'\,\rangle$ and $5s_{1/2}|\,F=1\,\rangle \rightarrow 5p_{3/2}|\,F'\,\rangle$ transition is presented on the left and right of Fig. C.4 correspondingly.

For example, the frequency of the cooling laser has to be a few linewidths below the frequency of the atomic transition, and on the slope of the $|\,F=2\,\rangle \rightarrow |\,F'=3\,\rangle$ peak in Fig. C.4. That frequency corresponds to a certain *set-point* voltage; a small change in the laser frequency changes the absorption of the medium and results in a different voltage generated from the photodiode in accordance with the absorption

profile. If the difference between the read-out voltage from the photodiode and the set-point voltage (*error signal*) is properly fed-back to the laser, it forces the latter to change its frequency back to the desired value corresponding the set-point voltage. Thus the difference between the read-out and the set point stays zero keeping the laser frequency stabilized even if the properties of the environment (temperature, acoustic noise, *etc.*) are changing. We achieved the stabilization by a servo loop, which circuit diagram is presented in Fig. C.5. The voltage difference between the two photodiodes is subtracted from the set point voltage, the result integrated, amplified, and fed back to the laser system electronics. The internal cavity of the laser diode is extended by a diffraction grating; the first order is diffracted of the grating back to the diode thus setting the oscillating frequency of the laser within its gain profile. The variable tilt of the grating allows continuous tuning of the laser's wavelength and is practically realized by a piezoelectric transducer (PZT). The signal from the servo loop, when added to the bias voltage of the PZT, provides the stabilization of the laser frequency at the given set point voltage. The tuning of the laser frequency within the slope of a spectroscopic feature can be achieved by the appropriate adjustment the set point voltage. As the laser frequency in controlled by a mechanical motion of the grating, the bandwidth of the feedback control is limited by a few kilohertz, still large enough to compensate for slow thermal effects and the acoustic noise. Faster Fourier components in the laser frequency spectrum can be suppressed by feeding back the error signal to the driving current of the laser diode, effectively reducing the linewidth of the laser.

Practically, we frequency-stabilized the Vortex laser by locking the corresponding photodiode signal on the side of the $|\, F = 1 \,\rangle \rightarrow |\, F' = 2 \,\rangle$ (re-pump) peak in Fig. C.4 using the circuit diagram in Fig. C.5. The cooling laser was stabilized on the side of the $|\, F = 2 \,\rangle \rightarrow |\, F' = 3 \,\rangle$ peak in Fig. C.4 using a commercial locking circuit (Toptica, PID 100).

With the magnetic field on and the frequency of the cooling and the repumping

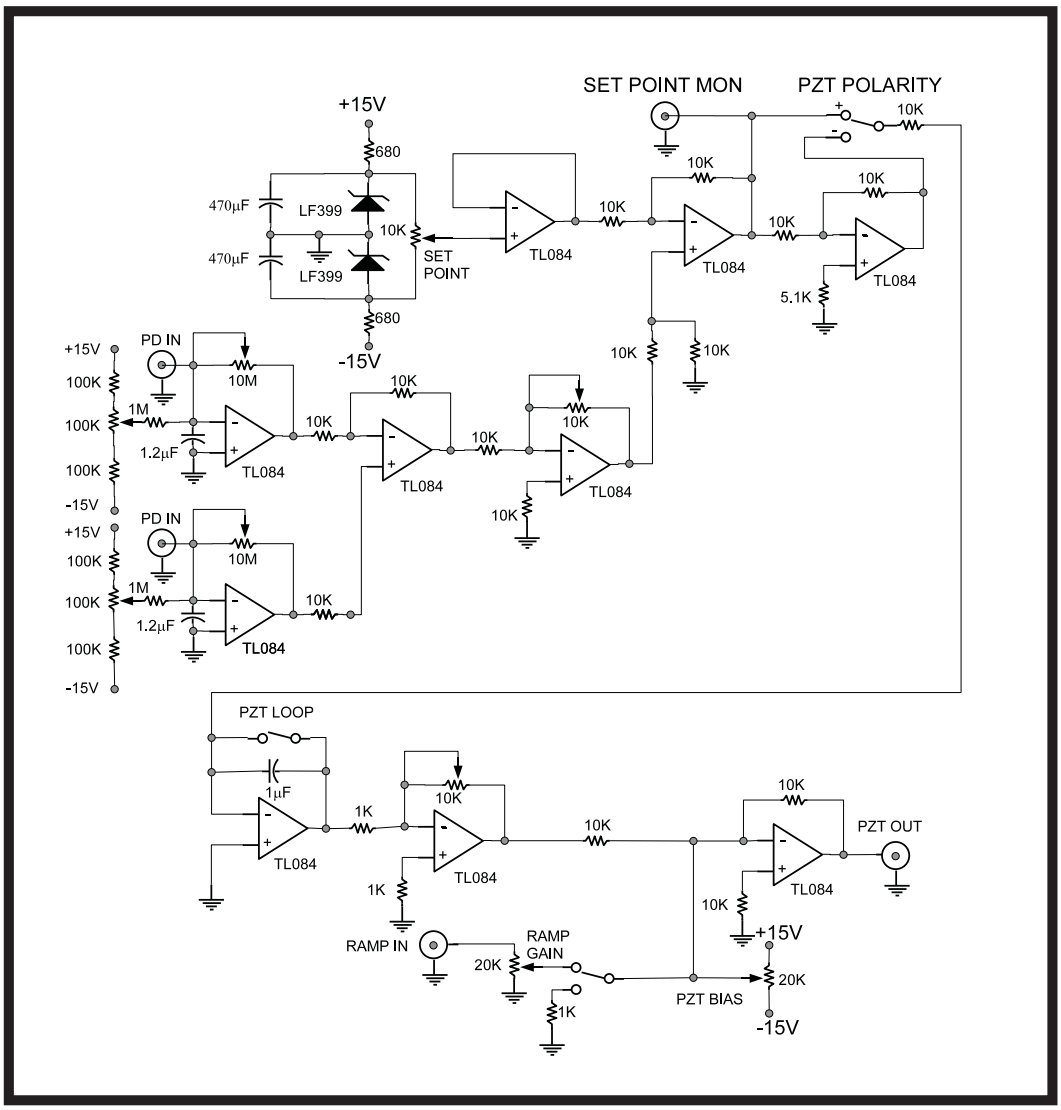

Figure C.5: The diagram of the locking circuit used to stabilize the re-pump laser on the slope of the spectroscopic feature of the $5s_{1/2}|\, F = 1\,\rangle \rightarrow 5p_{3/2}|\, F'\,\rangle$ transition with the values of passive and the part numbers for active elements of the circuit.

lasers stabilized, the rubidium cloud was collected at the intersection region of cooling lasers. The fluorescence of the MOT cloud and cooling beams (photons spontaneously emitted by excited atoms decaying into the ground state) is shown in Fig. C.1, photograph on the right. The steady-state number of atoms in the MOT

was estimated to be about 10^8 using the fluorescence signal from the MOT cloud. The spontaneously emitted photons from the fluorescent cloud were collected on an active area of a power meter by a high numerical aperture imaging system. The measured power is proportional to the number of photons emitted into the solid angle enclosed by the imaging system, and thus determines the number of emitters (atoms) via the scattering rate at the known detuning. This estimated number was used to calibrate shadow imaging signal - our primary detection method. The beam after the absorption by the cold atom cloud is projected onto a charge-coupled device (CCD) array of a 8-bit video camera (COHU, 4910) by a spherical lens that provides one-to-one imaging of the cloud on the plane of the CCD. The CCD array area was 4 x 6 mm with the resolution of 480 by 752. The analog signal from the camera was sent to a computer and digitized by a frame grabber card (PIXCI, SV4). The resulting digital image provided the information on the atom number, cloud size in the direction transverse to the probe beam and the cloud position with respect to the probe beam. Practically, the magnification of the imaging system is unknown and needs to be calibrated to the known size of the CCD array. That was done by imaging the cloud free fall in the gravity field and tracking the postion of the cloud's center of mass on the CCD array at various fall times. The cloud temperature defined in Appendix A, can be estimated from the cloud's free expansion. The linear size of the cloud σ along a specific direction as measured by the shadow imaging after a certain expansion time t is given by $\sigma^2(t) = \sigma_0^2 + v^2t^2$, where σ_0 is the initial size of the cloud, and v^2 is the mean square velocity of the Maxwellian distribution. As σ^2 grows linearly with t^2, the slope of this dependence gives v^2. Assuming anisotropic expansion, the equipartition theorem, $1/2k_BT = 1/2mV^2$, allows the expression of the value of the kinetic energy in units of temperature T; there k_B is the Boltzmann's constant, m is the mass of the rubidium atom. Generally, the cloud can be characterized by three values of temperature according to its expansion along three perpendicular directions if imaged by two orthogonal probe beams. A typical single MOT temperature for

our experiments was measured to be $(250 \pm 15)\ \mu K$.

Appendix D

Appendix D. Rydberg Experiment

D.1 Autler-Townes Splitting in 3-level Atom

According to the Wiener-Khinchine theorem, the spectrum of a steadily oscillating system can be found from the Fourier transform of the corresponding autocorrelation function. For an atomic system, the relative quantity is the dipole moment autocorrelation function,

$$G(\tau) = \left\langle \hat{d}(\tau)\, \hat{d}(0) \right\rangle .$$

In the Schödinger picture, the state vectors embody the time dependence, and the autocorrelation can be written as

$$G(\tau) = \left\langle e^{iH\tau/\hbar}\, \hat{d}\, e^{-iH\tau/\hbar}\, \hat{d} \right\rangle .$$

If an atom initially, at $t = 0$, is in the pure quantum state Ψ, the dipole autocorrelation function read

$$G(\tau) = \left\langle \Psi(\tau) | \hat{d} e^{-iH\tau/\hbar}\, \hat{d} | \Psi(0) \right\rangle . \tag{D.1}$$

The last expression can be treated as a matrix element

$$G(\tau) = \left\langle \Psi(\tau) | \hat{d} | \Phi(t) \right\rangle ,$$

where states $\Phi(t)$ and $\Psi(t)$ are each solutions to the same time-dependent Schödinger equation, but they evolve from different initial conditions: the state $\Psi(t)$ starts

from the initial state ψ, while $\Phi(t)$ starts from the state produced from ψ by the action of the dipole moment, $\Psi(0) = \psi$, and $\Phi(0) = \hat{d}\psi$.

We can treat the exponential Hamiltonian by introducing a complete set of dressed eigenstates of the operator H,

$$(H - \hbar Z_k)\,\Phi_k = 0, \qquad \Phi_k(t) = e^{-iZ_k t}\,\Phi_k,$$

and Eq. D.1 will be

$$G(\tau) = \sum_k e^{-iZ_k\tau} \left\langle \Psi(\tau)|\,\hat{d}\,|\Phi_k \right\rangle \left\langle \Phi_k|\,\hat{d}\,|\Psi(0) \right\rangle. \tag{D.2}$$

Consider a 3-level system, where the Hamiltonian H strongly couples two states, and the third state, ψ_0 is weakly connected by a dipole transition to a dressed state. Then, the autocorrelation function for this transition will be

$$G(\tau) = \sum_{k=1,2} e^{-i\omega_{k0}\tau} \left| \left\langle \psi(0)|\,\hat{d}\,|\Phi_k \right\rangle \right|^2, \tag{D.3}$$

where ω_k are the transition frequencies from the weakly-coupled state.

The dressed states and their eigenvalues can be written in terms of the unperturbed states ψ_1 and ψ_2

$$\Phi_1 = cos\Theta\,\psi_1 - sin\Theta\,\psi_2 \qquad \Phi_2 = sin\Theta\,\psi_1 + cos\Theta\,\psi_2, \tag{D.4}$$

and

$$\hbar Z_1 = E_1^A - \hbar\Delta \qquad \hbar Z_2 = E_1^A - \hbar\Delta + \hbar\hat{\Omega},$$

where E_1^A is the energy of state psi_1, the generalized Rabi frequency $\tilde{\Omega} = \sqrt{\delta^2 + \Omega^2}$, Ω is the Rabi frequency of the dressed state, the dynamic Stark shift $2\Delta = \tilde{\Omega} + \delta$, and $tan(2\Theta) = -\Omega/\delta$, and δ is the laser detuning from the $\psi_0 \rightarrow \psi_1$ transition. There we assumed that the state ψ_0 is coupled only with the unperturbed state ψ_1. The normalized autocorrelation function will be

$$g(\tau) = \frac{G(\tau)}{G(0)} = cos^2\Theta \;\; e^{-i(\omega_1 0 - \Delta)\tau} + sin^2\Theta \;\; e^{-i(\omega_b - \Delta + \tilde{\Omega})\tau}. \qquad \text{(D.5)}$$

The normalized autocorrelation function is related to the normalized spectral distribution function as

$$F(\omega) = \frac{1}{2\pi} \int_{-\infty}^{+\infty} g^1(\tau) e^{i\omega\tau} d\tau.$$

For the autocorrelation function (D.5),

$$F(\omega) = cos^2\Theta \;\; f(\omega_b - \Delta) + sin^2\Theta \;\; f(\omega_b - \Delta + \tilde{\Omega}),$$

where $f(\omega)$ is the Dirac's delta-function[1]. The resulting spectrum comprises a pair of lines (the Autler-Townes doublet) in place of the single line that would occur in the absence of the strong interaction. When the dressing interaction is weak ($\Theta = 0$), the spectrum reduces to a single line at frequency ω_{10}. When the dressing interaction is resonant ($\Theta = \pi/2$), the doublet comprises two lines of equal intensity, separated by the Rabi frequency Ω.

D.2 Population Dynamics of Two-level System with Ionization Loss

Consider two-level system with the ground state population, N_g, excited state population, N_e. Population dynamics of the system is set an excitation rate, R, from the excited state to the ground state, de-excitation rate, γ_1, and an ionization rate of the excited state, γ_2. For simplicity, we assume $\gamma_1 = \gamma_2 \equiv \gamma$. The dynamics is schematically shown in Fig. D.1. The total number of atoms in the system is $N_0 = N_i + N_g + N_e$. We are interested in the loss of atoms due to ionization.

[1]Note, that the finite lifetime of an atomic level, τ_0, results in the Lorentzian line shape of the width of $1/\tau_0$. The Lorentzian spectral distribution function can be obtained by multiplying the autocorrelation function by the factor of $e^{-\tau/\tau_0}$.

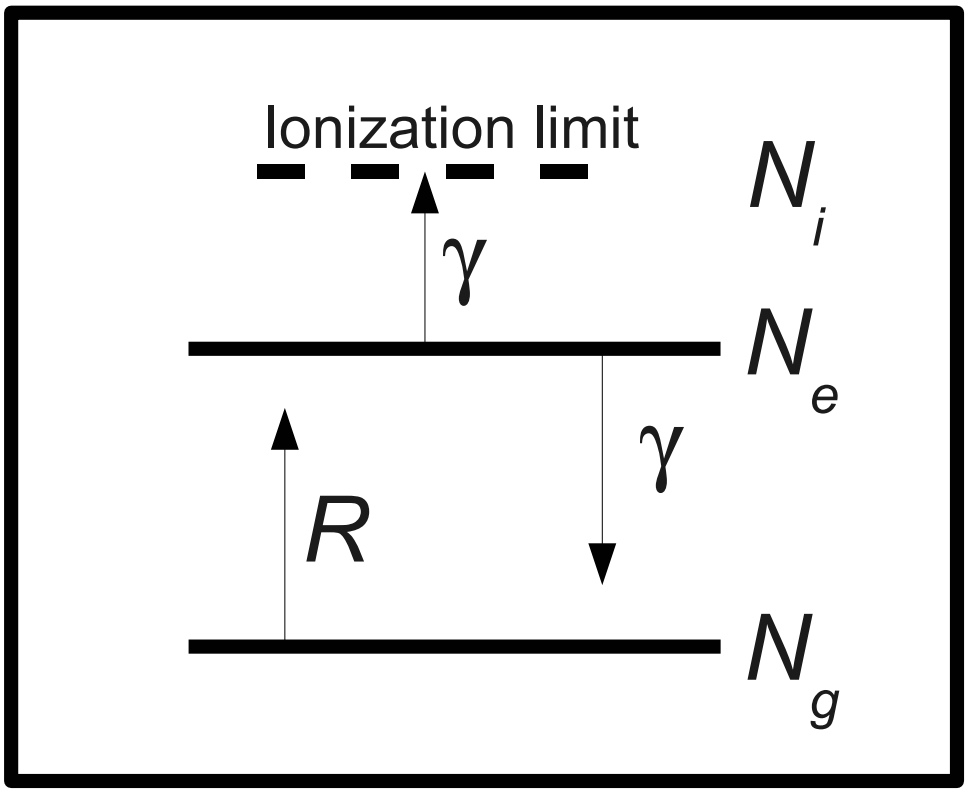

Figure D.1: Population dynamics of a two-level system with ionization loss

The corresponding rate equations are

$$\dot{N}_i = \gamma N_e$$

$$\dot{N}_e = RN_g - 2\gamma N_e$$

$$\dot{N}_g = -RN_g + \gamma N_e$$

And we look for the solutions in the form

$$N_e \sim e^{\lambda t},$$

which give rise to the following roots of the characteristic equation:

$$\lambda_{1,2} = \frac{-(2\gamma + R)}{2} \pm \frac{\sqrt{4\gamma^2 + R^2}}{2},$$

and for the case $R >> \gamma$,

$$\lambda_1 = -(\gamma + R), \qquad \lambda_2 = -\gamma,$$

an up to numerical constants C and D,

$$N_i = -\frac{\gamma C}{\gamma + R} e^{-(\gamma+R)t} + Ce^{-\gamma t} + D.$$

From the initial conditions, $C = N_0$ and $D = -R_R/(\gamma + R_R)$.

D.3 Stark Effect

In this section we numerically evaluate the energy shift of a Rydberg state of rubidium due to an external electric field. We first calculate the wavefunctions of Rydberg states. Electric field E will be considered as a perturbation and the new wavefunctions expanded in the basis of the eigenfunctions of the unperturbed Hamiltonian. The full Hamiltonian is given by

$$H = -\frac{\nabla^2}{2} + \frac{1}{r} + V_d(r) + Ez,$$

where $V_d(r)$ is the difference between the rubidium potential and the coulomb potential, $-1/r$. The eigenvalues of the unperturb Hamiltonian, $H_{E=0}$, are given by the quantum defect:

$$W = \langle\, nlm \,|\, H_{E=0} |\, nlm \,\rangle = \frac{1}{2(n - \delta_l)^2}.$$

As the Hamiltonian is given by the central potential, the separation of angular and radial coordinates is possible, and the radial part of the Schrödinger equation will be:

$$\frac{\partial^2 R}{\partial r^2} + \frac{2}{r}\frac{\partial R}{\partial r} + \left(2W + \frac{2}{r} - \frac{l(l+1)}{r^2}\right) R = 0,$$

where R is the radial wavefunction. The angular part of the wavefunction is give by the spherical harmonics of the hydrogenic atom Y_{lm} [122]. The substitution

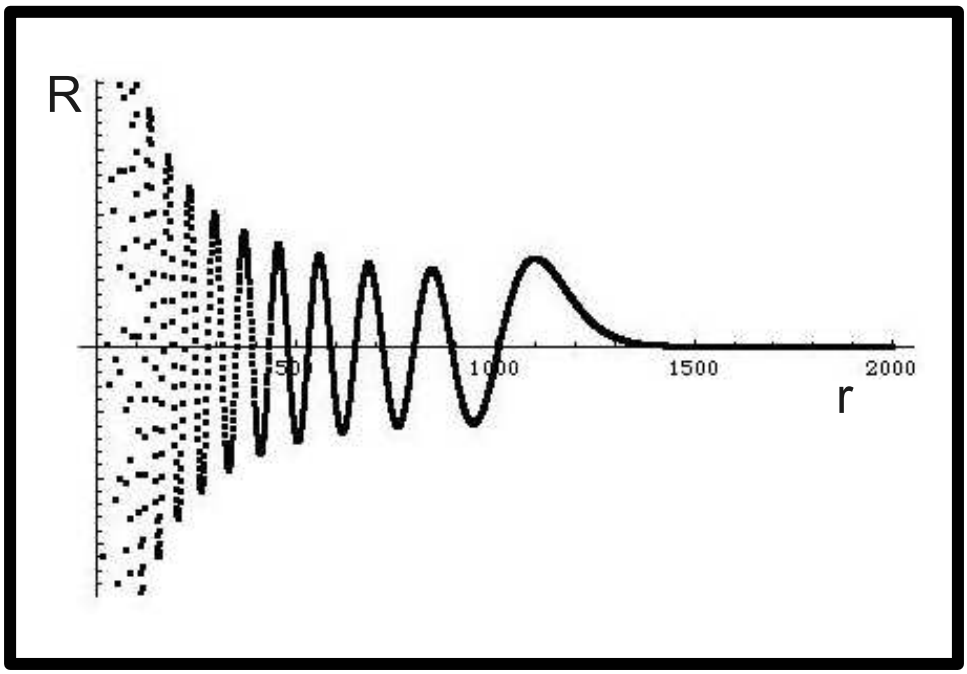

Figure D.2: Numerically calculated radial wavefunction of $50s_{1/2}$ state.

$x = \sqrt{r}, Y(x) = r^{3/4}R$ results in [123]

$$\left(-\frac{d^2}{dx^2} - 8Wx^2 + \frac{(2l+1/2)(2l+3/2)}{x^2}\right) Y = 8Y.$$

The last equation can be integrated numerically, and, as an example, the solution for $n = 50s$ is plotted in Fig. D.2.

In the presence of the electric field, the resulted Stark shift is given by

$$\Delta = \langle\, nlm \,|\, eEcos\theta |\, n'l'm' \,\rangle,$$

where $|\, nlm \,\rangle$ are the calculated unperturbed wavefunctions. The radial and angular parts of the expectation value can be evaluated numerically. The resulted Stark energy shift is presented in Fig. D.3 for $56s_{1/2}$ state. Note, that the effect is quadratic in the field at $E < 2$ V/cm and linear between 3 and 5 V/cm.

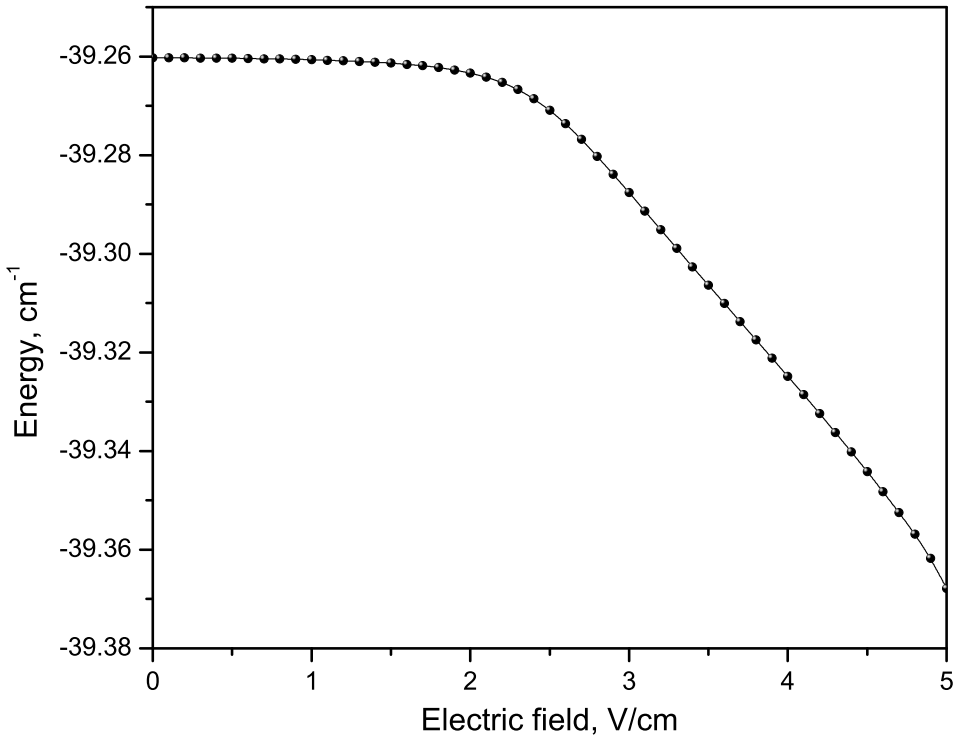

Figure D.3: The Stark effect for $56s_{1/2}$ state. The energy shift in quadratic in field at low fields, $E < 2$ V/cm and linear between 3 and 5 V/cm.

BIBLIOGRAPHY

[1] Stern O. Beugung von molekularstrahlen am gitter einer krystallspaltflache. *Naturwiss.*, **17**, 391, 1929.

[2] R.P. Feynmann. Quantum mechanical computers. *Found. Phys*, **16**(6), 507–531, 1986.

[3] A. M. Steane. Error correcting codes in quantum theory. *Phys. Rev. Lett.*, **77**(5), 793–797, 1996.

[4] Lov K. Grover. Quantum mechanics helps in searching for a needle in a haystack. *Phys. Rev. Lett.*, **79**(2), 325–328, 1997.

[5] Peter W. Shor. Polynomial-time algorithms for prime factorization and discrete logarithms on a quantum computer. *SIAM Journal on Computing*, **26**(5), 1484–1509, 1997.

[6] L. M. K. Vandersypen and I. L. Chuang. Nmr techniques for quantum control and computation. *Rev. Mod. Phys.*, **76**(4), 1037–1069, 2005.

[7] Pieter Kok, W. J. Munro, Kae Nemoto, T. C. Ralph, Jonathan P. Dowling, and G. J. Milburn. Linear optical quantum computing with photonic qubits. *Rev. Mod. Phys.*, **79**(1), 135, 2007.

[8] A.Imamoglu. Quantum computation using quantum dot spins and microcavities. *Fortschr. Phys.*, **48**(8), 987–997, 2000.

[9] J. I. Cirac and P. Zoller. Quantum computations with cold trapped ions. *Phys. Rev. Lett.*, **74**(20), 4091–4094, 1995.

[10] H. J. Briegel, T. Calarco, D. Jaksch, J. I. Cirac, and P. Zoller. Quantum computing with neutral atoms. *J. Mod. Opt.*, **47**(2), 415–451, 2000.

[11] N.F. Ramsey. *Molecular Beams*. Oxford University Press, London, first edition, 1956.

[12] Ch. J. Borde. Atomic interferometry with internal state labeling. *Physics Letters A*, **140**(1-2), 10 – 12, 1989.

[13] K. Bongs, S. Burger, S. Dettmer, D. Hellweg, J. Arlt, W. Ertmer, and K. Sengstock. Waveguide for bose-einstein condensates. *Phys. Rev. A*, **63**(3), 031602, 2001.

[14] Wolfgang Paul. Electromagnetic traps for charged and neutral particles. *Rev. Mod. Phys.*, **62**(3), 531–540, 1990.

[15] Joerge Schmiedmayer. A wire trap for neutral atoms. *Appl. Phys. B*, **60**(2-3), 169–179, 1995.

[16] Johannes Denschlag, Donatella Cassettari, and Jörg Schmiedmayer. Guiding neutral atoms with a wire. *Phys. Rev. Lett.*, **82**(10), 2014–2017, 1999.

[17] X. Luo, P. Krüger, K. Brugger, S. Wildermuth, H. Gimpel, M. W. Klein, S. Groth, R. Folman, I. Bar-Joseph, and J. Schmiedmayer. Atom fiber for omnidirectional guiding of cold neutral atoms. *Opt. Lett.*, **29**(18), 2145–2147, 2004.

[18] Dirk Müller, Dana Z. Anderson, Randal J. Grow, Peter D. D. Schwindt, and Eric A. Cornell. Guiding neutral atoms around curves with lithographically patterned current-carrying wires. *Phys. Rev. Lett.*, **83**(25), 5194–5197, 1999.

[19] P. G. Petrov, S. Machluf, S. Younis, R. Macaluso, T. David, B. Hadad, Y. Japha, M. Keil, E. Joselevich, and R. Folman. Trapping cold atoms using surface-grown carbon nanotubes. *Phys. Rev. A*, **79**(4), 043403, 2009.

[20] Donatella Cassettari, Björn Hessmo, Ron Folman, Thomas Maier, and Jörg Schmiedmayer. Beam splitter for guided atoms. *Phys. Rev. Lett.*, **85**(26), 5483–5487, 2000.

[21] Y. Shin, C. Sanner, G. B. Jo, T. A. Pasquini, M. Saba, W. Ketterle, D. E. Pritchard, M. Vengalattore, and M. Prentiss. *Phys. Rev. A*, **72**, 021604, 2005.

[22] T. Schumm, S. Hofferberth, L.M. Andersson, S. Wildermuth, S. Groth, I. Bar-Joseph, J. Schmiedmayer, and P. Kruger. Matter-wave interferometry in a double well on an atom chip. *Nat. Phys.*, **1**, 57, 2005.

[23] Y. J. Wang, D. Z. Anderson, V. M. Bright, E. A Cornell, Q. Diot, T. Kishimoto, M. Prentis, R. A. Saravanan, S. R. Segal, and S. Wu. *Phys. Rev. Lett.*, **94**, 090405, 2005.

[24] A. Ashkin and J. M. Dziedzic. Optical levitation by radiation pressure. *Appl. Phys. Lett.*, **19**(8), 283–285, 1971.

[25] A. Ashkin, J. M. Dziedzic, J. E. Bjorkholm, and Steven Chu. Observation of a single-beam gradient force optical trap for dielectric particles. *Opt. Lett.*, **11**(5), 288, 1986.

[26] Shunichi Sato, Yasunori Harada, and Yoshio Waseda. Optical trapping of microscopic metal particles. *Opt. Lett.*, **19**(22), 1807, 1994.

[27] K Svoboda and S M Block. Biological applications of optical forces. *Annual Review of Biophysics and Biomolecular Structure*, **23**(1), 247–285, 1994.

[28] H. He, M. E. J. Friese, N. R. Heckenberg, and H. Rubinsztein-Dunlop. Direct observation of transfer of angular momentum to absorptive particles from a laser beam with a phase singularity. *Phys. Rev. Lett.*, **75**(5), 826–829, 1995.

[29] Emily Edwards. *Construction of Apparatus and First Experiments Investigating Dynamics of Bose-Einstein Condensates in Disordered Optical Lattices*. PhD thesis, University of Maryland, 2009.

[30] M. L. Citron, H. R. Gray, C. W. Gabel, and C. R. Stroud. Experimental study of power broadening in a two-level atom. *Phys. Rev. A*, **16**(4), 1507–1512, 1977.

[31] M. J. Renn, D. Montgomery, O. Vdovin, D. Z. Anderson, C. E. Wieman, and E. A. Cornell. Laser-guided atoms in hollow-core optical fibers. *Phys. Rev. Lett.*, **75**(18), 3253–3256, 1995.

[32] Fetah Benabid, J. Knight, and P. Russell. Particle levitation and guidance in hollow-core photonic crystal fiber. *Opt. Express*, **10**(21), 1195–1203, 2002.

[33] Michael J. Renn, Elizabeth A. Donley, Eric A. Cornell, Carl E. Wieman, and Dana Z. Anderson. Evanescent-wave guiding of atoms in hollow optical fibers. *Phys. Rev. A*, **53**(2), 648–651, 1996.

[34] Dirk Müller, Eric A. Cornell, Dana Z. Anderson, and Eric R. I. Abraham. Guiding laser-cooled atoms in hollow-core fibers. *Phys. Rev. A*, **61**(3), 033411, 2000.

[35] J. E. Bjorkholm, R. R. Freeman, A. Ashkin, and D. B. Pearson. Observation of focusing of neutral atoms by the dipole forces of resonance-radiation pressure. *Phys. Rev. Lett.*, **41**(20), 1361–1364, 1978.

[36] K. Szymaniec, H. J. Davies, and C. S. Adams. An atomic fountain guided by a far-off resonance laser beam. *EPL (Europhys. Lett.)*, **45**(4), 450–455, 1999.

[37] Laurence Pruvost, Dan Marescaux, Olivier Houde, and Hong Tuan Duong. Guiding and cooling of cold atoms in a dipole guide. *Opt. Comm.*, **166**(1-6), 199 – 209, 1999.

[38] Olivier Houde, Demascoth Kadio, and Laurence Pruvost. Cold atom beam splitter realized with two crossing dipole guides. *Phys. Rev. Lett.*, **85**(26), 5543–5546, 2000.

[39] R. Dumke, T. Müther, M. Volk, W. Ertmer, and G. Birkl. Interferometer-type structures for guided atoms. *Phys. Rev. Lett.*, **89**(22), 220402, 2002.

[40] J. P. Yin, W. J. Gao, and Y. F. Zhu. Generation of dark hollow beams and their applications. *Prog. Opt.*, **45**, 119, 2003.

[41] Takahiro Kuga, Yoshio Torii, Noritsugu Shiokawa, Takuya Hirano, Yukiko Shimizu, and Hiroyuki Sasada. Novel optical trap of atoms with a doughnut beam. *Phys. Rev. Lett.*, **78**(25), 4713–4716, 1997.

[42] Yu. B. Ovchinnikov, I. Manek, and R. Grimm. Surface trap for cs atoms based on evanescent-wave cooling. *Phys. Rev. Lett.*, **79**(12), 2225–2228, 1997.

[43] S Kulin, S Aubin, S Christe, B Peker, S L Rolston, and L A Orozco. A single hollow-beam optical trap for cold atoms. *J. Opt. B*, **3**(6), 353–357, 2001.

[44] M. D. Barrett, J. A. Sauer, and M. S. Chapman. All-optical formation of an atomic bose-einstein condensate. *Phys. Rev. Lett.*, **87**(1), 010404, 2001.

[45] M. Schiffer, M. Rauner, S. Kuppens, M. Zinner, K. Sengstock, and W. Ertmer. Guiding, focusing, and cooling of atoms in astrong dipole potential. *Appl. Phys. B*, **67**(6), 705–708, 1998.

[46] Jianping Yin, Yifu Zhu, Wonho Jhe, and Zuzhu Wang. Atom guiding and cooling in a dark hollow laser beam. *Phys. Rev. A*, **58**(1), 509–513, 1998.

[47] Y. Song, D. Milam, and W. T. Hill III. Long, narrow all-light atom guide. *Opt. Lett.*, **24**(24), 1805–1807, 1999.

[48] Xinye Xu, Kihwan Kim, Wonho Jhe, and Namic Kwon. Efficient optical guiding of trapped cold atoms by a hollow laser beam. *Phys. Rev. A*, **63**(6), 063401, 2001.

[49] Narupon Chattrapiban, Elizabeth A. Rogers, David Cofield, III Wendell T. Hill, and Rajarshi Roy. Generation of nondiffracting bessel beams by use of a spatial light modulator. *Opt. Lett.*, **28**(22), 2183–2185, 2003.

[50] Narupon Chattrapiban, Elizabeth A. Rogers, Ilya V. Arakelyan, Rajarshi Roy, and W. T. Hill, III. Laser beams with embedded vortices: Tools for atom optics. *J. Opt. Soc. Am. B*, **23**, 2006.

[51] Daniel Waltner, Martha Gutiérrez, Arseni Goussev, and Klaus Richter. Semiclassical mechanism for the quantum decay in open chaotic systems. *Phys. Rev. Lett.*, **101**(17), 174101, 2008.

[52] K. Bongs, S. Burger, S. Dettmer, K. Sengstock, and W. Ertmer. Manipulation of bose-einstein condensates by dipole potentials. *J. Mod. Opt.*, **47**(14/15), 2697, 2000.

[53] Z. T. Lu, K. L. Corwin, M. J. Renn, M. H. Anderson, E. A. Cornell, and C. E. Wieman. Low-velocity intense source of atoms from a magneto-optical trap. *Phys. Rev. Lett.*, **77**(16), 3331–3334, 1996.

[54] Min Yan, Jianping Yin, and Yifu Zhu. Dark-hollow-beam guiding and splitting of a low-velocity atomic beam. *J. Opt. Soc. Am. B*, **17**(11), 1817–1820, 2000.

[55] M. Rioux, P. A. Bélanger, and M. Cormier. High-order circular-mode selection in a conical resonator. *Appl. Opt.*, **16**(7), 1791–1792, 1977.

[56] V. Bagini, F. Frezza, M. Santarsiero, G. Schettini, and G.S. Spagnola. Generalized bessel-gauss beams. *J. Mod. Opt.*, **43**(6), 1155, 1996.

[57] J. Arlt and K. Dholakia. Generation of high-order bessel beams by use of an axicon. *Opt. Comm.*, **177**(1-6), 297 – 301, 2000.

[58] J. Durnin, J. J. Miceli, and J. H. Eberly. Diffraction-free beams. *Phys. Rev. Lett.*, **58**(15):1499–1501, 1987.

[59] I. Khoo and S. Wu. *Optics and Nonlinear Optics of Liquid Crystals*, pages 1–6, 269–286. Utopia, Singapore, 1993.

[60] Narupon Chattrapiban. *Dynamics of an atomic ensemble in a single Bessel tunnel*. PhD thesis, University of Maryland, 2010.

[61] Grimm R., Weidemuller M., and Ovchinnikov Yu. Optical dipole traps for neutral atoms. *Adv. At. Mol. Opt. Phys.*, **42**, 95–170, 2000.

[62] D. E. Miller, J. R. Anglin, J. R. Abo-Shaeer, K. Xu, J. K. Chin, and W. Ketterle. High-contrast interference in a thermal cloud of atoms. *Phys. Rev. A*, **71**(4), 043615, 2005.

[63] V. Milner, J. L. Hanssen, W. C. Campbell, and M. G. Raizen. Optical billiards for atoms. *Phys. Rev. Lett.*, **86**(8), 1514–1517, 2001.

[64] N Friedman, A Kaplan, D Carasso, and N Davidson. Observation of chaotic and regular dynamics in atom-optics billiards. *Phys. Rev. Lett.*, **86**(8), 1518–1521, 2001.

[65] M.A. Nielsen and I.L. Chuang. *Quantum Computation and Quantum Information*. Cambridge University Press, Cambridge, first edition, 2000.

[66] D.P. DiVincenzo. The physical implementation of quantum computation. *Fortschr. Phys.*, **48**(9), 771–783, 2000.

[67] D. Jaksch, H.-J. Briegel, J. I. Cirac, C. W. Gardiner, and P. Zoller. Entanglement of atoms via cold controlled collisions. *Phys. Rev. Lett.*, **82**(9), 1975–1978, 1999.

[68] J. M. Raimond, M. Brune, and S. Haroche. Manipulating quantum entanglement with atoms and photons in a cavity. *Rev. Mod. Phys.*, **73**(3):565–582, 2001.

[69] D. Jaksch, J. I. Cirac, P. Zoller, S. L. Rolston, R. Côté, and M. D. Lukin. Fast quantum gates for neutral atoms. *Phys. Rev. Lett.*, **85**(10), 2208–2211, 2000.

[70] S. Bize, Y. Sortais, M. S. Santos, C. Mandache, A. Clairon, and C. Salomon. High-accuracy measurement of the ground-state ^{87}Rb hyperfine splitting in an atomic fountain. *Europhys. Lett.*, **45**(5), 558–564, 1999.

[71] Worawarong Rakreungdet, Jae Hoon Lee, Kim Fook Lee, Brian E. Mischuck, Enrique Montano, and Poul S. Jessen. Accurate microwave control and real-time diagnostics of neutral-atom qubits. *Phys. Rev. A*, **79**(2), 022316, 2009.

[72] Line H. Pedersen. *Neutral Atom Quantum Computing with Rydberg Blockade.* PhD thesis, University of Aarhus, 2006.

[73] M. D. Lukin, M. Fleischhauer, R. Cote, L. M. Duan, D. Jaksch, J. I. Cirac, and P. Zoller. Dipole blockade and quantum information processing in mesoscopic atomic ensembles. *Phys. Rev. Lett.*, **87**(3), 037901, 2001.

[74] M. Saffman, T. G. Walker, and K. Molmer. Quantum information with Rydberg atoms. *http://www.citebase.org/abstract?id=oai:arXiv.org:0909.4777*, 2009.

[75] T.F. Gallagher. *Rydberg Atoms.* Cambridge University Press, Cambridge, first edition, 1994.

[76] G. W. F. Drake and R. A. Swainson. Quantum defects and the 1/n dependence of Rydberg energies: Second-order polarization effects. *Phys. Rev. A*, **44**(9):5448–5459, 1991.

[77] F. Gounand. Calculation of radial matrix elements and radiative lifetimes for highly excited states of alkali atoms using the coulomb approximation. *J. Phys. Fr.*, **40**(5), 457–460, 1979.

[78] Gallagher T.F. and Pillet P. Dipole-dipole interactions of Rydberg atoms. *Adv. At. Mol. Opt. Phys.*, **56**:161, 2008.

[79] Z. Hu and H. J. Kimble. Observation of a single atom in a magneto-optical trap. *Opt. Lett.*, **19**(22), 1888–1890, 1994.

[80] D. Frese, B. Ueberholz, S. Kuhr, W. Alt, D. Schrader, V. Gomer, and D. Meschede. Single atoms in an optical dipole trap: Towards a deterministic source of cold atoms. *Phys. Rev. Lett.*, **85**(18), 3777–3780, 2000.

[81] M. Saffman and T. G. Walker. Analysis of a quantum logic device based on dipole-dipole interactions of optically trapped Rydberg atoms. *Phys. Rev. A*, **72**(2), 022347, 2005.

[82] A. Grabowski and T. Pfau. A lattice of magneto-optical and magnetic traps for cold atoms. *Eur. Phys. J. D*, **22**(3), 347–354, 2003.

[83] R.F. Stebbings and F.B.Dunning. *Rydberg States of Atoms and Molecules*. Cambridge University Press, Cambridge, 1983.

[84] P. Thoumany, T. Hänsch, G. Stania, L. Urbonas, and Th. Becker. Optical spectroscopy of rubidium rydberg atoms with a 297 nm frequency-doubled dye laser. *Opt. Lett.*, **34**(11), 1621–1623, 2009.

[85] B. K. Teo, D. Feldbaum, T. Cubel, J. R. Guest, P. R. Berman, and G. Raithel. Autler-townes spectroscopy of the $5s1/2 - 5p3/2 - 44d$ cascade of cold ^{85}Rb atoms. *Phys. Rev. A*, **68**(5), 053407, 2003.

[86] T. A. Johnson, E. Urban, T. Henage, L. Isenhower, D. D. Yavuz, T. G. Walker, and M. Saffman. Rabi oscillations between ground and Rydberg

states with dipole-dipole atomic interactions. *Phys. Rev. Lett.*, **100**(11), 113003, 2008.

[87] T. Cubel, B. K. Teo, V. S. Malinovsky, J. R. Guest, A. Reinhard, B. Knuffman, P. R. Berman, and G. Raithel. Coherent population transfer of ground-state atoms into Rydberg states. *Phys. Rev. A*, **72**(2), 023405, 2005.

[88] E. Urban, T. A. Johnson, T. Henage, L. Isenhower, D. D. Yavuz, T. G. Walker, and M. Saffman. Observation of collective excitation of two individual atoms in the Rydberg blockade regime. *Nat. Phys.*,**5**(2), 110–114, 2009.

[89] A. Gaetan, Y. Miroshnychenko, T. Wilk, A. Chotia, M. Viteau, D. Comparat, P. Pillet, A. Browaeys, and P. Grangier. Observation of collective excitation of two individual atoms in the Rydberg blockade regime. *Nat Phys*, **5**(2), 115–118, 2009.

[90] L. Isenhower, E. Urban, X. L. Zhang, A. T. Gill, T. Henage, T. A. Johnson, T. G. Walker, and M. Saffman. Demonstration of a neutral atom controlled-not quantum gate, 2009.

[91] J. Benhelm, G. Kirchmair, C. F. Roos, and R. Blatt. Towards fault-tolerant quantum computing with trapped ions. *Nat. Phys.*, **4**(6), 463–466, 2008.

[92] W. R. Anderson, J. R. Veale, and T. F. Gallagher. Resonant dipole-dipole energy transfer in a nearly frozen Rydberg gas. *Phys. Rev. Lett.*, **80**(2), 249–252, 1998.

[93] I. Mourachko, D. Comparat, F. de Tomasi, A. Fioretti, P. Nosbaum, V. M. Akulin, and P. Pillet. Many-body effects in a frozen Rydberg gas. *Phys. Rev. Lett.*, **80**(2), 253–256, 1998.

[94] D. Tong, S. M. Farooqi, J. Stanojevic, S. Krishnan, Y. P. Zhang, R. Côté, E. E. Eyler, and P. L. Gould. Local blockade of Rydberg excitation in an ultracold gas. *Phys. Rev. Lett.*, **93**(6), 063001, 2004.

[95] Rolf Heidemann, Ulrich Raitzsch, Vera Bendkowsky, Björn Butscher, Robert Löw, and Tilman Pfau. Rydberg excitation of bose-einstein condensates. *Phys. Rev. Lett.*, **100**(3), 033601, 2008.

[96] Robert Low, Hendrik Weimer, Ulrich Raitzsch, Rolf Heidemann, Vera Bendkowsky, Bjorn Butscher, Hans Peter Buchler, and Tilman Pfau. Universal scaling in a strongly interacting Rydberg gas, 2009.

[97] Thibault Vogt, Matthieu Viteau, Amodsen Chotia, Jianming Zhao, Daniel Comparat, and Pierre Pillet. Electric-field induced dipole blockade with Rydberg atoms. *Phys. Rev. Lett.*, **99**(7), 073002, 2007.

[98] J. Reichel, W. Hänsel, and T. W. Hänsch. Atomic micromanipulation with magnetic surface traps. *Phys. Rev. Lett.*, **83**(17), 3398–3401, 1999.

[99] D. Tong, S. M. Farooqi, E. G. M. van Kempen, Z. Pavlovic, J. Stanojevic, R. Côté, E. E. Eyler, and P. L. Gould. Observation of electric quadrupole transitions to Rydberg *nd* states of ultracold rubidium atoms. *Phys. Rev. A*, **79**(5), 052509, 2009.

[100] Carl E. Wieman and Leo Hollberg. Using diode lasers for atomic physics. *Rev. Sci. Instrum.*, **62**(1), 1–20, 1991.

[101] A. K. Mohapatra, T. R. Jackson, and C. S. Adams. Coherent optical detection of highly excited Rydberg states using electromagnetically induced transparency. *Phys. Rev. Lett.*, **98**(11), 113003, 2007.

[102] R. W. P. Drever, J. L. Hall, F. V. Kowalski, J. Hough, G. M. Ford, A. J. Munley, and H. Ward. Laser phase and frequency stabilization using an optical resonator. *Appl. Phys. B*, **31**(2), 97–105, 1983.

[103] G.F. Franklin, J.D. Powell, and A Emami-Naeni. *Feedback Control of Dynamic Systems*. Addison-Wesley, Reading, MA, 1987.

[104] T. Okoshi, K. Kikuchi, and A. Nakayama. Novel method for high resolution measurement of laser output spectrum. *Electr. Lett.*, **16**(16), 630–631, 1980.

[105] Hanne Ludvigsen, Mika Tossavainen, and Matti Kaivola. Laser linewidth measurements using self-homodyne detection with short delay. *Opt. Commun.*, **155**, 180 – 186, 1998.

[106] M. Brieger, H. Busener, A. Hese, F. v.Moers, and A. Renn. Enhancement of single frequency sgh in a passive ring resonator. *Opt. Commun.*, **38**(5-6), 423 – 426, 1981.

[107] S. H. Autler and C. H. Townes. Stark effect in rapidly varying fields. *Phys. Rev.*, **100**(2), 703–722, 1955.

[108] D. Suter. *The Physics of Laser-Atom Interactions*. Cambridge University Press, Cambridge, second edition, 1997.

[109] L. Allen and J.H. Eberly. *Optical Resonance and Two-level Atoms*. Dover Publications, Inc, New York, second edition, 1987.

[110] J. P. Gordon and A. Ashkin. Motion of atoms in a radiation trap. *Phys. Rev. A*, **21**(5), 1606–1617, 1980.

[111] Paul D. Lett, Richard N. Watts, Christoph I. Westbrook, William D. Phillips, Phillip L. Gould, and Harold J. Metcalf. Observation of atoms laser cooled below the doppler limit. *Phys. Rev. Lett.*, **61**(2), 169–172, 1988.

[112] J. Dalibard and C. Cohen-Tannoudji. Laser cooling below the doppler limit by polarization gradients: simple theoretical models. *J. Opt. Soc. Am. B*, **6**(11), 2023–2045, 1989.

[113] A. Ashkin and J. P. Gordon. Stability of radiation-pressure particle traps: an optical earnshaw theorem. *Opt. Lett.*, **8**(10), 511–513, 1983.

[114] E. L. Raab, M. Prentiss, Alex Cable, Steven Chu, and D. E. Pritchard. Trapping of neutral sodium atoms with radiation pressure. *Phys. Rev. Lett.*, **59**(23), 2631–2634, 1987.

[115] A. Ashkin. Trapping of Atoms by Resonance Radiation Pressure. *Phys. Rev. Lett.*, **40**(12), 729–732, 1978.

[116] T. H. Havelock. Mathematical Analysis of Wave Propagation in Isotropic of $p-$Dimensions. *Proc. London Math. Soc.*, $\mathbf{s2-2}(1)$, 122–137, 1905.

[117] J. Durnin. Exact solutions for nondiffracting beams. I. The scalar theory. *J. Opt. Soc. Am. A*, **4**(4), 651–654, 1987.

[118] Antti Vasara, Jari Turunen, and Ari T. Friberg. Realization of general nondiffracting beams with computer-generated holograms. *J. Opt. Soc. Am. A*, **6**(11), 1748–1754, 1989.

[119] M. Born and E. Wolf. *Principles of Optics*. Cambridge University Press, Cambridge, seven edition, 1999.

[120] C. Monroe, W. Swann, H. Robinson, and C. Wieman. Very cold trapped atoms in a vapor cell. *Phys. Rev. Lett.*, **65**(13), 1571–1574, 1990.

[121] Daniel A. Steck. Rubidium-87 and rubidium-85 D-line data, http://steck.us/alkalidata, revision 2.0.1, 2 May 2008.

[122] H.A. Bethe and E.A. Salpeter. *Quantum Mechanics of One and Two Electron Atoms*. Academic Press, New York, first edition, 1957.

[123] S. A. Bhatti, C. L. Cromer, and W. E. Cooke. Analysis of the Rydberg character of the $5d7dd21$ state of barium. *Phys. Rev. A*, **24**(1), 161–165, 1981.